

## The Vera C. Rubin Observatory Data Preview 1

1  
2 VERA C. RUBIN OBSERVATORY TEAM,<sup>1</sup> TATIANA ACERO-CUELLAR ,<sup>2</sup> EMILY ACOSTA ,<sup>1</sup> CHRISTINA L. ADAIR ,<sup>3</sup>  
3 PRAKRUTH ADARI ,<sup>4</sup> JENNIFER K. ADELMAN-McCARTHY ,<sup>5</sup> ANASTASIA ALEXOV ,<sup>1</sup> RUSS ALLBERY ,<sup>1</sup>  
4 ROBYN ALLSMAN,<sup>1</sup> YUSRA ALSAYYAD ,<sup>6</sup> JHONATAN AMADO ,<sup>5</sup> NATHAN AMOUROUX ,<sup>7</sup> PIERRE ANTILOGUS ,<sup>8</sup>  
5 ALEXIS ARACENA ALCAYAGA,<sup>9</sup> GONZALO ARAVENA-ROJAS ,<sup>9</sup> CLAUDIO H. ARAYA CORTES,<sup>9</sup> ÉRIC AUBOURG ,<sup>10</sup>  
6 TIM S. AXELROD ,<sup>11</sup> JOHN BANOVETZ ,<sup>12</sup> CARLOS BARRÍA,<sup>9</sup> AMANDA E. BAUER ,<sup>13</sup> BRIAN J. BAUMAN,<sup>14</sup>  
7 ELLEN BECHTOL ,<sup>15</sup> KEITH BECHTOL ,<sup>1,16</sup> ANDREW C. BECKER ,<sup>17</sup> VALERIE R. BECKER ,<sup>18</sup>  
8 MARK G. BECKETT ,<sup>19</sup> ERIC C. BELLM ,<sup>20</sup> PEDRO H. BERNARDINELLI ,<sup>21</sup> FEDERICA BETTINA BIANCO ,<sup>2,22,23</sup>  
9 ROBERT D. BLUM ,<sup>18</sup> JOANNE BOGART,<sup>24</sup> ADAM BOLTON ,<sup>3</sup> MICHAEL T. BOOTH,<sup>1</sup> JAMES F. BOSCH ,<sup>6</sup>  
10 ALEXANDRE BOUCAUD ,<sup>25</sup> DOMINIQUE BOUTIGNY ,<sup>7</sup> ROBERT A. BOVILL,<sup>1</sup> ANDREW BRADSHAW,<sup>3,24</sup>  
11 JOHAN BREGEON ,<sup>26</sup> MASSIMO BRESCIA ,<sup>27</sup> BRIAN J. BRONDEL ,<sup>28</sup> ALEXANDER BROUGHTON ,<sup>24</sup>  
12 AUDREY BUDLONG ,<sup>29</sup> DIMITRI BUFFAT,<sup>26</sup> RODOLFO CANESTRARI ,<sup>30</sup> NEVEN CAPLAR ,<sup>20</sup> JEFFREY L. CARLIN ,<sup>1</sup>  
13 ROSS CEBALLO ,<sup>18</sup> COLIN ORION CHANDLER ,<sup>31,20,32</sup> CHIHWAY CHANG ,<sup>33</sup> GLENAVER CHARLES-EMERSON,<sup>1</sup>  
14 HSN-FANG CHIANG ,<sup>3</sup> JAMES CHIANG ,<sup>24</sup> YUMI CHOI ,<sup>34</sup> ERIC J. CHRISTENSEN ,<sup>9</sup> CHARLES F. CLAVER,<sup>1</sup>  
15 ANDY W. CLEMENTS,<sup>1</sup> JOSEPH J. COCKRUM,<sup>1</sup> JOHANN COHEN-TANUGI ,<sup>35</sup> FRANCO COLLEONI,<sup>9</sup> CÉLINE COMBET ,<sup>26</sup>  
16 ANDREW J. CONNOLLY ,<sup>21</sup> JULIO EDUARDO CONSTANZO CORDOVA ,<sup>9</sup> HANS E CONTRERAS,<sup>9</sup>  
17 JOHN FRANKLIN CRENSHAW ,<sup>21</sup> SYLVIE DAGORET-CAMPAGNE ,<sup>36</sup> SCOTT F. DANIEL,<sup>20</sup> FELIPE DARUICH,<sup>9</sup>  
18 GUILLAUME DAUBARD ,<sup>8</sup> GREG DAUES,<sup>37</sup> ERIK DENNIHY ,<sup>1</sup> STEPHANIE J. H. DEPPE ,<sup>18</sup> SETH W. DIGEL ,<sup>3</sup>  
19 PETER E. DOHERTY,<sup>38</sup> CYRILLE DOUX ,<sup>26</sup> ALEX DRLICA-WAGNER ,<sup>5</sup> GREGORY P. DUBOIS-FELSMANN ,<sup>39</sup>  
20 FROSSIE ECONOMOU ,<sup>1</sup> ORION EIGER ,<sup>3,24</sup> LUKAS EISERT ,<sup>3</sup> ALAN M. EISNER ,<sup>40</sup> ANTHONY ENGLERT ,<sup>41</sup>  
21 BADEN ERB,<sup>9</sup> JUAN A. FABREGA,<sup>9</sup> PARKER FAGRELIUS,<sup>1</sup> KEVIN FANNING ,<sup>3</sup> ANGELO FAUSTI NETO ,<sup>1</sup>  
22 PETER S. FERGUSON ,<sup>21,16</sup> AGNÈS FERTÉ ,<sup>3</sup> KRZYSZTOF FINDEISEN ,<sup>20</sup> MERLIN FISHER-LEVINE ,<sup>42</sup>  
23 GLORIA FONSECA ALVAREZ ,<sup>34</sup> MICHAEL D. FOSS,<sup>3</sup> DOMINIQUE FOCHEZ ,<sup>43</sup> DAN C. FUCHS ,<sup>3</sup> SHENMING FU ,<sup>24</sup>  
24 EMMANUEL GANGLER ,<sup>44</sup> IGOR GAPONENKO,<sup>3</sup> JULEN GARCIA ,<sup>45</sup> JOHN H GATES,<sup>3</sup> RANPAL K. GILL ,<sup>28</sup>  
25 ENRICO GIRO ,<sup>46</sup> THOMAS GLANZMAN ,<sup>3</sup> ROBINSON GODOY,<sup>9</sup> IAIN GOODENOW,<sup>1</sup> MIRANDA R. GORSUCH ,<sup>16</sup>  
26 MICHELLE GOWER ,<sup>37</sup> MELISSA L. GRAHAM ,<sup>20,21</sup> MIKAEL GRANVIK ,<sup>47,48</sup> SARAH GREENSTREET ,<sup>34</sup> WEN GUAN ,<sup>12</sup>  
27 THIBAUT GUILLEMIN ,<sup>7</sup> LEANNE P. GUY ,<sup>9</sup> DIANE HASCALL,<sup>3</sup> PATRICK A. HASCALL,<sup>3</sup> AREN NATHANIEL HEINZE ,<sup>21</sup>  
28 FABIO HERNANDEZ ,<sup>49</sup> KENNETH HERNER ,<sup>5</sup> ARDIS HERROLD,<sup>1</sup> CLARE R. HIGGS ,<sup>18</sup> JOSHUA HOBLITT ,<sup>1</sup>  
29 ERIN LEIGH HOWARD ,<sup>20</sup> MINHEE HYUN ,<sup>9</sup> AMANDA IBSEN,<sup>28</sup> PATRICK INGRAHAM ,<sup>11</sup> DAVID H. IRVING ,<sup>18</sup>  
30 ŽELJKO IVEZIĆ ,<sup>1,20</sup> SUZANNE H. JACOBY,<sup>1</sup> BUELL T. JANNUZI ,<sup>50</sup> SREEVANI JARUGULA ,<sup>5</sup> M. JAMES JEE ,<sup>51,52</sup>  
31 TIM JENNESS ,<sup>1</sup> TOBY C. JENNINGS ,<sup>3</sup> ANDREA JEREMIE ,<sup>7</sup> GARRETT JERNIGAN,<sup>53,\*</sup> DAVID JIMÉNEZ MEJÍAS,<sup>9</sup>  
32 ANTHONY S. JOHNSON ,<sup>3</sup> R. LYNNE JONES ,<sup>20</sup> ROGER WILLIAM LEWIS JONES ,<sup>54</sup> CLAIRE JURAMY-GILLES ,<sup>8</sup>  
33 MARIO JURIĆ ,<sup>21</sup> STEVEN M. KAHN ,<sup>55</sup> J. BRYCE KALMBACH ,<sup>3</sup> YIJUNG KANG ,<sup>24,9</sup> ARUN KANAWADI ,<sup>56,6</sup>  
34 JEFFREY P. KANTOR,<sup>1</sup> EDWARD KARAVAKIS ,<sup>12</sup> KSHITIJ KELKAR ,<sup>9</sup> LEE S. KELVIN ,<sup>6</sup> SCOT J. KLEINMAN,<sup>57</sup>  
35 IVAN V. KOTOV,<sup>12</sup> GÁBOR KOVÁCS ,<sup>21</sup> MIKOLAJ KOWALIK ,<sup>37</sup> VICTOR L. KRABBENDAM,<sup>1</sup> K. SIMON KRUGHOFF ,<sup>1,\*</sup>  
36 PETR KUBÁNEK ,<sup>9</sup> JACOB A. KURLANDER ,<sup>21</sup> MILE KUSULJA,<sup>26</sup> CRAIG S. LAGE ,<sup>52</sup> PAULO J. A. LAGO ,<sup>28</sup>  
37 KATHERINE LALIOTIS ,<sup>58</sup> TRAVIS LANGE ,<sup>3</sup> DIDIER LAPORTE,<sup>8</sup> RYAN M. LAU ,<sup>34</sup> JUAN CARLOS LAZARTE,<sup>3</sup>  
38 QUENTIN LE BOULC'H ,<sup>49</sup> PIERRE-FRANÇOIS LÉGET ,<sup>6</sup> LAURENT LE GUILLOU ,<sup>8</sup> BENJAMIN LEVINE ,<sup>4</sup> MING LIANG,<sup>1</sup>  
39 SHUANG LIANG,<sup>3</sup> KIAN-TAT LIM ,<sup>3</sup> ANJA VON DER LINDEN ,<sup>4</sup> HUAN LIN ,<sup>5</sup> MARGAUX LOPEZ ,<sup>3</sup>  
40 JUAN J. LOPEZ TORO,<sup>9</sup> PETER LOVE,<sup>54</sup> ROBERT H. LUPTON ,<sup>6</sup> NATE B. LUST ,<sup>6</sup> LAUREN A. MACARTHUR ,<sup>6</sup>  
41 SEAN PATRICK MACBRIDE ,<sup>59</sup> GREG M. MADEJSKI,<sup>24</sup> GABRIELE MAINETTI ,<sup>49</sup> STEVEN J. MARGHEIM ,<sup>28</sup>  
42 THOMAS W. MARKIEWICZ ,<sup>3</sup> PHIL MARSHALL ,<sup>3</sup> STUART MARSHALL,<sup>24</sup> GUIDO MAULEN,<sup>9</sup> SIDNEY MAU ,<sup>56</sup>  
43 MORGAN MAY,<sup>60,12</sup> JEREMY McCORMICK ,<sup>3</sup> DAVID MCKAY ,<sup>61</sup> ROBERT MCKERCHER,<sup>1</sup> GUILLEM MEGIAS HOMAR ,<sup>62</sup>  
44 AARON M. MEISNER ,<sup>34</sup> FELIPE MENANTEAU,<sup>37</sup> HEATHER R. MENTZER ,<sup>40</sup> KRISTEN METZGER,<sup>18</sup>  
45 JOSHUA E. MEYERS ,<sup>24</sup> MICHELLE MILLER,<sup>34</sup> DAVID J. MILLS,<sup>1</sup> JOACHIM MOEYENS ,<sup>21</sup> MARC MONIEZ,<sup>36</sup>  
46 FRED E. MOOLEKAMP ,<sup>63</sup> C. A. L. MORALES MARÍN ,<sup>9</sup> FRITZ MUELLER ,<sup>3</sup> JAMES R. MULLANEY ,<sup>64</sup>  
47 FREDDY MUÑOZ ARANCIBIA,<sup>1</sup> KATE NAPIER ,<sup>24</sup> HOMER NEAL,<sup>3</sup> ERIC H. NEILSEN, JR. ,<sup>5</sup> JEREMY NEVEU ,<sup>36</sup>  
48 TIMOTHY NOBLE,<sup>65</sup> ERFAN NOURBAKHSH ,<sup>6</sup> KNUT OLSEN ,<sup>34</sup> WILLIAM O'MULLANE ,<sup>9</sup> DMITRY ONOPRIENKO,<sup>3</sup>  
49 MARCO ORIUNNO ,<sup>3</sup> SHAWN OSIER,<sup>3</sup> RUSSELL E. OWEN,<sup>20</sup> AASHAY PAI ,<sup>33</sup> JOHN K. PAREJKO ,<sup>20</sup> HYE YUN PARK ,<sup>56</sup>

50 JAMES B. PARSONS,<sup>37,\*</sup> MARIA T. PATTERSON<sup>id</sup>,<sup>20</sup> MARINA S. PAVLOVIC<sup>id</sup>,<sup>9</sup> KARLA PEÑA RAMÍREZ<sup>id</sup>,<sup>9</sup>  
 51 JOHN R. PETERSON<sup>id</sup>,<sup>66</sup> STEPHEN R. PIETROWICZ<sup>id</sup>,<sup>37</sup> ANDRÉS A. PLAZAS MALAGÓN<sup>id</sup>,<sup>3,24</sup> REBEKAH POLEN,<sup>56</sup>  
 52 HANNAH MARY MARGARET POLLEK,<sup>3</sup> PAUL A. PRICE<sup>id</sup>,<sup>6</sup> BRUNO C. QUINT<sup>id</sup>,<sup>1</sup> JOSÉ MIGUEL QUINTERO MARIN,<sup>9</sup>  
 53 MARKUS RABUS<sup>id</sup>,<sup>67</sup> BENJAMIN RACINE<sup>id</sup>,<sup>43</sup> VELJKO RADEKA,<sup>12</sup> MANON RAMEL,<sup>26</sup> ARIANNA RANABHAT<sup>id</sup>,<sup>68</sup>  
 54 ANDREW P. RASMUSSEN<sup>id</sup>,<sup>24</sup> DAVID A. RATHFELDER,<sup>69</sup> MEREDITH L. RAWLS<sup>id</sup>,<sup>20,21</sup> SOPHIE L. REED<sup>id</sup>,<sup>6</sup>  
 55 KEVIN A. REIL<sup>id</sup>,<sup>3</sup> DAVID J. REISS,<sup>20</sup> MICHAEL A. REUTER<sup>id</sup>,<sup>1</sup> TIAGO RIBEIRO<sup>id</sup>,<sup>1</sup> MICKAEL RIGAULT<sup>id</sup>,<sup>70</sup>  
 56 VINCENT J. RIOT<sup>id</sup>,<sup>14</sup> STEVEN M. RITZ<sup>id</sup>,<sup>40</sup> MARIO F. RIVERA RIVERA,<sup>9</sup> BRANT E. ROBERTSON<sup>id</sup>,<sup>71</sup>  
 57 WILLIAM ROBY<sup>id</sup>,<sup>39</sup> GABRIELE RODEGHIERO<sup>id</sup>,<sup>72</sup> AARON ROODMAN<sup>id</sup>,<sup>24</sup> LUCA ROSIGNOLI<sup>id</sup>,<sup>73,72</sup> CÉCILE ROUCELLE<sup>id</sup>,<sup>25</sup>  
 58 MATTHEW R. RUMORE<sup>id</sup>,<sup>12</sup> STEFANO RUSSO,<sup>8</sup> ELI S. RYKOFF<sup>id</sup>,<sup>24</sup> ANDREI SALNIKOV<sup>id</sup>,<sup>3</sup> BRUNO O. SÁNCHEZ<sup>id</sup>,<sup>43</sup>  
 59 DAVID SANMARTIM<sup>id</sup>,<sup>9</sup> CLARE SAUNDERS<sup>id</sup>,<sup>6</sup> RAFE H. SCHINDLER,<sup>24</sup> SAMUEL J. SCHMIDT<sup>id</sup>,<sup>52</sup> JACQUES SEBAG,<sup>9</sup>  
 60 NIMA SEDAGHAT<sup>id</sup>,<sup>20</sup> BRIAN SELVY,<sup>1</sup> EDGARD ESTEBAN SEPULVEDA VALENZUELA,<sup>9</sup> GONZALO SERICHE<sup>id</sup>,<sup>9</sup>  
 61 JACQUELINE C. SERON-NAVARRETE<sup>id</sup>,<sup>9</sup> IGNACIO SEVILLA-NOARBE<sup>id</sup>,<sup>74</sup> ALYSHA B. SHUGART<sup>id</sup>,<sup>9</sup> JONATHAN SICK<sup>id</sup>,<sup>75,1</sup>  
 62 CRISTIÁN SILVA<sup>id</sup>,<sup>9</sup> MATHEW C. SIMS<sup>id</sup>,<sup>76</sup> JALADH SINGHAL<sup>id</sup>,<sup>39</sup> KEVIN BENJAMIN SIRUNO,<sup>9</sup> COLIN T. SLATER<sup>id</sup>,<sup>20</sup>  
 63 BRIANNA M. SMART<sup>id</sup>,<sup>20</sup> ADAM SNYDER<sup>id</sup>,<sup>52</sup> CHRISTINE SOLDAHL,<sup>3</sup> IOANA SOTUELA ELORRIAGA<sup>id</sup>,<sup>9</sup> BRIAN STALDER<sup>id</sup>,<sup>1</sup>  
 64 HERNAN STOCKEBRAND<sup>id</sup>,<sup>9</sup> ALAN L. STRAUSS<sup>id</sup>,<sup>18</sup> MICHAEL A. STRAUSS<sup>id</sup>,<sup>6</sup> KRZYSZTOF SUBERLAK<sup>id</sup>,<sup>20</sup>  
 65 IAN S. SULLIVAN<sup>id</sup>,<sup>20</sup> JOHN D. SWINBANK<sup>id</sup>,<sup>77,6</sup> DIEGO TAPIA<sup>id</sup>,<sup>9</sup> ALESSIO TARANTO<sup>id</sup>,<sup>72,73</sup> DAN S. TARANU<sup>id</sup>,<sup>6</sup>  
 66 JOHN GREGG THAYER<sup>id</sup>,<sup>3</sup> SANDRINE THOMAS<sup>id</sup>,<sup>18</sup> ADAM J. THORNTON<sup>id</sup>,<sup>1</sup> ROBERTO TIGHE,<sup>9</sup>  
 67 LAURA TORIBIO SAN CIPRIANO,<sup>74</sup> TE-WEI TSAI<sup>id</sup>,<sup>1</sup> DOUGLAS L. TUCKER<sup>id</sup>,<sup>5</sup> MAX TURRI,<sup>3</sup> J. ANTHONY TYSON<sup>id</sup>,<sup>52</sup>  
 68 ELANA K. URBACH<sup>id</sup>,<sup>78</sup> YOUSUKE UTSUMI<sup>id</sup>,<sup>79</sup> BRIAN VAN KLAVEREN,<sup>3</sup> WOUTER VAN REEVEN<sup>id</sup>,<sup>9</sup>  
 69 PETER ANTHONY VAUCHER<sup>id</sup>,<sup>3</sup> PAULINA VENEGAS<sup>id</sup>,<sup>28</sup> APRAJITA VERMA<sup>id</sup>,<sup>80</sup> ANTONIA SIERRA VILLARREAL<sup>id</sup>,<sup>3</sup>  
 70 STELIOS VOUTSINAS<sup>id</sup>,<sup>1</sup> CHRISTOPHER W. WALTER<sup>id</sup>,<sup>56</sup> YUANKUN (DAVID) WANG<sup>id</sup>,<sup>21</sup> CHRISTOPHER Z. WATERS<sup>id</sup>,<sup>6</sup>  
 71 CHRISTINA C. WILLIAMS<sup>id</sup>,<sup>34</sup> BETH WILLMAN<sup>id</sup>,<sup>81</sup> MATTHIAS WITTGEN<sup>id</sup>,<sup>3</sup> W. M. WOOD-VASEY<sup>id</sup>,<sup>82</sup> WEI YANG<sup>id</sup>,<sup>3</sup>  
 72 ZHAOYU YANG<sup>id</sup>,<sup>12</sup> BRIAN P. YANNY<sup>id</sup>,<sup>5</sup> PETER YOACHIM<sup>id</sup>,<sup>20</sup> TIANQING ZHANG<sup>id</sup>,<sup>82</sup> CONGHAO ZHOU<sup>id</sup>,<sup>40</sup> AND  
 73 DANICA ŽILKOVÁ<sup>id</sup>,<sup>28</sup>

74 <sup>1</sup>Vera C. Rubin Observatory Project Office, 950 N. Cherry Ave., Tucson, AZ 85719, USA

75 <sup>2</sup>Department of Physics and Astronomy, University of Delaware, Newark, DE 19716-2570, USA

76 <sup>3</sup>SLAC National Accelerator Laboratory, 2575 Sand Hill Rd., Menlo Park, CA 94025, USA

77 <sup>4</sup>Department of Physics and Astronomy, Stony Brook University, Stony Brook, NY 11794, USA

78 <sup>5</sup>Fermi National Accelerator Laboratory, P. O. Box 500, Batavia, IL 60510, USA

79 <sup>6</sup>Department of Astrophysical Sciences, Princeton University, Princeton, NJ 08544, USA

80 <sup>7</sup>Université Savoie Mont-Blanc, CNRS/IN2P3, LAPP, 9 Chemin de Bellevue, F-74940 Annecy-le-Vieux, France

81 <sup>8</sup>Sorbonne Université, Université Paris Cité, CNRS/IN2P3, LPNHE, 4 place Jussieu, F-75005 Paris, France

82 <sup>9</sup>Vera C. Rubin Observatory, Avenida Juan Cisternas #1500, La Serena, Chile

83 <sup>10</sup>Université Paris Cité, CNRS/IN2P3, CEA, APC, 4 rue Elsa Morante, F-75013 Paris, France

84 <sup>11</sup>Steward Observatory, The University of Arizona, 933 N. Cherry Ave., Tucson, AZ 85721, USA

85 <sup>12</sup>Brookhaven National Laboratory, Upton, NY 11973, USA

86 <sup>13</sup>Yerkes Observatory, 373 W. Geneva St., Williams Bay, WI 53191, USA

87 <sup>14</sup>Lawrence Livermore National Laboratory, 7000 East Avenue, Livermore, CA 94550, USA

88 <sup>15</sup>Wisconsin IceCube Particle Astrophysics Center, University of Wisconsin—Madison, Madison, WI 53706, USA

89 <sup>16</sup>Department of Physics, University of Wisconsin-Madison, Madison, WI 53706, USA

90 <sup>17</sup>Amazon Web Services, Seattle, WA 98121, USA

91 <sup>18</sup>Vera C. Rubin Observatory/NSF NOIRLab, 950 N. Cherry Ave., Tucson, AZ 85719, USA

92 <sup>19</sup>Institute for Astronomy, University of Edinburgh, Royal Observatory, Blackford Hill, Edinburgh EH9 3HJ, UK

93 <sup>20</sup>University of Washington, Dept. of Astronomy, Box 351580, Seattle, WA 98195, USA

94 <sup>21</sup>Institute for Data-intensive Research in Astrophysics and Cosmology, University of Washington, 3910 15th Avenue NE, Seattle, WA  
 95 98195, USA

96 <sup>22</sup>Data Science Institute, University of Delaware, Newark, DE 19717 USA

97 <sup>23</sup>Joseph R. Biden, Jr., School of Public Policy and Administration, University of Delaware, Newark, DE 19717 USA

98 <sup>24</sup>Kavli Institute for Particle Astrophysics and Cosmology, SLAC National Accelerator Laboratory, 2575 Sand Hill Rd., Menlo Park, CA  
 99 94025, USA

100 <sup>25</sup>Université Paris Cité, CNRS/IN2P3, APC, 4 rue Elsa Morante, F-75013 Paris, France

101 <sup>26</sup>Université Grenoble Alpes, CNRS/IN2P3, LPSC, 53 avenue des Martyrs, F-38026 Grenoble, France

102 <sup>27</sup>Department of Physics "E. Pancini", University Federico II of Napoli, Via Cintia, 80126 Napoli, Italy

103 <sup>28</sup>Vera C. Rubin Observatory/NSF NOIRLab, Avenida Juan Cisternas #1500, La Serena, Chile

104 <sup>29</sup>University of Washington, Dept. of Physics, Box 351580, Seattle, WA 98195, USA

105 <sup>30</sup>INAF Istituto di Astrofisica Spaziale e Fisica Cosmica di Palermo, Via Ugo la Malfa 153, 90146, Palermo, Italy

- 106 <sup>31</sup>LSST Interdisciplinary Network for Collaboration and Computing, Tucson, USA
- 107 <sup>32</sup>Department of Astronomy and Planetary Science, Northern Arizona University, P.O. Box 6010, Flagstaff, AZ 86011, USA
- 108 <sup>33</sup>Department of Astronomy and Astrophysics, University of Chicago, 5640 South Ellis Avenue, Chicago, IL 60637, USA
- 109 <sup>34</sup>NSF NOIRLab, 950 N. Cherry Ave., Tucson, AZ 85719, USA
- 110 <sup>35</sup>LPCA, Université Clermont-Auvergne, CNRS/IN2P3, Clermont-Ferrand, France
- 111 <sup>36</sup>Université Paris-Saclay, CNRS/IN2P3, IJCLab, 15 Rue Georges Clemenceau, F-91405 Orsay, France
- 112 <sup>37</sup>NCSA, University of Illinois at Urbana-Champaign, 1205 W. Clark St., Urbana, IL 61801, USA
- 113 <sup>38</sup>Smithsonian Astrophysical Observatory, 60 Garden St., Cambridge MA 02138, USA
- 114 <sup>39</sup>Caltech/IPAC, California Institute of Technology, MS 100-22, Pasadena, CA 91125-2200, USA
- 115 <sup>40</sup>Santa Cruz Institute for Particle Physics and Physics Department, University of California–Santa Cruz, 1156 High St., Santa Cruz,
- 116 CA 95064, USA
- 117 <sup>41</sup>Department of Physics, Brown University, 182 Hope Street, Providence, RI 02912, USA
- 118 <sup>42</sup>D4D CONSULTING LTD., Suite 1 Second Floor, Everdene House, Deansleigh Road, Bournemouth, UK BH7 7DU
- 119 <sup>43</sup>Aix Marseille Université, CNRS/IN2P3, CPPM, 163 avenue de Luminy, F-13288 Marseille, France
- 120 <sup>44</sup>Université Clermont Auvergne, CNRS/IN2P3, LPCA, 4 Avenue Blaise Pascal, F-63000 Clermont-Ferrand, France
- 121 <sup>45</sup>C. Iñaki Goenaga, 5, 20600, Guipúzcoa, Spain
- 122 <sup>46</sup>INAF Osservatorio Astronomico di Trieste, Via Giovan Battista Tiepolo 11, 34143, Trieste, Italy
- 123 <sup>47</sup>Department of Physics, P.O. Box 64, 00014 University of Helsinki, Finland
- 124 <sup>48</sup>Asteroid Engineering Laboratory, Luleå University of Technology, Box 848, SE-981 28 Kiruna, Sweden
- 125 <sup>49</sup>CNRS/IN2P3, CC-IN2P3, 21 avenue Pierre de Coubertin, F-69627 Villeurbanne, France
- 126 <sup>50</sup>University of Arizona, Department of Astronomy and Steward Observatory, 933 N. Cherry Ave, Tucson, AZ 85721, USA
- 127 <sup>51</sup>Department of Astronomy, Yonsei University, 50 Yonsei-ro, Seoul 03722, Republic of Korea
- 128 <sup>52</sup>Physics Department, University of California, One Shields Avenue, Davis, CA 95616, USA
- 129 <sup>53</sup>Space Sciences Lab, University of California, 7 Gauss Way, Berkeley, CA 94720-7450, USA
- 130 <sup>54</sup>Lancaster University, Lancaster, UK
- 131 <sup>55</sup>Physics Department, University of California, 366 Physics North, MC 7300 Berkeley, CA 94720, USA
- 132 <sup>56</sup>Department of Physics, Duke University, Durham, NC 27708, USA
- 133 <sup>57</sup>Astromanager LLC, 63 Hala St, Hilo, 96720 Hawaii, USA
- 134 <sup>58</sup>Center for Cosmology and Astro-Particle Physics, The Ohio State University, Columbus, OH 43210, USA
- 135 <sup>59</sup>Physik-Institut, University of Zurich, Winterthurerstrasse 190, 8057 Zurich, Switzerland
- 136 <sup>60</sup>Department of Physics Columbia University, New York, NY 10027, USA
- 137 <sup>61</sup>EPCC, University of Edinburgh, 47 Potterrow, Edinburgh, EH8 9BT, UK
- 138 <sup>62</sup>Division of Physics, Mathematics and Astronomy, California Institute of Technology, Pasadena, CA 91125, USA
- 139 <sup>63</sup>soZen Inc., 105 Clearview Dr, Penfield, NY 14526
- 140 <sup>64</sup>Astrophysics Research Cluster, School of Mathematical and Physical Sciences, University of Sheffield, Sheffield, S3 7RH, United
- 141 Kingdom
- 142 <sup>65</sup>Science and Technology Facilities Council, Rutherford Appleton Laboratory, Harwell, UK
- 143 <sup>66</sup>Department of Physics and Astronomy, Purdue University, 525 Northwestern Ave., West Lafayette, IN 47907, USA
- 144 <sup>67</sup>Departamento de Matemática y Física Aplicadas, Facultad de Ingeniería, Universidad Católica de la Santísima Concepción, Alonso de
- 145 Rivera 2850, Concepción, Chile
- 146 <sup>68</sup>Australian Astronomical Optics, Macquarie University, North Ryde, NSW, Australia
- 147 <sup>69</sup>AURA, 950 N. Cherry Ave., Tucson, AZ 85719, USA
- 148 <sup>70</sup>Université Claude Bernard Lyon 1, CNRS/IN2P3, IP2I, 4 Rue Enrico Fermi, F-69622 Villeurbanne, France
- 149 <sup>71</sup>Department of Astronomy and Astrophysics, University of California–Santa Cruz, 1156 High St., Santa Cruz, CA 95064, USA
- 150 <sup>72</sup>INAF Osservatorio di Astrofisica e Scienza dello Spazio Bologna, Via P. Gobetti 93/3, 40129, Bologna, Italy
- 151 <sup>73</sup>Department of Physics and Astronomy (DIFA), University of Bologna, Via P. Gobetti 93/2, 40129, Bologna, Italy
- 152 <sup>74</sup>Centro de Investigaciones Energéticas, Medioambientales y Tecnológicas, Av. Complutense 40, 28040 Madrid, Spain
- 153 <sup>75</sup>J.Sick Codes Inc., Penetanguishene, Ontario, Canada
- 154 <sup>76</sup>Science and Technology Facilities Council, UK Research and Innovation, Polaris House, North Star Avenue, Swindon, SN2 1SZ, UK
- 155 <sup>77</sup>ASTRON, Oude Hoogeveensedijk 4, 7991 PD, Dwingeloo, The Netherlands
- 156 <sup>78</sup>Department of Physics, Harvard University, 17 Oxford St., Cambridge MA 02138, USA
- 157 <sup>79</sup>National Astronomical Observatory of Japan, Chile Observatory, Los Abedules 3085, Vitacura, Santiago, Chile
- 158 <sup>80</sup>Department of Physics, University of Oxford, Denys Wilkinson Building, Keble Road, Oxford, OX1 3RH, UK
- 159 <sup>81</sup>LSST Discovery Alliance, 933 N. Cherry Ave., Tucson, AZ 85719, USA
- 160 <sup>82</sup>Department of Physics and Astronomy, University of Pittsburgh, 3941 O’Hara Street, Pittsburgh, PA 15260, USA

## ABSTRACT

We present Rubin Data Preview 1 (DP1), the first data from the NSF-DOE Vera C. Rubin Observatory, comprising raw and calibrated single-epoch images, coadds, difference images, detection catalogs, and ancillary data products. DP1 is based on 1792 optical/near-infrared exposures acquired over 48 distinct nights by the Rubin Commissioning Camera, LSSTComCam, on the Simonyi Survey Telescope at the Summit Facility on Cerro Pachón, Chile in late 2024. DP1 covers  $\sim 15 \text{ deg}^2$  distributed across seven roughly equal-sized non-contiguous fields, each independently observed in six broad photometric bands, *ugrizy*. The median FWHM of the point-spread function across all bands is approximately  $1''.14$ , with the sharpest images reaching about  $0''.58$ . The  $5\sigma$  point source depths for coadded images in the deepest field, the Extended Chandra Deep Field South, are:  $u = 24.55, g = 26.18, r = 25.96, i = 25.71, z = 25.07, y = 23.1$ . Other fields are no more than 2.2 magnitudes shallower in any band, where they have nonzero coverage. DP1 contains approximately 2.3 million distinct astrophysical objects, of which 1.6 million are extended in at least one band in coadds, and 431 solar system objects, of which 93 are new discoveries. DP1 is approximately 3.5 TB in size and is available to Rubin data rights holders via the Rubin Science Platform, a cloud-based environment for the analysis of petascale astronomical data. While small compared to future LSST releases, its high quality and diversity of data support a broad range of early science investigations ahead of full operations in 2026.

*Keywords:* Rubin Observatory – LSST

## 1. INTRODUCTION

The National Science Foundation (NSF)–Department of Energy (DOE) Vera C. Rubin Observatory is a ground-based, wide-field optical/near-infrared facility located on Cerro Pachón in northern Chile. Named in honor of Vera C. Rubin, a pioneering astronomer whose groundbreaking work in the 20th century provided the first convincing evidence for the existence of dark matter (V. C. Rubin & W. K. Ford 1970; V. C. Rubin et al. 1980), the observatory’s prime mission is to carry out the Legacy Survey of Space and Time (LSST) (Ž. Ivezić et al. 2019a). This 10-year survey is designed to obtain rapid-cadence, multi-band imaging of the entire visible southern sky approximately every 3–4 nights. Over its main  $18,000 \text{ deg}^2$  footprint, the LSST is expected to reach a depth of  $\sim 27$  magnitude in the r-band, with  $\sim 800$  visits per pointing in all filters (F. B. Bianco et al. 2022).

The Rubin Observatory system consists of four main components: the Simonyi Survey Telescope, featuring an 8.4 m diameter (6.5 m effective aperture) primary mirror that delivers a wide field of view; the 3.2-gigapixel LSST Science Camera (LSSTCam), capable of imaging 9.6 square degrees per exposure<sup>83</sup> with seeing-limited

quality in six broadband filters, *ugrizy* (320–1050 nm); an automated Data Management System that processes and archives tens of terabytes of data per night, generating science-ready data products within minutes for a global community of scientists; and an Education and Public Outreach (EPO) program that provides real-time data access, interactive tools, and educational content to engage the public. The integrated system’s étendue<sup>84</sup> of  $319 \text{ m}^2 \text{ deg}^2$ , is over an order of magnitude larger than that of any previous optical observatory, enabling a fast, large-scale survey with exceptional depth in a fraction of the time compared to other observatories.

The observatory’s design is driven by four key science themes: probing dark energy and dark matter; taking an inventory of the solar system; exploring the transient and variable optical sky; and mapping the Milky Way (Ž. Ivezić et al. 2019a). These themes inform the optimization of a range of system parameters, including image quality; photometric and astrometric accuracy; single-visit depth; coadded survey depth; the filter complement; the total number of visits per pointing and their distribution on the sky; and total sky coverage. Additionally, they inform the design of the data processing and access systems. By optimizing the system parameters to support a wide range of scientific goals, we maximize the observatory’s scientific output across

\* Author is deceased

<sup>83</sup> We define an “exposure” as the process of exposing all detectors in the focal plane. It is synonymous with the term “visit” in DP1. By contrast, an “image” is the output of a single detector following an exposure.

<sup>84</sup> The product of the primary mirror area and the angular area of its field of view for a given set of observing conditions.

all areas, making Rubin a powerful discovery machine capable of addressing a broad range of astrophysical questions.

Throughout the duration of the LSST, Rubin Observatory will issue a series of Data Releases, each representing a complete reprocessing of all LSST data collected up to that point. Prior to the start of the LSST survey, commissioning activities generated a significant volume of science-grade data. To make this early data available to the community, the Rubin Early Science Program (L. P. Guy et al. 2026) was established. One key component of this program is a series of Data Previews; early versions of the LSST Data Releases. These previews include preliminary data products derived from both simulated and commissioning data, which, together with early versions of the data access services, are intended to support high-impact early science, facilitate community readiness, and inform the development of Rubin’s operational capabilities ahead of the start of full survey operations. All data and services provided through the Rubin Early Science Program are offered on a shared-risk basis<sup>85</sup>.

This paper describes Rubin’s second of three planned Data Previews: Data Preview 1 (DP1) (NSF-DOE Vera C. Rubin Observatory 2025a). The first, Data Preview 0 (DP0), contained data products produced from the processing of simulated LSST-like data sets. These were released together with a very early version of the Rubin Science Platform (RSP) (M. Jurić et al. 2019), which provided the data access services. DP0 was released in multiple phases; DP0.1, DP0.2, and DP0.3, each building upon the previous and incorporating new data and functionalities. DP0.1 and DP0.2 uses data from the cosmoDC2 simulations (LSST Dark Energy Science Collaboration (LSST DESC) et al. 2021) prepared by the Dark Energy Science Collaboration (DESC), whereas DP0.3 is based on simulated datasets from the Solar System Science Collaboration (SSSC). Online documentation for DP0 is available at <https://dp0.lsst.io>.

DP1 contains data products derived from the reprocessing of science-grade exposures acquired by the Rubin Commissioning Camera (LSSTComCam) in late 2024. The third and final Data Preview, Data Preview 2 (DP2), is planned to be based on a reprocessing of all science-grade data taken with Rubin’s LSSTCam during commissioning.

All Rubin Data Releases and Previews are subject to a two-year proprietary period, with immediate access granted exclusively to LSST data rights holders<sup>86</sup> (R. Blum & the Rubin Operations Team 2020). After the two-year proprietary period, DP1 will be made public. However, even once the data become public, access for individuals without data rights will not be provided through Rubin Data Access Centers in the US and Chile (R. Blum & the Rubin Operations Team 2020). Alternative access mechanisms are still under discussion and have not yet been finalized.

In this paper, we describe the contents and validation of Rubin DP1, the first Data Preview to deliver data derived from observations conducted by the Vera C. Rubin Observatory, as well as the data-access mechanisms and community-support services that accompany it. DP1 is based on the reprocessing of 1792 science-grade exposures acquired during the first on-sky commissioning campaign, conducted over 48 nights between 2024-10-24 and 2024-12-11. It covers a total area of approximately  $\sim 15$  deg<sup>2</sup> distributed across seven distinct non-contiguous fields. The data products include raw and calibrated single-epoch images, coadded images, difference images, detection catalogs, and other derived data products. DP1 is about 3.5 TB in size and contains around 2.3 million distinct astronomical objects, detected in 2644 coadded images. Full DP1 release documentation is available at <https://dp1.lsst.io>. Despite Rubin Observatory still being in commissioning and not yet complete at the time the observations were acquired, Rubin DP1 provides an important first look at the data, showcasing its characteristics and capabilities.

The structure of this paper is as follows. In section 2 we describe the observatory system and overall construction and commissioning status at the time of data acquisition, the seven fields included in DP1, and the observing strategy used. Section 3 summarizes the contents of DP1 and the data products contained in the release. The data processing pipelines are described in section 4, followed by a description of the data validation and performance assessment in section 5. Section 6 describes the RSP, a cloud-based data science infrastructure that provides tools and services to Rubin data rights holders to access, visualize and analyze peta-scale data generated by the LSST. Section 7 presents Rubin Observatory’s model for community support, which emphasizes self-help via documentation and tutorials, and employs an open platform for issue reporting that en-

<sup>85</sup> Shared risk means early access with caveats: the community benefits from getting a head start on science, preparing analyses, and providing feedback, while also accepting that the system may not work as well as it will during full operations.

<sup>86</sup> Individuals or institutions with formal authorization to access proprietary data collected by the Vera C. Rubin Observatory. See <https://www.lsst.org/scientists/international-drh-list>

ables crowd-sourced solutions. Finally, a summary of the DP1 release and information on expected future releases of data is given in section 8. The appendix contains a useful glossary of terms used throughout this paper.

All magnitudes quoted are in the AB system (J. B. Oke & J. E. Gunn 1983), unless otherwise specified.

## 2. ON-SKY COMMISSIONING CAMPAIGN

The primary objective of the first Rubin on-sky commissioning campaign was to optically align the Simonyi Survey Telescope and verify its ability to deliver acceptable image quality using the Commissioning Camera, LSSTComCam. Additionally, the campaign provided valuable operational experience to support commissioning the LSST Science Camera, LSSTCam (T. Lange et al. 2024; A. Roodman et al. 2024). We note that commissioning LSSTComCam was not an objective of the campaign; rather LSSTComCam was used as a tool to support broader observatory commissioning, including early testing of the Active Optics System (AOS) (§2.1) and the LSST Science Pipelines (§2.4). As a result, many artifacts present in the data are specific to LSSTComCam and will be addressed only if they persist with LSSTCam. Accordingly, the image quality achieved during this campaign, and in the DP1 data, may not reflect the performance ultimately expected from LSSTCam.

Approximately 16,000 exposures<sup>87</sup> were collected during this campaign, the majority in support of AOS commissioning, system-level verification, and end-to-end testing of the telescope’s hardware and software. This included over 10000 exposures for AOS commissioning, more than 2000 bias and dark calibration frames, and over 2000 exposures dedicated to commissioning the LSST Science Pipelines. For DP1, we have selected a subset of 1792 science-grade exposures from this campaign that are most useful for the community to begin preparing for early science.

At the time of the campaign, the observatory was still under construction, with several key components, such as dome thermal control, full mirror control, and the final AOS configuration either incomplete or still undergoing commissioning. As a result, image quality varied widely throughout the campaign and exhibited a broader distribution than is expected with LSSTCam. Despite these limitations, the campaign success-

fully demonstrated system integration and established a functional observatory.

### 2.1. Simonyi Survey Telescope

The Simonyi Survey Telescope (B. Stalder et al. 2024) features a unique three-mirror design, including an 8.4-meter Primary Mirror Tertiary Mirror (M1M3) fabricated from a single substrate and a 3.5-meter Secondary Mirror (M2). This compact configuration supports a wide 3.5-degree field of view while enabling exceptional stability, allowing the telescope to slew and settle in under five seconds. To achieve the scientific goals of the 10-year LSST, the Observatory must maintain high image quality across its wide field of view (Ž. Ivezić et al. 2019b). This is accomplished through the AOS (B. Xin et al. 2015; G. Megias Homar et al. 2024a), which corrects, between successive exposures, wavefront distortions caused by optical misalignments and mirror surface deformations, primarily due to the effect of gravitational and thermal loads.

The AOS, which comprises an open-loop component and a closed-loop component, optimizes image quality by aligning the camera and M2 relative to M1M3, as well as adjusting the shapes of all three mirrors to nanometer precision. The AOS open-loop component corrects for predictable distortions and misalignments, while the closed-loop component addresses unpredictable or slowly varying aberrations using feedback from the corner wavefront sensors. The closed-loop wavefront sensing technique is curvature wavefront sensing, which infers wavefront errors in the optical system by analyzing extra- and intra-focal star images (S. Thomas et al. 2023). Since LSSTComCam lacks dedicated wavefront sensors, wavefront errors were instead estimated by defocusing the telescope  $\pm 1.5$  mm on either side of focus and applying the curvature wavefront sensing pipeline to the resulting images. Each night began with an initial alignment correction using a laser tracker to position the system within the capture range of the closed-loop algorithm (G. Megias Homar et al. 2024b). Once this coarse alignment was complete, the AOS refined the optical alignment and applied mirror surfaces corrections to optimize the image quality across the LSSTComCam field of view.

During LSST Science Pipelines commissioning (§2.4), observations were conducted using the AOS in open-loop mode only, without closed-loop corrections between exposures. Closed-loop operation, which requires additional intra- and extra-focal images with LSSTComCam, was not compatible with the continuous data acquisition needed by the pipelines. The image quality for these data was monitored by measuring the Point

<sup>87</sup> We define an exposure as the process of exposing all LSSTComCam detectors. It is synonymous with visit in DP1. By contrast, an image is the output of a single LSSTComCam detector following an exposure.

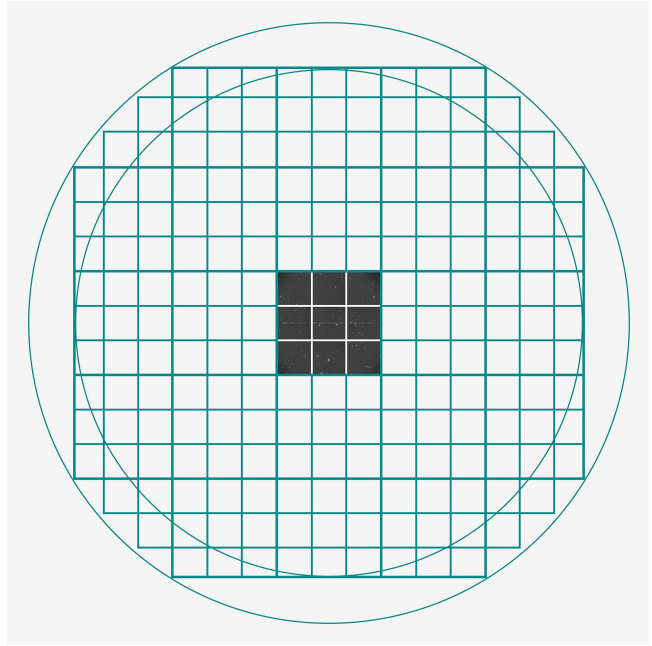
421 Spread Function (PSF) at Full Width at Half-Maximum  
 422 (FWHM), and closed-loop sequences were periodically  
 423 run when image quality degradation was observed.

## 424 2.2. The LSST Commissioning Camera

425 LSSTComCam (B. Stalder et al. 2022, 2020; J.  
 426 Howard et al. 2018; SLAC National Accelerator Labora-  
 427 tory & NSF-DOE Vera C. Rubin Observatory 2024) is  
 428 a 144-megapixel version of the 3.2-gigapixel LSSTCam.  
 429 It covers approximately 5% of the LSSTCam focal plane  
 430 area, with a field of view of  $\sim 0.5 \text{ deg}^2$  ( $40' \times 40'$ ), com-  
 431 pared to LSSTCam’s  $9.6 \text{ deg}^2$ . It was developed to val-  
 432 idate camera interfaces with other observatory compo-  
 433 nents and evaluate overall system performance prior to  
 434 the start of LSSTCam commissioning. Although LSST-  
 435 ComCam has a smaller imaging area, it shares the same  
 436 plate scale of  $0''.2$  per pixel and is housed in a support  
 437 structure that replicates the mass, center of gravity, and  
 438 physical dimensions of LSSTCam. All mechanical and  
 439 utility interfaces to the telescope are implemented iden-  
 440 tically, enabling full end-to-end testing of observatory  
 441 systems, including readout electronics, image acquisi-  
 442 tion, and data pipelines. Although the LSSTComCam  
 443 cryostat employs a different cooling system (Cryotels) to  
 444 that of LSSTCam, it included a refrigeration pathfinder  
 445 to validate the cryogenic system intended for LSSTCam.

446 The LSSTCam focal plane comprises 25 modular rafts  
 447 arranged in a  $5 \times 5$  grid, of which 21 are science rafts de-  
 448 dicated to imaging and 4 are corner rafts used for guid-  
 449 ing and wavefront sensing. LSSTCam employs CCD  
 450 sensors from two vendors: Imaging Technology Labora-  
 451 tory, University of Arizona (UA) (ITL) and Teledyne  
 452 (E2V). In contrast, LSSTComCam contains only a single  
 453 science raft equipped exclusively with ITL sensors.  
 454 Figure 1 presents a schematic of the LSSTCam focal  
 455 plane, with the LSSTComCam raft positioned at the  
 456 center, corresponding to the LSSTCam central science  
 457 raft location. The perspective is from above, looking  
 458 down through the LSSTComCam lenses onto the focal  
 459 plane.

460 Each science raft is a self-contained unit compris-  
 461 ing nine  $4\text{K} \times 4\text{K}$  Charge-Coupled Device (CCD) (G. E.  
 462 Smith 2010) sensors arranged in a  $3 \times 3$  mosaic, complete  
 463 with integrated readout electronics and cooling systems.  
 464 Each sensor is subdivided into 16 segments arranged in  
 465 a  $2 \times 8$  layout, with each segment consisting of  $512 \times 2048$   
 466 pixels and read out in parallel using individual ampli-  
 467 fiers. This design is identical across all science rafts.  
 468 To maintain uniform performance and calibration, each  
 469 raft is populated exclusively with sensors from a single  
 470 vendor.  
 471



472 **Figure 1.** LSSTComCam focal plane layout illustrating the  
 473 placement of its nine sensors, shown in gray, which form a  
 474 raft. The view is looking down from above the focal plane  
 475 through the LSSTComCam lenses. LSSTComCam is Raft  
 476 R22 (R22). We also indicate the location of the LSSTCam  
 477 sensors (open squares) to highlight the field-of-view of LSST-  
 478 ComCam in relation to that of LSSTCam.

479 LSSTComCam consists of a single science raft, designa-  
 480 ted Raft 22 (R22), equipped solely with ITL sensors.  
 481 These sensors were selected from the best-performing re-  
 482 maining ITL devices after the LSSTCam rafts were fully  
 483 populated. Some exhibit known issues such as high read-  
 484 out noise (e.g., Detector 8) and elevated Charge Transfer  
 485 Inefficiency (CTI) (e.g., Detector 5). Consequently, cer-  
 486 tain image artifacts present in the DP1 dataset may be  
 specific to LSSTComCam. Figure 2 shows the LSST-  
 ComCam R22 focal plane layout and the placement and  
 numbering scheme of sensors (S) and amplifiers (C).  
 This configuration is identical across all science rafts  
 in LSSTCam. The LSSTCam and LSSTComCam focal  
 planes are described in detail in A. A. Plazas Malagón  
 et al. (2026).

### 488 2.2.1. Filter Complement

489 LSSTComCam supports imaging with six broadband  
 490 filters *ugrizy* spanning 320–1050 nm, identical in de-  
 491 sign to LSSTCam. However, its filter exchanger can  
 492 hold only three filters at a time, compared to five with  
 493 LSSTCam. The full-system throughput of the six LSST-  
 494 ComCam filters, which encompasses contributions from  
 495 a standard atmosphere at airmass 1.2, telescope opti-  
 496 cs, camera surfaces, and the mean ITL detector quan-

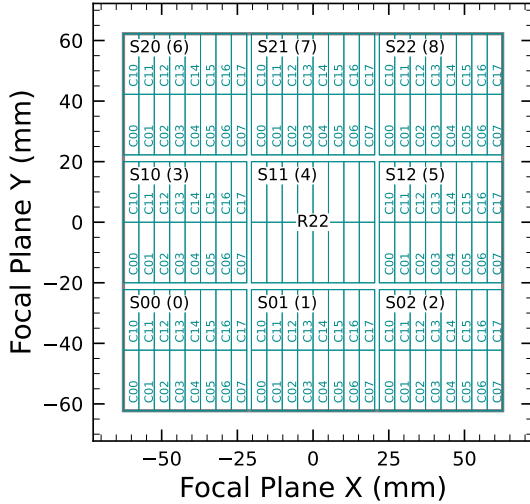


**Figure 2.** LSSTComCam focal plane layout, showing Raft 22 (R22) and the placement and numbering scheme of sensors (S) and amplifiers (C). The view is from above, looking through the LSSTComCam lenses onto the focal plane. Each sensor contains 16 amplifiers, and the raft is composed of a  $3 \times 3$  array of sensors. The detector number for each sensor is indicated in parentheses.

West B with a set of 10 usable 10-second exposures over two nights. EUTELSAT 117 West B is part the Global Positioning System (GPS) system and serves as one of the Wide Area Augmentation System (WAAS) satellites operated for the U.S. Federal Aviation Administration (FAA) and used to broadcast GPS corrections to air traffic.

As these satellites are part of the GPS system, their positions are tracked very precisely and the record of their locations is published after the fact and can be downloaded. Following the technique previously employed by other surveys, (J. L. Tonry et al. 2018), we observed the satellite while tracking the sky and then downloaded the data-files with its precise locations from the National Satellite Test Bed web site<sup>88</sup>. By comparing the measured and predicted locations of the start of the satellite track on the sky, we determined that (relative to the start of integration-time recorded in the Flexible Image Transport System (FITS) headers) our time was accurate to  $53.6 \pm 11.0$  milliseconds.

This work continues to be an area of ongoing study, with the exact timing of when the shutter open command is issued, and the complete profile of the shutter movement not yet determined. However the open command is on average near 29 milliseconds later. Incorporating the delays into the fit reduces the offset to  $24.8 \pm 11.0$  milliseconds.

The full shutter takes approximately 396 milliseconds to completely open. As the LSSTComCam sensors are centered in the aperture, the center of the focal plane should be exposed about half-way through the shutter open procedure, 198 milliseconds after the open command. There are uncertainties on the full motion profile, and the blade direction motions are currently not known, but the fraction of the shutter aperture subtended by the focal plane is 52%. This implies that that the shutter will pass any pixel between  $198 \pm 103$  milliseconds. Subtracting this from the fitted delay of 24.8 milliseconds and adding the fitted error of 11.0 milliseconds in quadrature, results in a current conservative estimate of the delay of  $-173.2 \pm 104.1$  milliseconds, consistent with and smaller than the constraints on the timing offset determined using astrometric residuals from known asteroid associations presented in §5.9.2.

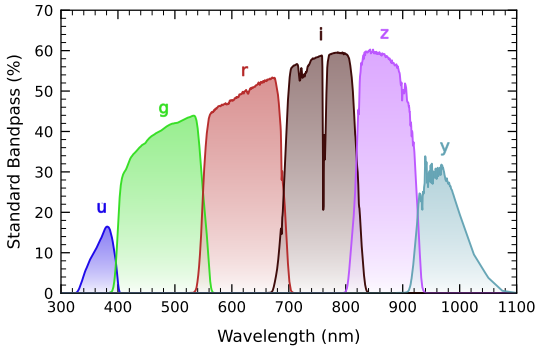


**Figure 3.** LSSTComCam standard bandpasses, illustrating full system throughput. The bandpasses include a standard atmosphere at airmass 1.2, telescope optics, camera surfaces, and mean ITL detector quantum efficiency. The corresponding transmission curves are provided as a DP1 data product.

### 2.2.2. Timing Calibration

The absolute time accuracy of data taken with LSSTComCam relies on the Network Time Protocol (NTP) for clock synchronization, which should be accurate to approximately 1 millisecond. In order to evaluate the absolute timing accuracy of the entire system we observed the geosynchronous satellite EUTELSAT 117

### 2.3. Flat Field System

During the on-sky campaign, key components of the Rubin calibration system (P. Ingraham et al. 2022), including the flat field screen, had not yet been installed. As a result, flat fielding for DP1 relied en-

<sup>88</sup> <https://www.nstb.tc.faa.gov/nstbarchive.html>

558 tirely on twilight flats. While twilight flats pose chal-  
 559 lenges such as non-uniform illumination and star print-  
 560 through, they were the only available option during  
 561 LSSTComCam commissioning and for DP1 processing.  
 562 To mitigate these limitations, dithered, tracked expo-  
 563 sures were taken over a broad range of azimuth and rota-  
 564 tor angles to construct combined flat calibration frames.  
 565 Exposure times were dynamically adjusted to reach tar-  
 566 get signal levels of between 10,000 and 20,000 electrons.  
 567 Future campaigns with LSSTCam will benefit from more  
 568 stable and uniform flat fielding using the Rubin flat field  
 569 system, described in P. Fagrelus & E. S. Rykoff (2025).

#### 2.4. LSST Science Pipelines Commissioning

571 Commissioning of the LSST Science Pipelines, (Rubin  
 572 Observatory Science Pipelines Developers 2025), began  
 573 once the telescope was able to routinely deliver sub-  
 574 arcsecond image quality. The goals included testing the  
 575 internal astrometric and photometric calibration across  
 576 a range of observing conditions, validating the difference  
 577 image analysis and prompt processing (K.-T. Lim 2023)  
 578 framework, and accumulating over 200 visits per band  
 579 to evaluate deep coadded images with integrated expo-  
 580 sure times roughly equivalent to those of the planned  
 581 LSST Wide-Fast-Deep (WFD) 10-year depth. To sup-  
 582 port these goals, seven target fields were selected that  
 583 span a range of stellar densities, overlap with external  
 584 reference datasets, and collectively span the full breadth  
 585 of the four primary LSST science themes. These seven  
 586 fields form the basis of the DP1 dataset. Figure 4 shows  
 587 the locations of these seven fields on the sky, overlaid on  
 588 the LSST baseline survey footprint (R. L. Jones et al.  
 589 2021; P. Yoachim 2022; Rubin’s Survey Cadence Opti-  
 590 mization Committee et al. 2022, 2023, 2025), along with  
 591 the sky coverage of both the LSSTCam and LSSTCom-  
 592 Cam focal planes. Each of the seven target fields was  
 593 observed repeatedly in multiple bands over many nights.  
 594 A typical observing epoch on a given target field con-  
 595 sisted of 5-20 visits in each of the three loaded filters.  
 596 Only images taken as 1x30 second exposures have been  
 597 included in DP1. All images were acquired using the  
 598 Rubin Feature-Based Scheduler (FBS), version 3.0 (E.  
 599 Naghib et al. 2019; P. Yoachim et al. 2024). Table 1 lists  
 600 the seven DP1 fields and their pointing centers, and pro-  
 601 vides a summary of the band coverage in each.

603 Figure 5 shows the temporal sampling of observations  
 604 by filter and by night. The figure indicates the dates  
 605 on which each field was observed in a given band but  
 606 does not convey the total number of observations ob-  
 607 tained per filter on any individual night. Gaps in cov-  
 608 erage across some bands arise from the fact that LSST-  
 609 ComCam can only accommodate three filters at a time

611 (see §2.2). As the campaign progressed, the temporal  
 612 sampling became denser across all fields, reflecting im-  
 613 proved efficiency and increased time allocated for sci-  
 614 ence observations. The Extended Chandra Deep Field-  
 615 South Survey (ECDFS) field received the most consis-  
 616 tent and densest temporal sampling. It is important to  
 617 note that the time sampling in the DP1 dataset differs  
 618 significantly from what will be seen in the final LSST  
 619 data. All fields except for the low ecliptic latitude field,  
 620 Rubin\_SV\_38\_7, used a small random dithering pat-  
 621 tern. The random translational dithers of the telescope  
 622 boresight were applied for each visit, with offsets of up to  
 623 0.2 degrees around the pointing center. The rotational  
 624 dithers of the camera rotator were typically approxi-  
 625 mately 1 degree per visit, with larger random offsets  
 626 at each filter change, which worked to keep operational  
 627 efficiency high. The Rubin\_SV\_38\_7 field used a dif-  
 628 ferent dither pattern to optimize coverage of Solar Sys-  
 629 tem Objects and test Solar System Object linking across  
 630 multiple nights. These observations used a 2x2 grid of  
 631 LSSTComCam pointings to cover an area of about 1.3  
 632 degreex1.3 degrees. The visits cycled between the grid’s  
 633 four pointing centers, each separated by 0.65 degrees,  
 634 and used small random translational dithers to fill chip  
 635 gaps with the goal of acquiring 3-4 visits per pointing  
 636 center per band in each observing epoch. The RA and  
 637 Dec values provided in Table 1 for this field represent  
 638 approximately the center of the four fields.

639 Figure 6 shows sky coverage maps showing the distri-  
 640 bution of visits in each of the seven DP1 fields, color  
 641 coded by band. The images clearly show the focal plane  
 642 chip gaps and dithering pattern. Only the detectors for  
 643 which single frame processing succeeded are included  
 644 in the plots, which explains why the central region of  
 645 47\_Tuc looks thinner than the other fields (see §5.10).  
 646 Table 2 reports the 5 $\sigma$  point source depths for coad-  
 647 ded images per field and per band, where coverage in  
 648 a band is non-zero, together with the expected 10-year  
 649 LSST depths derived from the baseline simulated survey  
 650 (F. B. Bianco et al. 2022).

#### 2.5. Delivered Image Quality

653 The delivered image quality is influenced by contribu-  
 654 tions from both the observing system (i.e., dome, tele-  
 655 scope and camera) and the atmosphere. During the  
 656 campaign, the Rubin Differential Image Motion Monitor  
 657 (DIMM) was not operational, so atmospheric seeing was  
 658 estimated using live data from the Southern Astrophys-  
 659 ical Research Telescope (SOAR) Ring-Image Next Gen-  
 660 eration Scintillation Sensor (RINGSS) seeing monitor,  
 661 also located on Cerro Pachón. Although accelerometers  
 662 mounted on the mirror cell and top-end assembly were

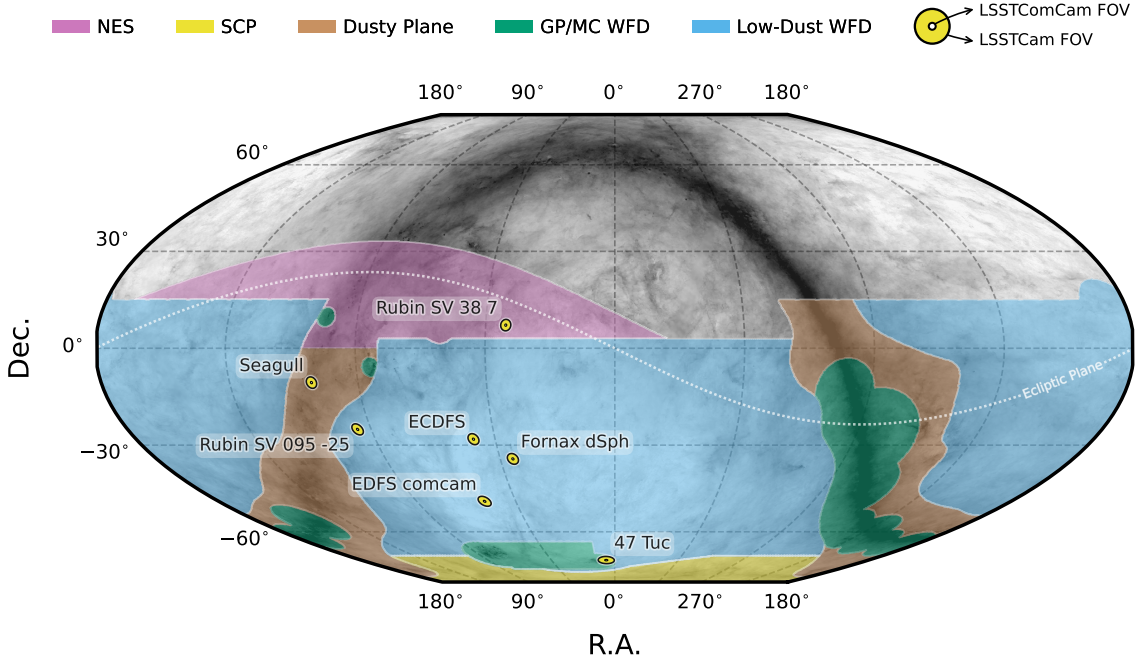


**Figure 4.** Locations of the seven DP1 fields overlaid on the LSST baseline survey footprint. NES: North Ecliptic Spur; SCP: South Celestial Pole; Low-Dust WFD: regions away from the Galactic Plane (GP) observed with a WFD cadence; GP/MC WFD: Galactic Plane and Magellanic Clouds regions observed with a WFD cadence. The fields of view of the LSSTCam and LSSTComCam focal planes are shown as concentric yellow circles about the pointing center of each field. The background Milky Way dust map is based on the FDS model (D. P. Finkbeiner et al. 1999).

**Table 1.** DP1 fields and pointing centers with the number of exposures in each band per field. ICRS coordinates are in units of decimal degrees, and are specified as J2000.

| Field Code       | Field Name                           | RA      | Dec     | Band     |          |          |          |          | Total |          |
|------------------|--------------------------------------|---------|---------|----------|----------|----------|----------|----------|-------|----------|
|                  |                                      |         |         | <i>u</i> | <i>g</i> | <i>r</i> | <i>i</i> | <i>z</i> |       | <i>y</i> |
| 47_Tuc           | 47 Tucanae Globular Cluster          | 6.128   | -72.090 | 6        | 10       | 32       | 19       | 0        | 5     | 72       |
| ECDFS            | Extended Chandra Deep Field South    | 53.160  | -28.100 | 43       | 230      | 237      | 162      | 153      | 30    | 855      |
| EDFS_comcam      | Rubin SV Euclid Deep Field South     | 59.150  | -48.730 | 20       | 61       | 87       | 42       | 42       | 20    | 272      |
| Fornax_dSph      | Fornax Dwarf Spheroidal Galaxy       | 40.080  | -34.450 | 0        | 5        | 25       | 12       | 0        | 0     | 42       |
| Rubin_SV_095_-25 | Rubin SV Low Galactic Latitude Field | 95.040  | -25.000 | 33       | 82       | 84       | 23       | 60       | 10    | 292      |
| Rubin_SV_38_7    | Rubin SV Low Ecliptic Latitude Field | 37.980  | 7.015   | 0        | 44       | 40       | 55       | 20       | 0     | 159      |
| Seagull          | Seagull Nebula                       | 106.300 | -10.510 | 10       | 37       | 43       | 0        | 10       | 0     | 100      |
| Total            |                                      |         |         | 112      | 469      | 548      | 313      | 285      | 65    | 1792     |

663 available to track dynamic optics effects, such as mir-  
 664 ror oscillations that can degrade optical alignment, this  
 665 data was not used during the campaign. Mount encoder  
 666 data were used to measure the mount jitter in every im-  
 667 age, with a measured median contribution of 0.004 arc-  
 668 seconds to image degradation. As the pointing model  
 669 was not fine tuned, tracking errors could range from 0.2  
 670 to 0.4 arcseconds per image, depending on RA and Dec.

671 Dome and mirror-induced seeing were not measured dur-  
 672 ing the campaign.

673 The DP1 median delivered image quality, quantified  
 674 as the PSF at FWHM across all filters and target fields,  
 675 is  $1''.14$ . The best images achieve a PSF FWHM of ap-  
 676 proximately  $0''.58$ . Both the per-sensor PSF FWHM and  
 677 the overall median vary depending on the filter and the  
 678 specific target field. The median delivered image quality  
 679 per band and target field is provided in Table 3. Fig-

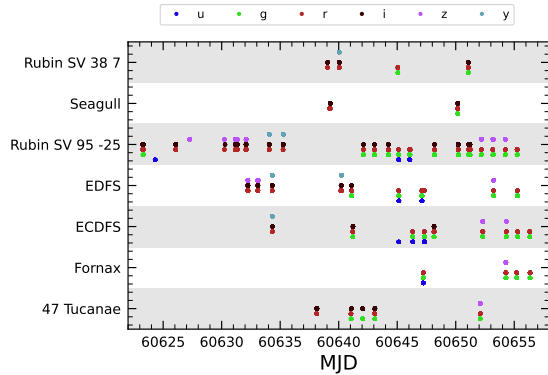


**Figure 5.** Temporal distribution of DP1 observations, grouped by field as a function of Modified Julian Date (MJD) and color-coded by filter. Each point indicates that a given field was observed at least once in the corresponding filter on that date.

**Table 2.** DP1 median  $5\sigma$  coadded point-source detection limits per field and band, expressed in magnitudes, compared with the expected 10-year LSST values derived from the baseline simulated survey (F. B. Bianco et al. 2022).

| Field Code       | Band     |          |          |          |          |          |
|------------------|----------|----------|----------|----------|----------|----------|
|                  | <i>u</i> | <i>g</i> | <i>r</i> | <i>i</i> | <i>z</i> | <i>y</i> |
| 47_Tuc           | -        | 24.03    | 24.24    | 23.90    | -        | 21.79    |
| ECDFS            | 24.55    | 26.18    | 25.96    | 25.71    | 25.07    | 23.10    |
| EDFS_comcam      | 23.42    | 25.77    | 25.72    | 25.17    | 24.47    | 23.14    |
| Fornax_dSph      | -        | 24.53    | 25.07    | 24.64    | -        | -        |
| Rubin_SV_095_-25 | 24.29    | 25.46    | 24.95    | 24.86    | 24.32    | 22.68    |
| Rubin_SV_38_7    | -        | 25.46    | 25.15    | 24.86    | 23.52    | -        |
| Seagull          | 23.51    | 24.72    | 24.19    | -        | 23.30    | -        |
| LSST 10-year     | 25.73    | 26.86    | 26.88    | 26.34    | 25.63    | 24.87    |

**Table 3.** DP1 Median image quality per field and per band quantified as the PSF at FWHM in arcseconds.

| Field Code       | Band     |          |          |          |          |          | All  |
|------------------|----------|----------|----------|----------|----------|----------|------|
|                  | <i>u</i> | <i>g</i> | <i>r</i> | <i>i</i> | <i>z</i> | <i>y</i> |      |
| 47_Tuc           | -        | 1.27     | 1.25     | 1.11     | -        | 1.33     | 1.22 |
| ECDFS            | 1.40     | 1.14     | 1.08     | 1.00     | 1.00     | 1.07     | 1.08 |
| EDFS_comcam      | 1.88     | 1.25     | 1.20     | 1.10     | 1.18     | 0.99     | 1.19 |
| Fornax_dSph      | -        | 1.16     | 0.82     | 0.93     | -        | -        | 0.85 |
| Rubin_SV_095_-25 | 1.40     | 1.25     | 1.14     | 0.97     | 1.17     | 0.82     | 1.19 |
| Rubin_SV_38_7    | -        | 1.13     | 1.13     | 1.10     | 1.22     | -        | 1.13 |
| Seagull          | 1.50     | 1.34     | 1.19     | -        | 1.19     | -        | 1.25 |
| All              | 1.48     | 1.17     | 1.12     | 1.03     | 1.11     | 1.01     | 1.13 |

### 3. OVERVIEW OF THE CONTENTS OF RUBIN DP1

In this section we describe the Rubin DP1 data products and provide summary statistics for each. For more detailed information, we refer the reader to the DOI-registered DP1 release documentation available at <https://dp1.lsst.io> and the catalog schemas available at <https://sdm-schemas.lsst.io>.<sup>89</sup>

The DP1 science data products are derived from the 15972 individual CCD images taken across 1792 exposures in the seven LSSTComCam commissioning fields (§2.4). To aid legibility, we have separated the descriptions of the data products from the description of the data release processing pipeline (§4). Similarly, as the DP1 data products can be accessed via one or both of International Virtual Observatory Alliance (IVOA) Services (§6.2.1) or the Data Butler (§6.2.2), we describe them here in a manner that is agnostic to the means of access.

The data products that comprise DP1 provide an early preview of future LSST data releases and are strongly dependent on the type and quality of the data that was collected during the LSSTComCam on-sky campaign (§2.4). Consequently not all anticipated LSST data products, as described in the Data Product Definition Document (DPDD) (M. Jurić et al. 2023), were produced for the DP1 dataset.

Rubin Observatory has adopted the convention by which single-epoch detections are referred to as “Sources”, and the astrophysical object associated with

<sup>89</sup> Searchable catalog schemas are also available to Data Rights Holders via the Rubin Science Platform at <https://data.lsst.cloud>.

ure 7 shows the distribution of PSF FWHM (in arcsec) over all 16071 individual sensors images. Ongoing efforts aim to quantify all sources of image degradation, including contributions from the camera system; static and dynamic optical components; telescope mount motion; observatory-induced seeing from the dome and primary mirror; and atmospheric conditions. For the LSST, the design specification for the median delivered image quality, referenced to the zenith and 550 nm, is  $0''.7$ . This value corresponds to the measured median atmospheric seeing at the Cerro Pachón site and a system contribution to delivered image quality of  $0''.35$  added in quadrature.

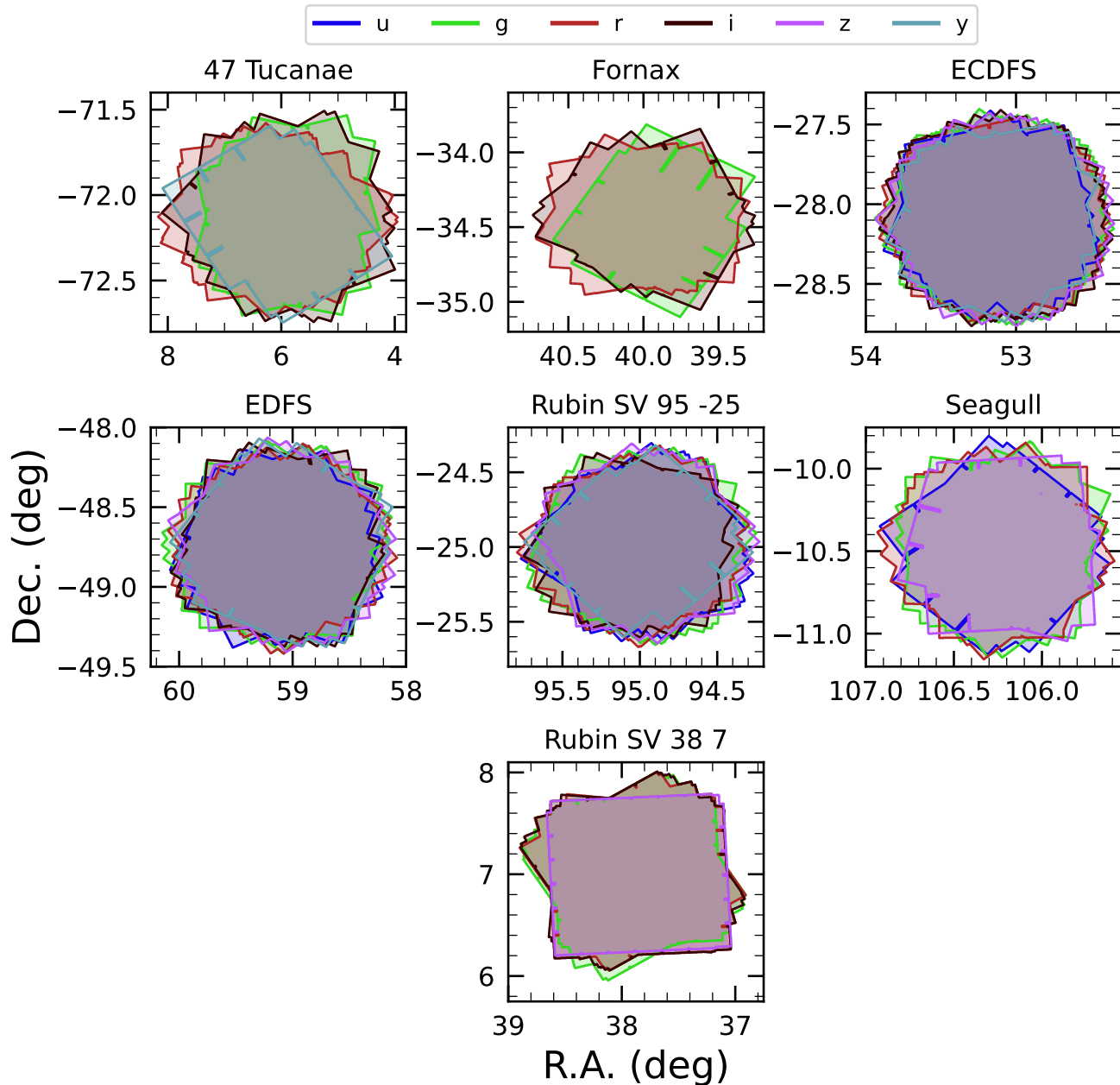


**Figure 6.** Sky coverage maps showing the distribution of visits in each field, color coded by band. The images clearly show the focal plane chip gaps and dithering pattern. Only the detectors for which single frame processing succeeded are included in the plots, which explains why the central region of 47\_Tuc looks thinner than the other fields.

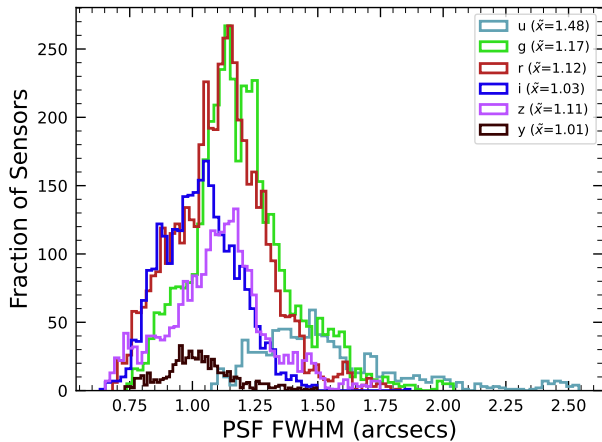
724 a given detection is referred to as an “Object”<sup>90</sup>. As 729  
 725 such, a given Object will likely have multiple associated 730  
 726 Sources, since it will be observed in multiple epochs. 731

727 At the highest level, the DP1 data products fall into  
 728 one of five types:

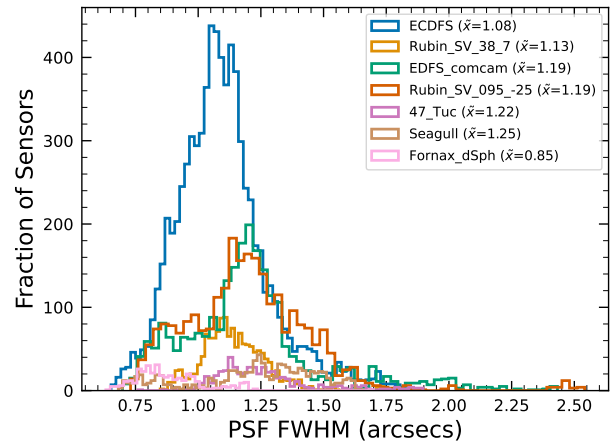
- **Science Images**, including single-epoch images, deep and template coadded images, and difference images (§3.1);

- **Catalogs** of astrophysical Sources and Objects detected and measured in the aforementioned images. We also provide the astrometric and photometric reference catalog generated from external

<sup>90</sup> We caution that this nomenclature is not universal; for example, some surveys use “detections” for what we call “sources”, and “sources” for what we call “objects”.



(a) PSF FWHM (arcsecs) per passband across all DP1 target fields.



(b) PSF FWHM (arcsecs) per DP1 target field across all passbands

**Figure 7.** Histograms showing the distribution of delivered image quality for all 16071 single-epoch individual sensors in the DP1 dataset per passband (a) and per field (b). The median values are given in the legend.

736 sources that was used during processing to gener-  
737 ate the DP1 data products (§3.2);

- 738 • **Maps**, which provide non-science-level visualiza-  
739 tions of the data within the release. They include,  
740 for example, zoomable multi-band images and cover-  
741 age maps (§3.4.1);
- 742 • **Ancillary data products**, including, for exam-  
743 ple, the parameters used to configure the data pro-  
744 cessing pipelines, log and processing performance  
745 files, and **calibration** data products (§3.6);
- 746 • **Metadata** in the form of tables containing infor-  
747 mation about each visit and processed image, such  
748 as pointing, exposure time, and a range of image  
749 quality summary statistics (§3.5).

750 While images and catalogs are expected to be the pri-  
751 mary data products for scientific research, we also rec-  
752 ognize the value of providing access to other data types  
753 to support investigations and ensure transparency.

754 To facilitate processing, Rubin DP1 uses a single  
755 skymap<sup>91</sup> that covers the entire sky area encompass-  
756 ing the seven DP1 fields. The DP1 skymap divides the  
757 entire celestial sphere into 18938 **tracts**, each covering  
758 approximately  $2.8 \text{ deg}^2$ . The **tracts** are arranged in rings  
759 of declination, ordered from south to north, then with  
760 increasing right ascension within a ring. Each **tract** is  
761 further subdivided into  $10 \times 10$  equally-sized patches.

<sup>91</sup> A skymap is a tiling of the celestial sphere, organizing large-  
scale sky coverage into manageable sections for processing and  
analysis. While the skymap described here is specific to DP1,  
we do not anticipate major changes to the skymap in future  
data releases.

762 Both **tracts** and patches overlap with their neighboring  
763 regions. The amount of overlap between **tracts** changes  
764 with declination, with **tracts** nearest the poles having  
765 the greatest degree of overlap; the minimum overlap be-  
766 tween **tracts** is  $1'0$ . By contrast, the amount of overlap  
767 between patches is constant, with each **patch** overlap-  
768 ping each of its neighbouring patches by  $80'0$ . Each  
769 patch covers  $0.036 \text{ deg}^2$  which, due to the patch over-  
770 lap, is slightly larger than the tract area divided by the  
771 number of patches in a tract. The aerial coverage of  
772 a patch is comparable to, but somewhat smaller than,  
773 the  $0.058 \text{ deg}^2$  field-of-view of a single LSSTComCam or  
774 LSSTComCam detector, meaning each detector image spans  
775 multiple patches. The size of a tract is larger than the  
776 LSSTComCam field of view. However, since each ob-  
777 served field extends across more than one tract, each  
778 field covers multiple tracts.

779 The skymap is integral to the production of co-added  
780 images. To create a coadded image, the processing  
781 pipeline selects all calibrated science images in a given  
782 field that meet specific quality thresholds (§3.1 and  
783 §4.5.1) for a given **patch**, warps them onto a single  
784 consistent pixel grid for that **patch**, as defined by the  
785 skymap, then coadds them. Each individual coadd im-  
786 age therefore covers a single **patch**.

787 Throughout this section, the data product names are  
788 indicated using monospace font. Data products are ac-  
789 cessed via either the IVOA Services (§6.2.1) or the Data  
790 Butler (§6.2.2).

### 3.1. Science Images

792 Science images are exposures of the night sky, as dis-  
793 tinct from **calibration** images (§3.6.3). Although the re-  
794 lease includes **calibration** images, thereby allowing users

**Table 4.** Number of **raw** images per field and band. Each raw image corresponds to a single 30-second LSSTComCam exposure on one CCD. Most exposures produce nine raw images, one per sensor in the focal plane, however some yield fewer due to occasional hardware or readout issues.

| Field Code       | Band     |          |          |          |          |          | Total |
|------------------|----------|----------|----------|----------|----------|----------|-------|
|                  | <i>u</i> | <i>g</i> | <i>r</i> | <i>i</i> | <i>z</i> | <i>y</i> |       |
| 47_Tuc           | 54       | 90       | 288      | 171      | 0        | 45       | 648   |
| ECDFS            | 387      | 2070     | 2133     | 1455     | 1377     | 270      | 7692  |
| EDFS_comcam      | 180      | 549      | 783      | 378      | 378      | 180      | 2448  |
| Fornax_dSph      | 0        | 45       | 225      | 108      | 0        | 0        | 378   |
| Rubin_SV_095_-25 | 297      | 738      | 756      | 207      | 540      | 90       | 2628  |
| Rubin_SV_38_7    | 0        | 396      | 360      | 495      | 180      | 0        | 1431  |
| Seagull          | 90       | 333      | 387      | 0        | 90       | 0        | 900   |
| Total            | 1008     | 4221     | 4932     | 2814     | 2565     | 585      | 16125 |

to reprocess the raw images if needed, this is expected to be necessary only in rare cases. Users are strongly encouraged to start from the `visit_image` provided. The data product names shown here are those used by the Data Butler, but the names used in the IVOA Services differ only slightly in that they are prepended by “`lsst.`”.

### 3.1.1. Raw Image

**raw** images (NSF-DOE Vera C. Rubin Observatory 2025b) are unprocessed data received directly from the camera. Each **raw** corresponds to a single CCD from a single LSSTComCam exposure of 30 s duration. Each LSSTComCam exposure typically produces up to nine **raws**, one per sensor in the focal plane. However, a small number of exposures resulted in fewer than nine **raw** images due to temporary hardware issues or readout faults.

In total, DP1 includes 16125 raw images. Table 4 provides a summary by target and band. A **raw** contains  $4608 \times 4096$  pixels, including prescan and overscan, and occupies around 18 MB of disk space.<sup>92</sup> The field of view of a single **raw**, excluding prescan and overscan regions, is roughly  $0^\circ 23' \times 0^\circ 22' \approx 0.051 \text{ deg}^2$ , corresponding to a plate scale of  $0''.2$  per pixel.

<sup>92</sup> Each amplifier image contains 3 and 64 columns of serial prescan and overscan pixels, respectively, and 48 rows of parallel overscan pixels, meaning a **raw** contains  $4072 \times 4000$  exposed pixels.

### 3.1.2. Visit Image

`visit_images` (NSF-DOE Vera C. Rubin Observatory 2025c) are fully-calibrated processed images. They have undergone instrument signature removal (§4.2.1) and all the single frame processing steps described in §4.2 which are, in summary: PSF modeling, background subtraction, and astrometric and photometric calibration. As with **raws**, a `visit_image` contains processed data from a single CCD resulting from a single 30 s LSSTComCam exposure. As a consequence, a single LSSTComCam exposure typically results in nine `visit_images`. The handful of exposures with fewer than nine **raw** images also have fewer than nine `visit_images`, but there are an additional 153 **raw** images that failed processing and for which there is thus no corresponding `visit_image`. The majority of failures – 131 in total – were due to challenges with astrometric fits or PSF models in the 47\_Tuc crowded field. The other failures were in the Rubin\_SV\_095\_-25 (9 failures), ECDFS (8), Fornax\_dSph (3), and EDFs\_comcam (2) fields.

In total, there are 15972 `visit_images` in DP1. Each `visit_image` comprises three images: a calibrated science image, a variance image, and a pixel-level bit-mask that flags issues such as saturation, cosmic rays, or other artifacts. Each `visit_image` also contains a position-dependent PSF model, World Coordinate System (WCS) information, and various metadata providing information about the observation and processing. The science and variance images and the pixel mask each contain  $4072 \times 4000$  pixels. In total, a single `visit_image`, including all extensions and metadata, occupies around 110 MB of disk space. A plot showing the normalized cumulative histogram of the  $5\sigma$  depths of all the `visit_images` in DP1 is shown in Figure 8.

### 3.1.3. Deep Coadd

`deep_coadds` are created on a per-band basis, meaning only data from exposures taken with a common filter are coadded. As such, there are up to six `deep_coadds` covering each `patch` – one for each of the six LSSTComCam bands. The process of producing `deep_coadds` is described in §4.5 but, to summarize, it involves the selection of suitable `visit_images` (both in terms of `patch` coverage, band, and image quality), the warping of those `visit_images` onto a common pixel grid, and the co-adding of the warped `visit_images`. To be included in a DP1 `deep_coadd`, a `visit_image` needed to have a PSF FWHM smaller than  $1''.7$ . Of the 15972 `visit_images`, 15375 satisfied this criterion and were therefore used to create `deep_coadds`.

There are a total of 2644 `deep_coadds` in DP1. As mentioned above, a single `deep_coadd` covers one `patch`,

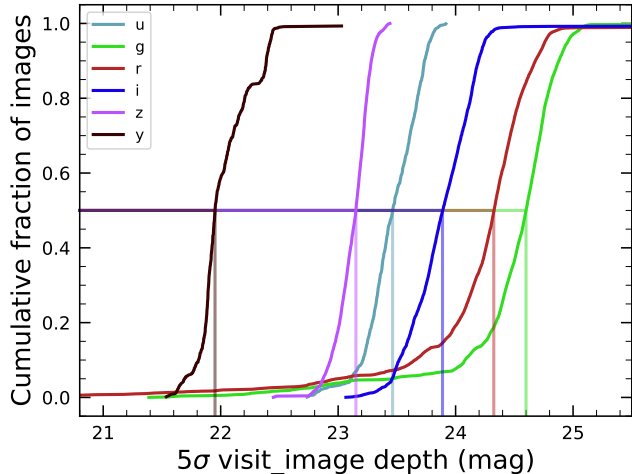


**Figure 8.** Normalized cumulative histograms of the  $5\sigma$  depths of all `visit_images` in each band. The vertical lines indicate the 50th percentiles for each band (see legend).

and includes a small amount of overlap with its neighboring `patch`. The skymap used for DP1 defines a `patch` as having an on-sky area of  $0.028 \text{ deg}^2$  excluding overlap, and  $0.036 \text{ deg}^2$  including overlap. A single `deep_coadd` – including overlap – contains  $3400 \times 3400$  equal-sized pixels, corresponding to a platescale of  $0''.2$  per pixel. Each `deep_coadd` contains the science image (i.e., the coadd), a variance image, and a pixel mask; all three contain the same number of pixels. Each `deep_coadd` also contains a position-dependent PSF model (which is the weighted sum of the PSF models of the input `visit_images`), WCS information, plus various `meta-data`.

The number of `visit_images` that contributed to a given `deep_coadd` varies across the patch; the Survey Property Maps can be consulted to gain insights into the total exposure time at all locations covered by the survey. Similarly, since coadds always cover an entire `patch`, it is common for a `deep_coadd` to contain regions that were not covered by any of the selected `visit_images`, particularly if the `patch` is on the outskirts of a field and was thus not fully observed. By the nature of how coadds are produced, such regions may contain seemingly valid `flux` values (i.e., not necessarily zeros or NaNs), but will instead be flagged with the `NO_DATA` flag in the pixel mask. It is therefore crucial that the pixel mask be referred to when analyzing `deep_coadds`.

#### 3.1.4. Template Coadd

`template_coadds` (NSF-DOE Vera C. Rubin Observatory 2025d) are those created to use as templates for difference imaging, i.e., the process of subtracting a template image from a `visit_image` to identify either vari-

able or `transient` objects. It should be noted, however, that `template_coadds` are not themselves subtracted from `visit_images` but are, instead, warped to match the WCS of a `visit_image`. It is this warped template that is subtracted from the `visit_image` to create a difference image.<sup>93</sup> As with `deep_coadds`, `template_coadds` are produced by warping and co-adding multiple `visit_images` covering a given skymap-defined `patch`. The process of building `template_coadds` is the same as that for `deep_coadds`, but the selection criteria differ between the two types of coadd. In the case of `template_coadds`, one third of `visit_images` covering the `patch` in question with the narrowest PSF FWHM are selected. If one third corresponds to fewer than twelve `visit_images` (i.e., there are fewer than 36 `visit_images` covering the `patch`), then the twelve `visit_images` with the narrowest PSF FWHM are selected. Finally, if there are fewer than twelve `visit_images` covering the `patch`, then all `visit_images` are selected. Of the 15972 `visit_images`, 13113 were used to create `template_coadds`. This selection strategy is designed to optimize for seeing when a `patch` is well-covered by `visit_images`, yet still enable the production of `template_coadds` for poorly-covered patches. As with `deep_coadds`, the number of `visit_images` that contributed to a `template_coadd` varies across the patch.

DP1 contains a total of 2730 `template_coadds`.<sup>94</sup> As with `deep_coadds`, a single `template_coadd` covers a single `patch`. Since the same skymap is used when creating both `deep_coadd` and `template_coadds`, the on-sky area and pixel count of `template_coadds` are the same as that of a `deep_coadd` (see above). Similarly, `template_coadds` contain the science image (i.e., the coadd), a variance image, and a pixel mask; all three contain the same number of pixels. Also included are the PSF model, WCS information, and `metadata`. As is the case for `deep_coadds`, those pixels within `template_coadds` that are not covered by any of the selected `visit_images` may still have seemingly valid values, but are indicated with the `NO_DATA` flag within the pixel mask.

#### 3.1.5. Difference Image

`difference_images` (NSF-DOE Vera C. Rubin Observatory 2025e) are generated by the subtraction of the warped, scaled, and PSF-matched `template_coadd`

<sup>93</sup> For storage space reasons, warped templates are not retained for DP1, as they can be readily and reliably recreated from the `template_coadds`.

<sup>94</sup> The difference in the number of `deep_coadds` and `template_coadds` is due to the difference in the `visit_image` selection criteria for each coadd.

from the `visit_image` (see §4.6.1). In principle, only those sources whose `flux` has changed relative to the `template_coadd` should be apparent (at a significant level) within a `difference_image`. In practice, however, there are numerous spurious sources present in `difference_images` due to unavoidably imperfect template matching.

In total, there are 15972 `difference_images` in DP1, one for each `visit_image`.

Like `visit_images`, `difference_images` contain the science (i.e., difference) image, a variance image, and a pixel mask; all three contain the same number of pixels, which is the same as that of the input `visit_image`. Also included is the PSF model, WCS information, and `metadata`.

### 3.1.6. Background Images

Background images contain the model `background` that has been generated and removed from a science image. `visit_images`, `deep_coadds` and `template_coadds` all have associated `background` images.<sup>95</sup> Background images contain the same number of pixels as their respective science image, and there is one `background` image for each `visit_image`, `deep_coadd`, and `template_coadd`. Difference imaging analysis also measures and subtracts a `background` model, but the `difference_background` data product is not written out by default and is not part of DP1.

Background images are not available via the IVOA Service; they can only be accessed via the Butler Data Service.

## 3.2. Catalogs

In this section we describe science-ready tables produced by the science pipelines. All catalogs contain data for detections in the images described in §3.1, except the `Calibration` catalog, which contains reference data obtained from previous surveys. Observatory-produced `metadata` tables are described in §3.5.

The catalogs contains measurements for either Sources detected in `visit_images` and `difference_images`, or Objects detected in `deep_coadds`. All catalogs store fluxes rather than magnitudes, with fluxes measured in nanojansky ( $1 \text{ nJy} = 10^{-35} \text{ Wm}^{-2}\text{Hz}^{-1}$ ). Fluxes are preferred for multi-epoch observations, as they can be averaged across epochs, unlike magnitudes. Additionally, flux measurements on difference images (§3.1) are computed against a template, representing a flux difference. As a result, flux measurements on difference

images can be negative, particularly for faint sources in the presence of noise.

The `Source`, `Object`, `ForcedSource`, `DiaSource`, `DiaObject`, and `ForcedSourceOnDiaObject` catalogs described below each vary in terms of their specific columns but generally contain: one or more unique identification numbers, positional information, multiple types of `flux` measurements (e.g., aperture fluxes, PSF fluxes, Gaussian fluxes, etc.), and a series of boolean flags indicating characteristics such as saturation or cosmic ray contamination for each source/object. The Solar System catalogs `SSObject` and `SSSource` deviate from this general structure in that they instead contain orbital parameters for all known asteroids.

Where applicable, quantities are prefixed with the band in which they were measured, and all measured properties are reported with their associated  $1\sigma$  uncertainties. For example, `g_ra` and `g_raErr` refer to right ascension and its uncertainty, measured in the g-band.

Fluxes for various apertures are provided together with an uncertainty and a flag, and named in the format `[band]_ap[size]Flux`, where `[size]` is the aperture diameter in pixels. For example, `g_ap03Flux`, `g_ap03FluxErr`, `g_ap03Flux_flag` provide the flux, uncertainty and flag measured within a 3.0-pixel aperture in the g-band. Similarly for flux measurements using difference algorithms, e.g. `g_psfFlux` provides the flux derived using the PSF model as a weight function, forced on g-band.

A complete list of columns with description and units for all tables in DP1 is available at <https://sdm-schemas.lsst.io/dp1.html> Since DP1 is a preview release, it does not include all the catalogs expected in a full LSST Data Release. Additionally, some catalogs may be missing columns, as not all quantities have been computed yet. These quantities will be included in future releases, and, where it is known to be the case, missing data are noted in the catalog descriptions that follow.

Catalog data are stored in the Qserv database (§6.5.1) and are accessible via Table Access Protocol (IVOA standard) (IVOA), and an online DP1 catalog schema is available at <https://sdm-schemas.lsst.io/dp1.html>. Catalog data are also accessible via the Data Butler (see §6.2.2).

### 3.2.1. Source Catalog

The `Source` catalog (NSF-DOE Vera C. Rubin Observatory 2025f) contains data on all sources which are, prior to deblending (§4.5.2), detected with a greater than  $5\sigma$  significance in each individual visit. The detections reported in the `Source` catalog have undergone deblending; in the case of blended detections, only the

<sup>95</sup> In future data releases, `background` images may be included as part of their respective science image data product.

deblended sources are included in the `Source` catalog. It is important to note that while the criterion for inclusion in a `Source` catalog is a  $> 5\sigma$  detection in a `visit_image` prior to deblending, the positions and fluxes are reported post-deblending. Hence, it is possible for the `Source` catalog to contain sources whose flux-to-error ratios – potentially of all types (i.e., aperture flux, PSF flux, etc.) – are less than 5.

In addition to the general information mentioned above (i.e., IDs, positions, fluxes, flags), the `Source` catalog also includes basic `shape` and extendedness information.

The `Source` catalog contains data for 46 million sources in DP1.

A cumulative histogram showing the PSF magnitudes of all sources contained within the `Source` catalogue is presented in the top panel of Figure 9

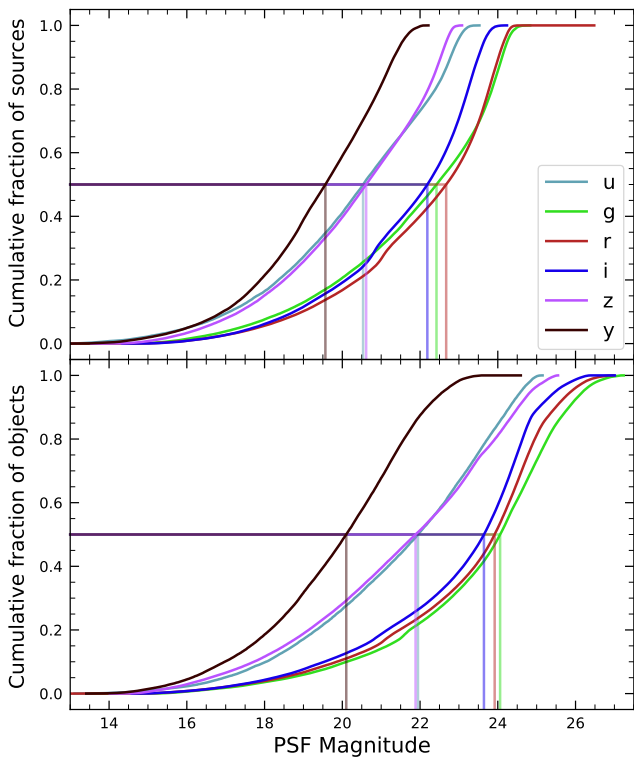


**Figure 9.** Normalized cumulative histograms of the PSF magnitudes of all  $> 5\sigma$ -detected sources (top panel) and objects (bottom panel) contained in the `Source` and `Object` catalogs, respectively, separated according to band (see legend). The vertical lines indicate the 50th percentile for each band.

### 3.2.2. Object Catalog

The `Object` catalog (NSF-DOE Vera C. Rubin Observatory 2025g) contains data on all objects detected with a greater than  $5\sigma$  significance in the `deep_coadds`.

With coadd images produced on a per-band basis, a  $> 5\sigma$  detection in one or more of the bands will result in an object being included in the `Object` catalog. For cases where an object is detected at  $> 5\sigma$  in more than one band, a cross-matching has been performed between bands to associate an object in one band with its counterpart(s) in the other bands. As such, the `Object` catalog contains data from multiple bands. The objects reported in the `Object` catalog have also undergone deblending; in the case of blended detections, only the deblended child objects are included in the catalog. As with the `Source` catalog, the criterion for inclusion in the `Object` catalog is a  $> 5\sigma$  detection in one of the `deep_coadds` prior to deblending, yet the positions and fluxes of objects are reported post-deblending. Hence, it is possible for `Object` catalog to contain objects whose flux-to-error ratios — potentially of all types and in all bands — are less than 5.

In addition to the general information mentioned above (i.e., IDs, positions, fluxes, flags), the `Object` catalog also includes basic `shape` and extendedness information. While they may be included in future data releases, no photometric redshifts, Petrosian magnitudes (V. Petrosian 1976), proper motions or periodicity information are included in the DP1 object catalogs.

The `Object` catalog contains data for 2.3 million objects in DP1.

### 3.2.3. ForcedSource Catalog

The `ForcedSource` catalog (NSF-DOE Vera C. Rubin Observatory 2025h) contains forced PSF photometry measurements performed on both `difference_images` (i.e., the `psfDiffFlux` column) and `visit_images` (i.e., the `psfFlux` column) at the positions of all the objects in the `Object` catalog, to allow assessment of the time variability of the fluxes. We recommend using the `psfDiffFlux` column when generating light curves because this quantity is less sensitive to flux from neighboring sources than `psfFlux`. In addition to forced photometry PSF fluxes, a number of boolean flags are also included in the `ForcedSource` catalog.

The `ForcedSource` catalog contains a total of 269 million entries across 2.3 million unique objects.

### 3.2.4. DiaSource Catalog

The `DiaSource` catalogs (NSF-DOE Vera C. Rubin Observatory 2025i) contains data on all the sources detected at  $> 5\sigma$  significance — including those associated with known Solar System objects — in the `difference_images`. Unlike sources detected in `visit_images`, sources detected in difference images (hereafter, “DiaSource”) have gone through an association step in which an attempt has been made to associate them into

underlying objects called “DiaObject”. The `DiaSource` catalog consolidates all this information across multiple visits and bands. The detections reported in the `DiaSource` catalog have not undergone deblending.

The `DiaSource` catalog contains data for 3.1 million `DiaSources` in [DP1](#).

### 3.2.5. *DiaObject Catalog*

The `DiaObject` catalog ([NSF-DOE Vera C. Rubin Observatory 2025j](#)) contains the astrophysical objects that `DiaSources` are associated with (i.e., the `DiaObjects`). The `DiaObject` catalog contains only non-Solar System Objects; Solar System Objects are, instead, recorded in the `SSObject` catalog. When a `DiaSource` is identified, the `DiaObject` and `SSObject` catalogs are searched for objects to associate it with. If no association is found, a new `DiaObject` is created and the `DiaSource` is associated to it. Along similar lines, an attempt has been made to associate `DiaObjects` across multiple bands, meaning the `DiaObject` catalog, like the `Object` catalog, contains data from multiple bands. Since `DiaObjects` are typically [transient](#) or variable (by the nature of their means of detection), the `DiaObject` catalog contains summary statistics of their fluxes, such as the mean and standard deviation over multiple epochs; users must refer to the `ForcedSourceOnDiaObject` catalog (see below) or the `DiaSource` catalog for single [epoch flux](#) measurements of `DiaObjects`.

The `DIAObject` catalog contains data for 1.1 million `DiaObjects` in [DP1](#).

### 3.2.6. *ForcedSourceOnDiaObject Catalog*

The `ForcedSourceOnDiaObject` catalog ([NSF-DOE Vera C. Rubin Observatory 2025k](#)) is equivalent to the `ForcedSource` catalog, but contains [forced photometry](#) measurements obtained at the positions of all the `DiaObjects` in the `DiaObject` catalog.

The `ForcedSourceOnDiaObject` catalog contains a total of 197 million entries across 1.1 million unique `DiaObjects`.

## 3.3. *SSObject Catalog*

The `SSObject` catalog ([NSF-DOE Vera C. Rubin Observatory 2025l](#)) and the [Minor Planet Center Orbit database \(MPCORB\)](#) carry information about solar system objects. The `MPCORB` table provides the [Minor Planet Center](#)-computed orbital elements for all known asteroids, including those that Rubin discovered. For [DP1](#), the `SSObject` catalog serves primarily to provide the mapping between the [International Astronomical Union \(IAU\)](#) designation of an object (listed in `MPCORB`), and the internal `ssObjectId` identifier,

which is used as a key to find solar system object observations in the `DiaSource` and `SSSource` tables. The `SSObject` catalog contains data for 431 `SSObjects` in [DP1](#).

### 3.3.1. *SSSource Catalog*

The `SSSource` catalog ([NSF-DOE Vera C. Rubin Observatory 2025m](#)) contains data on all `DiaSources` that are either associated with previously-known Solar System Objects, or have been confirmed as newly-discovered Solar System Objects by confirmation of their orbital properties. As entries in the `SSSource` catalog stem from the `DiaSource` catalog, they have all been detected at  $> 5\sigma$  significance in at least one band. The `SSSource` catalog contains data for 5988 Solar System Sources.

### 3.3.2. *CcdVisit Catalog*

The `CcdVisit` catalog ([NSF-DOE Vera C. Rubin Observatory 2025n](#)) contains data for all `CCD` images from a single visit. In principle, this means nine entries per visit, however due to a variety of technical reasons, not all `CCDs` have data for each visit, and so the catalog may contain fewer than nine entries per visit. In addition to technical information, such as the on-sky coordinates of the central pixel and measured pixel scale, the `CcdVisit` catalog contains a range of data quality measurements, such as whole-image summary statistics for the `PSF` size, zeropoint, sky [background](#), sky noise, and quality of astrometric solution. It provides an efficient method to access `visit_image` properties without needing to access the image data. When combined with the data contained in the `Visit` table described in [§3.5](#), it provides a full picture of the telescope pointing and sky conditions at the time of observation.

The `CcdVisit` catalog contains 16071 entries (nine entries for each of the 1786 visits, minus three entries for one incomplete visit). This differs from the number of `visit_images` due to the more stringent requirements imposed to generate a science-ready image.

### 3.3.3. *Calibration Catalog*

The `Calibration` catalog is the reference catalog that was used to perform astrometric and photometric [calibration](#). It is a whole-sky catalog built specifically for [LSST](#), as no single prior reference catalog had both the depth and coverage needed to calibrate [LSST](#) data. It combines data from multiple previous reference catalogs and contains only stellar sources. Full details on how the `Calibration` catalog was built are provided in [P. S.](#)

1214 Ferguson et al. (2025)<sup>96</sup>. We provide a brief summary  
1215 here.

1216 For the *grizy* bands, the input catalogs were (in order  
1217 of decreasing priority): Dark Energy Survey (DES)  
1218 Y6 Calibration Stars (E. S. Rykoff et al. 2023); Gaia-  
1219 B or R Photometry (Gaia) (XP) Synthetic Magnitudes  
1220 (Gaia Collaboration et al. 2023a); the Panoramic Survey  
1221 Telescope and Rapid Response System (Pan-STARRS)1  
1222 3PI Survey (K. C. Chambers et al. 2016); Data Release  
1223 2 of the SkyMapper survey (C. A. Onken et al. 2019);  
1224 and Data Release 4 of the VLT Survey Telescope (VST)  
1225 Asteroid Terrestrial-impact Last Alert System (ATLAS)  
1226 survey (T. Shanks et al. 2015). For the *u*-band, the input  
1227 catalogs were (in order of decreasing priority): Standard  
1228 Stars from Sloan Digital Sky Survey (SDSS) Data Re-  
1229 lease 16 (R. Ahumada et al. 2020); Gaia-XP Synthetic  
1230 Magnitudes (Gaia Collaboration et al. 2023a); and syn-  
1231 thetic magnitudes generated using Single Lens Reflex  
1232 (SLR), which estimates the *u*-band flux from the *g*-band  
1233 flux and *g-r* colors. This SLR estimates were used to  
1234 boost the number of *u*-band reference sources, as other-  
1235 wise the source density from the *u*-band input catalogs  
1236 is too low to be useful for the LSST.

1237 Only stellar sources were selected from each input cat-  
1238 alog. Throughout, the Calibration catalog uses the  
1239 DES bandpasses for the *grizy* bands and the SDSS band-  
1240 pass for the *u*-band; color transformations derived from  
1241 high quality sources were used to convert fluxes from the  
1242 various input catalogs (some of which did not use the  
1243 DES/SDSS bandpasses) to the respective bandpasses.  
1244 All sources from the input catalogs are matched to Gaia-  
1245 Data Release 3 (DR3) sources for robust astrometric in-  
1246 formation, selecting only isolated sources (i.e., no neigh-  
1247 bors within 1").

1248 After collating the input catalogs and transforming  
1249 the fluxes to the standard DES/SDSS bandpasses, the  
1250 catalog was used to identify sources within a specific  
1251 region of the sky. This process generated a set of stan-  
1252 dard columns containing positional and flux informa-  
1253 tion, along with their associated uncertainties.

### 1254 3.3.4. Source and Object Designations

1255 To refer to individual sources or objects from the DP1  
1256 catalogs, one should follow the LSST DP1 naming con-  
1257 vention that has been registered with the International  
1258 Astronomical Union. Because the Source, Object, Di-  
1259 aSource, DiaObject, and SSObject tables each have  
1260 their own unique IDs, their designations should differ.

<sup>96</sup> In P. S. Ferguson et al. (2025), the calibration reference catalog is referred to as “The Monster”. This terminology is also carried over to the DP1 Butler.

1261 In general, source and object designations should be-  
1262 gin with the string “LSST-DP1” (denoting the Legacy  
1263 Survey of Space and Time, Data Preview 1), followed  
1264 by a string specifying the table from which the source  
1265 was obtained. These strings should be “O” (for the Ob-  
1266 ject table), “S” (Source), “DO” (DiaObject), “DS”  
1267 (DiaSource), or “SSO” (SSObject). Following the table  
1268 identifier, the designation should contain the full unique  
1269 numeric identifier from the specified table (i.e., the ob-  
1270 jectId, sourceId, diaObjectId, diaSourceId, or ssObject-  
1271 Id). Each component of the identifier should be sep-  
1272 arated by dashes, resulting in a designation such as  
1273 “LSST-DP1-TAB-123456789012345678”. In summary,  
1274 source designations should adhere to the formats listed  
1275 below:

- 1276 • Object: LSST-DP1-O-609788942606161356 (for  
1277 objectId 609788942606161356)
- 1278 • Source: LSST-DP1-S-600408134082103129 (for  
1279 sourceId 600408134082103129)
- 1280 • DiaObject: LSST-DP1-DO-609788942606140532  
1281 (for diaObjectId 609788942606140532)
- 1282 • DiaSource: LSST-DP1-DS-600359758253260853  
1283 (for diaSourceId 600359758253260853)
- 1284 • SSObject: LSST-DP1-SSO-21163611375481943  
1285 (for ssObjectId 21163611375481943)

1286 Tables that were not explicitly mentioned in the de-  
1287 scription above do not have their own unique IDs, but  
1288 are instead linked to one of the five tables listed above  
1289 via a unique ID. For example, the ForcedSource table  
1290 uses objectId, ForcedSourceOnDiaObject uses diaOb-  
1291 jectId, SSSource uses diaSourceId and ssObjectId, and  
1292 MPCORB uses ssObjectId.

## 1293 3.4. Maps

1294 Maps are two-dimensional visualizations of survey  
1295 data. In DP1, these fall into two categories: Sur-  
1296 vey Property Maps and Hierarchical Progressive Survey  
1297 (HiPS) Maps (P. Fernique et al. 2015).

### 1298 3.4.1. Survey Property Maps

1299 Survey Property Maps (NSF-DOE Vera C. Rubin Ob-  
1300 servatory 2025o) summarize how properties such as ob-  
1301 serving conditions or exposure time vary across the ob-  
1302 served sky. Each map provides the spatial distribution  
1303 of a specific quantity at a defined sky position for each  
1304 band by aggregating information from the images used  
1305 to make the deep\_coadd. Maps are initially created per-  
1306 tract and then combined to produce a final consolidated

map. At each sky location, represented by a spatial pixel in the Hierarchical Equal-Area iso-Latitude Pixelisation (HEALPix)(K. M. Górski et al. 2005) grid, values are derived using statistical operations, such as minimum, maximum, mean, weighted mean, or sum, depending on the property.

DP1 contains 14 survey property maps. The available maps describe total exposure times, observation epochs (one each for the earliest, mean, and latest observation epoch), PSF size and shape (one for each of the  $e^1$  and  $e^2$  shape parameters; see §5.2), PSF magnitude limits, sky background and noise levels, as well as astrometric shifts (one each for right ascension and declination) and PSF distortions (one for each of the  $e^1$  and  $e^2$  shape parameters) due to wavelength-dependent atmospheric Differential Chromatic Refraction (DCR) effects. They all use the dataset type format `deep_coadd_<PROPERTY>_consolidated_map_<STATISTIC>`. For example, `deep_coadd_exposure_time_consolidated_map_sum` provides a spatial map of the total exposure time accumulated per sky position in units of seconds. All maps are stored in HealSparse<sup>97</sup> format. Survey property maps are only available via the Data Butler (§6.2.2).

Figure 10 presents three survey property maps for exposure time, PSF magnitude limit, and sky noise, computed for representative tracts and bands. Because full consolidated maps cover widely separated tracts, we use clipped per-tract views here to make the spatial patterns more discernible.

### 3.4.2. HiPS Maps

HiPS Maps (P. Fernique et al. 2015), offer an interactive way to explore seamless, multi-band tiles of the sky regions covered by DP1, allowing for smooth panning and zooming. DP1 provides multi-band HiPS images created by combining data from individual bands of `deep_coadd` and `template_coadd` images, using an improved version (Lust et al. in prep) of the algorithm presented in R. Lupton et al. (2004). These images are false-color representations generated using various filter combinations for the red, green, and blue channels.

The available filter combinations include `gri`, `izy`, `riz`, and `ugr` for both `deep_coadd` and `template_coadd`. Additionally, for `deep_coadd` only, we provide color blends such as `uug` and `grz`. Post-DP1, we plan to also provide single-band HiPS images for all `ugrizy` bands in both Portable Network Graphics (PNG) and FITS formats.

HiPS maps are only accessible through the HiPS viewer in the RSP Portal (§6.3) and cannot be accessed via the Data Butler (§6.2.2). All multi-band HiPS images are provided in PNG format.

## 3.5. Metadata

DP1 also includes metadata about the observations, which are stored in the `Visit` table. We distinguish it from a catalog as the data it contains was produced by the observatory directly, rather than the science pipelines. The `Visit` table contains technical data for each visit, such as telescope pointing, camera rotation, airmass, exposure start and end time, and total exposure time. Some of the information contained within the `Visit` table is also contained in the `CCDVisit` catalogue described in §3.2 (e.g., exposure time), although the latter also includes information produced by the processing pipelines at a per-detector level, such as the PSF size and limiting magnitudes of a given `visit_image`.

## 3.6. Ancillary Data Products

DP1 also includes several ancillary data products. While we do not expect most users to need these, we describe them here for completeness. All the Data Products described in this section can only be accessed via the Data Butler (§6.2.2).

### 3.6.1. Standard Bandpasses

Figure 3 shows the full-system throughput of the six LSSTComCam filters. The corresponding transmission curves are provided as a DP1 data product. These datasets tabulate the full-system transmission of the six LSSTComCam filters as a function of wavelength and were used as a reference for the LSSTComCam DP1 photometry. The `standard_passband` dataset is keyed by band and is stored in Astropy Table format.

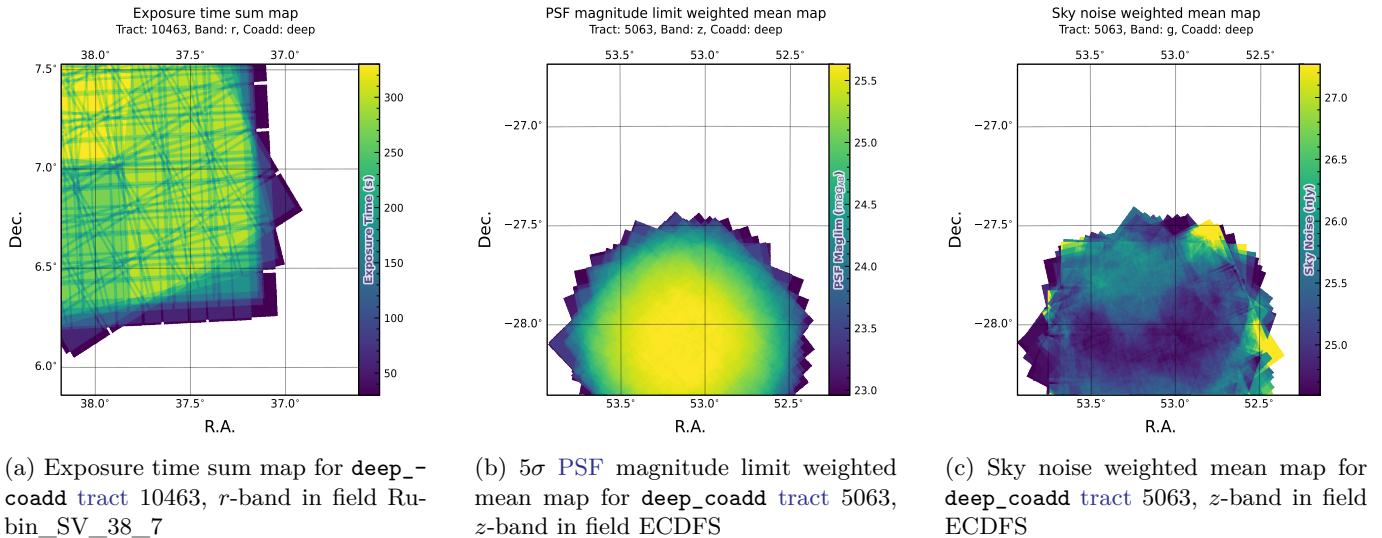
### 3.6.2. Task configuration, log, and metadata

DP1 includes provenance-related data products such as task logs, `configuration` files, and task metadata. Configuration files record the parameters used in each processing task, while logs and `metadata` contain information output during processing. These products help users understand the processing setup and investigate potential processing failures.

### 3.6.3. Calibration Data Products

Calibration data products include a variety of images and models that are used to characterize and correct the performance of the camera and other system components. These include bias, dark, and flat-field images,

<sup>97</sup> A sparse HEALPix representation that efficiently encodes data values on the celestial sphere. <https://healsparse.readthedocs.io>



(a) Exposure time sum map for `deep_coadd tract 10463`, `r`-band in field `Rubin_SV_38_7`

(b)  $5\sigma$  PSF magnitude limit weighted mean map for `deep_coadd tract 5063`, `z`-band in field ECDFS

(c) Sky noise weighted mean map for `deep_coadd tract 5063`, `g`-band in field ECDFS

**Figure 10.** Examples of survey property maps from Rubin DP1 across different bands, clipped to the boundary of a single tract for visual clarity.

1401 Photon Transfer Curve (PTC) gains, brighter-fatter kernels (P. Antilogus et al. 2014), charge transfer inefficiency (CTI) models, linearizers, and illumination corrections. For flat-field corrections, DP1 processing used combined flats, which are averaged from multiple individual flat-field exposures to provide a stable calibration. These calibration products are essential inputs to Instrument Signal Removal (ISR) (§4.2.1). While these products are included in DP1 for transparency and completeness, users should not need to rerun ISR for their science and are advised to start with the processed `visit_image`.

#### 1413 4. DATA RELEASE PROCESSING

1414 Data Release Processing (DRP) is the systematic processing of all Rubin Observatory data collected up to a certain date to produce the calibrated images, catalogs of detections, and derived data products described in Section 3. DP1 was processed entirely at the United States Data Facility (USDF) at SLAC using 17,024 CPU hours.<sup>98</sup>

1421 This section describes the pipeline algorithms used to produce DP1 and how they differ from those planned for full-scale LSST data releases. Data Release Production consists of four major stages: (1) single-frame processing, (2) calibration, (3) coaddition, and (4) difference image analysis (DIA).

<sup>98</sup> For future Data Releases, data processing will be distributed across the USDF, the French (FrDF) and UK (UKDF) data facilities.

#### 1427 4.1. LSST Science Pipelines Software

1428 The LSST Science Pipelines software (Rubin Observa-  
1429 tory Science Pipelines Developers 2025; J. D. Swinbank  
1430 et al. 2020) will be used to generate all Rubin Obser-  
1431 vatory and LSST data products. They provide both  
1432 the algorithm and middleware frameworks necessary to  
1433 process raw data into science-ready data products, en-  
1434 abling analysis by the Rubin scientific community. Ver-  
1435 sion v29.1 of the pipelines was used to produce DP1<sup>99</sup>.

#### 1436 4.2. Single Frame Processing

##### 1437 4.2.1. Instrument Signature Removal

1438 The first step in processing LSSTComCam images is  
1439 to correct for the effects introduced by the telescope and  
1440 detector. Each sensor and its readout amplifiers can  
1441 vary slightly in performance, causing images of even a  
1442 uniformly illuminated focal plane to exhibit discontinu-  
1443 ities and shifts due to detector effects. The ISR pipeline  
1444 aims to recover the original astrophysical signal as best  
1445 as possible and produce science-ready single-epoch im-  
1446 ages for source detection and measurement. A detailed  
1447 description of the ISR procedures can be found in P. Fa-  
1448 greglius & E. S. Rykoff (2025) and A. A. Plazas Malagón  
1449 et al. (2025). Figure 11 illustrates the model of detector  
1450 components and readout electronics and their impact  
1451 on the signal, tracing the process from photons incident  
1452 on the detector surface to the final quantized values<sup>100</sup>  
1453 recorded in the image files. The ISR pipeline essen-

<sup>99</sup> Documentation for this version is available at [https://pipelines.lsst.io/v/v29\\_1\\_1](https://pipelines.lsst.io/v/v29_1_1)

<sup>100</sup> The images written to disk by the camera have values that are integers that come from the ADC converting an analog voltage.

1454 tially “works backward” through the signal chain, cor-  
 1455 recting the integer analog-to-digital units (ADU) raw  
 1456 camera output back to a floating-point number of pho-  
 1457 toelectrons created in the silicon. The physical detec-  
 1458 tor, represented on the left in Figure 11, is the source  
 1459 of effects that arise from the silicon itself, such as the  
 1460 dark current and the brighter-fatter effect (A. A. Plazas  
 1461 et al. 2018; A. Broughton et al. 2024). After the inte-  
 1462 gration time has elapsed, the charge is shifted to the  
 1463 serial register and read out, which can introduce charge  
 1464 transfer inefficiencies and a clock-injected offset level.  
 1465 The signals for all amplifiers are transferred via cables  
 1466 to the Readout Electronics Board (REB), during which  
 1467 crosstalk between the amplifiers may occur. The Ana-  
 1468 log Signal Processing Integrated Circuit (ASPIC) on the  
 1469 REB converts the analog signal from the detector into a  
 1470 digital signal, adding both quantization and a bias level  
 1471 to the image. Although the signal chain is designed to  
 1472 be stable and linear, the presence of numerous sources  
 1473 of non-linearity indicates otherwise.

1474 The ISR processing pipeline for DP1 performs, in  
 1475 the following order: Analogue-to-Digital Unit (ADU)  
 1476 dithering to reduce quantization effects, serial over-  
 1477 scan subtraction, saturation masking, gain normaliza-  
 1478 tion, crosstalk correction, parallel overscan subtraction,  
 1479 linearity correction, serial CTI correction, image assem-  
 1480 bly, bias subtraction, dark subtraction, brighter-fatter  
 1481 correction, defect masking and interpolation, variance  
 1482 plane construction, flat fielding, and amplifier offset  
 1483 (amp-offset) correction<sup>101</sup>. Flat fielding for DP1 was  
 1484 performed using combined flats produced from twilight  
 1485 flats acquired with sufficient rotational dithering to mit-  
 1486 igate artifacts from print-through stars, as described in  
 1487 §2.3.

<sup>101</sup> Amp-offset corrections are designed to address systematic dis-  
 continuities in background sky levels across amplifier bound-  
 aries. The implementation in the LSST Science Pipelines is  
 based on the Pan-STARRS Pattern Continuity algorithm (C. Z.  
 Waters et al. 2020).

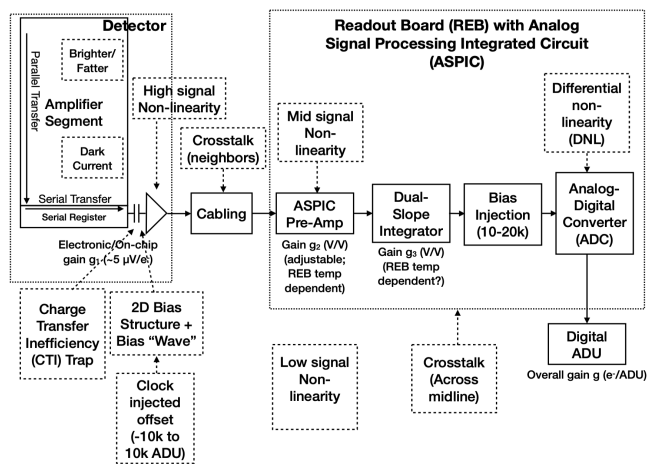


Figure 11. The model of the detector and REB components, labeled with the effects that they impart on signal.

#### 4.2.2. Background Subtraction

The background subtraction algorithms in the LSST Science Pipelines estimate and remove large-scale background signals from science imaging. Such signals may include sky brightness from airglow, moonlight, scattered light instrumental effects, zodiacal light, and diffuse astrophysical emission. In so doing, true astrophysical sources are isolated to allow for accurate detection and measurement.

To generate a background model, each post-ISR image is divided into superpixels of  $128 \times 128$  pixels. Pixels with a mask flag set that indicates that they contain no useful science data or that they contain flux from a preliminary source detection are masked. The iterative  $3\sigma$  clipped mean of the remaining pixels is calculated for each superpixel, constructing a background statistics image. A sixth-order Chebyshev polynomial is fit to these values on the scale of a single detector to allow for an extrapolation back to the native pixel resolution of the post-ISR image.

#### 4.3. Calibration

Stars are detected in each post-ISR image using a  $5\sigma$  threshold. Detections of the same star across multiple images are then associated to identify a consistent set of isolated stars with repeated observations suitable for use in PSF modeling, photometric calibration, and astrometric calibration.

Initial astrometric and photometric solutions are derived using only the calibration reference catalogs (see §3.2), and an initial PSF model is fit using PSFEx (E. Bertin 2011). These preliminary solutions provide approximate source positions, fluxes, and PSF shapes that serve as essential inputs to the calibration process, en-

1521 abling reliable source matching, selection of high-quality  
 1522 stars, and iterative refinement of the final astrometric,  
 1523 photometric, and PSF models. These preliminary solu-  
 1524 tions are subsequently replaced by more accurate fits, as  
 1525 described in the following sections.

#### 1526 4.3.1. PSF Modeling

1527 PSF modeling in DP1 uses the Piff (M. Jarvis et al.  
 1528 2021) package. Our configuration of Piff utilizes its `Pix-`  
 1529 `elGrid` model with a fourth-order polynomial interpola-  
 1530 tion per CCD, except in the  $u$ -band, where star counts  
 1531 are insufficient to support a fourth-order fit. In this  
 1532 case, a second-order polynomial is used instead. Details  
 1533 on the choice of polynomial order, overall PSF modeling  
 1534 performance, and known issues are discussed in §5.2.

#### 1535 4.3.2. Astrometric Calibration

1536 Starting from the astrometric solution calculated in  
 1537 single frame processing (§4.2), the final astrometric so-  
 1538 lution is computed using the ensemble of visits in a given  
 1539 band that overlap a given tract. This allows the astro-  
 1540 metric solution to be further refined by using all of the  
 1541 isolated point sources of sufficient signal-to-noise ratio  
 1542 in an image, rather than only those that appear in the  
 1543 reference catalog, as is done in single frame processing.  
 1544 Using multiple whole visits rather than a single detector  
 1545 also allows us to account for effects that impact the full  
 1546 focal plane, and for the proper motion and parallax of  
 1547 the sources.

1548 In order to perform the fit of the astrometric solu-  
 1549 tion, isolated point sources are associated between over-  
 1550 lapping visits and with the Gaia DR3 (Gaia Collabora-  
 1551 tion et al. 2023b) reference catalog where possible. The  
 1552 model used for DP1 consists of a static map from pixel  
 1553 space to an intermediate frame (the per-detector model),  
 1554 followed by a per-visit map from the intermediate frame  
 1555 to the plane tangent to the telescope boresight (the per-  
 1556 visit model), then finally a deterministic mapping from  
 1557 the tangent plane to the sky. The fit is done using the  
 1558 `gbdes` package (G. M. Bernstein et al. 2017), and a full  
 1559 description is given in C. Saunders (2024).

1560 The per-detector model is intended to capture quasi-  
 1561 static characteristics of the telescope and camera. Dur-  
 1562 ing Rubin Operations, the astrometric solution will al-  
 1563 low for separate epochs with different per-detector mod-  
 1564 els, to account for changes in the camera due to warm-  
 1565 ing and cooling and other discrete events. However, for  
 1566 DP1, LSSTComCam was assumed to be stable enough  
 1567 that all visits use the same per-detector model. The  
 1568 model itself is a separate two-dimensional polynomial for  
 1569 each detector. For DP1, a degree 4 polynomial was used;  
 1570 the degree of the polynomial mapping is tuned for each

1571 instrument and may be different for LSSTCam. Fur-  
 1572 ther improvements may be made by including a pixel-  
 1573 based astrometric offset mapping, which would be fit  
 1574 from the ensemble of astrometric residuals, but this is  
 1575 not included in the DP1 processing.

1576 The per-visit model attempts to account for the path  
 1577 of a photon from both atmospheric sources and those  
 1578 dependent on the telescope orientation. This model is  
 1579 also a polynomial mapping, in this case a degree 6 two-  
 1580 dimensional polynomial. Correction for DCR (§5.4) was  
 1581 not done for DP1, but will be included in LSSTCam  
 1582 processing during Rubin Operations. Future processing will  
 1583 also likely include a Gaussian Process fit to better ac-  
 1584 count for atmospheric turbulence, as was demonstrated  
 1585 by W. F. Fortino et al. (2021) and P. F. Léget et al.  
 1586 (2021).

1587 The final component of the astrometric calibration  
 1588 involves the positions of the isolated point sources in-  
 1589 cluded in the fit, which are described by five parameters:  
 1590 sky coordinates, proper motion, and parallax. While  
 1591 proper motions and parallaxes are not released for DP1,  
 1592 they are fitted for these sources in the astrometric solu-  
 1593 tion to improve the astrometric calibration.

#### 1594 4.3.3. Photometric Calibration

1595 Photometric calibration of the DP1 dataset is based  
 1596 on the Forward Global Calibration Method (FGCM)  
 1597 (D. L. Burke et al. 2018), adapted for the LSST Sci-  
 1598 ence Pipelines (H. Aihara et al. 2022; P. Fagelius &  
 1599 E. S. Rykoff 2025). We used the FGCM to calibrate  
 1600 the full DP1 dataset with a forward model that uses a  
 1601 parameterized model of the atmosphere as a function of  
 1602 airmass along with a model of the instrument through-  
 1603 put as a function of wavelength. The FGCM process  
 1604 typically begins with measurements of the instrumental  
 1605 throughput, including the mirrors, filters, and detectors.  
 1606 However, because full scans of the LSSTComCam as-  
 1607 built filters and individual detectors were not available,  
 1608 we instead used the nominal reference throughputs for  
 1609 the Simonyi Survey Telescope and LSSTCam.<sup>102</sup> These  
 1610 nominal throughputs were sufficient for the DP1 cali-  
 1611 bration, given the small and homogeneous focal plane  
 1612 consisting of only nine ITL detectors. The FGCM atmo-  
 1613 sphere model, provided by MODTRAN (A. Berk et al.  
 1614 1999), was used to generate a look-up table for atmo-  
 1615 spheric throughput as a function of zenith distance at  
 1616 Cerro Pachón. This model accounts for absorption and  
 1617 scattering by molecular constituents of the atmosphere,  
 1618 including  $O_2$  and  $O_3$ ; absorption by water vapor; and  
 1619 Mie scattering by airborne aerosol particulates. Nightly

<sup>102</sup> Available at: <https://github.com/lstt/throughputs/tree/1.9>

variations in the atmosphere are modeled by minimizing the variance in repeated observations of stars with a Signal to Noise Ratio (SNR) greater than 10, measured using “compensated aperture fluxes”. These fluxes include a local background subtraction (see §4.2.2) to mitigate the impact of background offsets. The model fitting process incorporates all six bands (*ugrizy*) but does not include any gray (achromatic) terms, except for a linear assumption of mirror reflectance degradation, which is minimal over the short duration of the DP1 observation campaign. As an additional constraint on the fit, we use a subset of stars from the reference catalog (P. S. Ferguson et al. 2025), primarily to constrain the system’s overall throughput and establish the “absolute” calibration.

Photometric transformation relations between LSST-Cam and LSSTComCam systems and other photometric systems are under development and are provided in (M. N. Porter et al. 2026)

#### 4.4. Visit Images and Source Catalogs

With the final PSF models, WCS solutions, and photometric calibrations in place, we reprocess each single-epoch image to produce a final set of calibrated visit images and source catalogs. Source detection is performed down to a  $5\sigma$  threshold using the updated PSF models, followed by measurement of PSF and aperture fluxes. These catalogs represent the best single-epoch source characterization, but they are not intended for constructing light curves. For time-domain analysis, we recommend using the forced photometry tables described in §4.6.2.

### 4.5. Coaddition Processing

#### 4.5.1. Coaddition

Only exposures with a seeing better than 1.7 arcseconds FWHM are included in the deep coadded images. For the template coadds, typically only the top third of visits with the best seeing are used (although see §3.1 for more details), resulting in an even tighter image quality cutoff for the template coadds. Exposures with poor PSF model quality, identified using internal diagnostics, are excluded to prevent contamination of the coadds with unreliable PSF estimates. The remaining exposures are combined using an inverse-variance weighted mean stacking algorithm.

To mitigate transient artifacts before coaddition, we apply the artifact rejection procedure described in Y. Al-Sayyad (2018) that identifies and masks features such as satellite trails, optical ghosts, and cosmic rays. It operates on a time series of PSF-matched images resampled onto a common pixel grid (“warps”) and leverages their

temporal behavior to distinguish persistent astrophysical sources from transient artifacts.

Artifact rejection uses both direct (where no PSF-matching is performed) and PSF-matched warps, homogenized to a standard PSF of 1.8 arcseconds FWHM, broadly consistent with the 1.7 arcsecond FWHM seeing threshold used in data screening. A sigma-clipped mean of the PSF-matched warps serves as a static sky model, against which individual warps are differenced to identify significant positive and negative residuals. Candidate artifact regions are classified as transient if they appear in less than a small percentage of the total number of exposures, with the threshold based on the number of visits,  $N$ , as follows:

- $N = 1$  or  $2$ : threshold = 0 (no clipping).
- $N = 3$  or  $4$ : threshold = 1.
- $N = 5$ : threshold = 2.
- $N > 5$ : threshold =  $2 + 0.03N$ .

Identified transient regions are masked before coaddition, improving image quality and reducing contamination in derived catalogs.

#### 4.5.2. Detection, Deblending and Measurement

After constructing coadded images, sources are detected in each band, merged across bands, deblended, and measured to generate the final object catalogs (§3.2). For each coadd in all six bands, we perform source detection at a  $5\sigma$  detection threshold and then adjust the background with a per-patch constant (coadds are built from background-subtracted images, but the deeper detection on coadds redefines what is considered source versus background). Detections across bands are merged in a fixed priority order, *irzygu*, to form a union detection catalog, which serves as input to deblending.

Deblending is performed using the Scarlet Lite algorithm, which implements the same model as Scarlet (P. Melchior et al. 2018), but operates on a single pixel grid. This allows the use of analytic gradients, resulting in greater computational speed and memory efficiency.

Object measurement is then performed on the deblended detection footprints in each band. Measurements are conducted in three modes: independent per-band measurements, forced measurements in each band, and multiband measurements.

Most measurement algorithms operate through a single-band plugin system, largely as originally described in J. Bosch et al. (2018). The same plugins are run separately for each object on a deblended image,

1718 which uses the Scarlet model as a template to re-weight  
 1719 the original noisy coadded pixel values. This effectively  
 1720 preserves the original image in regions where objects are  
 1721 not blended, while dampening the noise elsewhere.

1722 A reference band is chosen for each object based on de-  
 1723 tection significance and measurement quality using the  
 1724 same priority order as detection merging (*irzygu*) and  
 1725 a second round of measurements is performed in forced  
 1726 mode using the shape and position from the reference  
 1727 band to ensure consistent colors (J. Bosch et al. 2018).

1728 Measurement algorithm outputs include object fluxes,  
 1729 centroids, and higher-order moments thereof like sizes  
 1730 and shapes. A variety of flux measurements are pro-  
 1731 vided, from aperture fluxes and forward modeling algo-  
 1732 rithms.

1733 Composite model (CModel) magnitudes (K. Abaza-  
 1734 jian et al. 2004; J. Bosch et al. 2018) are used to cal-  
 1735 culate the extendedness parameter, which functions as  
 1736 a star-galaxy classifier. Extendedness is a binary clas-  
 1737 sifier that is set to 1 if the PSF model flux is less than  
 1738 98.5% of the (free, not forced) CModel flux in a given  
 1739 band. Additionally, the extendedness in the reference  
 1740 band is provided as a separate column for convenience  
 1741 as a multiband star-galaxy classification, and is recom-  
 1742 mended generally but also specifically for objects with  
 1743 low signal-to-noise ratio in some bands.

1744 Gaussian-Aperture-and-PSF (Gaussian Aperture and  
 1745 PSF (GAaP) K. Kuijken 2008; A. Kannawadi 2025)  
 1746 fluxes are provided to ensure consistent galaxy colors  
 1747 across bands. Sérsic model (J. L. Sérsic 1963; J. L. Sérsic  
 1748 1968) fits are run on all available bands simultaneously  
 1749 (MultiProFit, D. S. Taranu 2025). The resulting Sérsic  
 1750 model fluxes are provided as an alternative to CModel  
 1751 and are intended to represent total galaxy fluxes. Like  
 1752 CModel, the Sérsic model is a Gaussian mixture approx-  
 1753 imation to a true Sérsic profile, convolved with a Gaus-  
 1754 sian mixture approximation to the PSF. Sérsic model  
 1755 fits also include a free centroid, with all other structural  
 1756 parameters shared across all bands. That is, the in-  
 1757 trinsic model has no color gradients, but the convolved  
 1758 model may have color gradients if the PSF parameters  
 1759 vary significantly between bands.

1760 CModel measurements use a double “shapelet” (A.  
 1761 Refregier 2003) PSF model with a single shared shape.  
 1762 The Sérsic fits are intended to use a double Gaussian  
 1763 with independent shape parameters for each component.  
 1764 Due to a pipeline misconfiguration, the Sérsic fits actu-  
 1765 ally used the shapelet PSF parameters, with the higher-  
 1766 order terms ignored (since MultiProFit does not sup-  
 1767 port shapelet PSFs). This bug is not expected to im-  
 1768 pact the galaxy fluxes significantly, since the higher-  
 1769 order shapelet PSF parameters tend to be small, and

1770 the fix will be applied in future campaigns. Either way,  
 1771 the double Gaussian PSF parameters are included for  
 1772 each object.

1773 Further details on the performance of these algorithms  
 1774 are found in §5.7.

## 1775 4.6. Variability Measurement

### 1776 4.6.1. Difference Imaging Analysis

1777 Difference Image Analysis (DIA) uses the decorrelated  
 1778 Alard & Lupton image differencing algorithm (D. J.  
 1779 Reiss & R. H. Lupton 2016). We detected both posi-  
 1780 tive and negative DIASources at  $5\sigma$  in the difference  
 1781 image. Sources with footprints containing both posi-  
 1782 tive and negative peaks due to offsets from the tem-  
 1783 plate position or blending were fit with a dipole centroid  
 1784 code, which simultaneously fits offset positive and neg-  
 1785 ative PSFs. We filter the resulting DIASource catalog  
 1786 to remove detections with pixel flags indicative of ar-  
 1787 tifacts, non-astrophysical trail lengths, or unphysically  
 1788 negative direct fluxes. Finally, we perform a simple spa-  
 1789 tial association of DIASources into DIAObjects using a  
 1790 one-arcsecond matching radius.

1791 The Machine Learning reliability model applied to  
 1792 DP1 was developed with the aim to meet the latency  
 1793 requirements for Rubin Alert Production when executed  
 1794 on CPUs. Accordingly we developed a relatively simple  
 1795 model: a Convolutional Neural Network with three con-  
 1796 volutional layers, and two fully connected layers. The  
 1797 convolutional layers have a  $5 \times 5$  kernel size, with 16, 32,  
 1798 and 64 filters, respectively. A max-pooling layer of size 2  
 1799 is applied at the end of each convolutional layer, followed  
 1800 by a dropout layer of 0.4 to reduce overfitting. The last  
 1801 fully connected layers have sizes of 32 and 1. The ReLU  
 1802 activation function is used for the convolutional layers  
 1803 and the first fully connected layer, while a sigmoid func-  
 1804 tion is used for the output layer to provide a probabilistic  
 1805 interpretation. The cutouts are generated by extracting  
 1806 postage stamps of  $51 \times 51$  pixels centered on the detected  
 1807 sources. The input data of the model consist of the tem-  
 1808 plate, science, and difference image stacked to have an  
 1809 array of shape (3, 51, 51). The model is implemented  
 1810 using PyTorch (J. Ansel et al. 2024). The Binary Cross  
 1811 Entropy loss function was used, along with the Adap-  
 1812 tive Moment Estimation (Adam) optimizer with a fixed  
 1813 learning rate of  $1 \times 10^{-4}$ , weight decay of  $3.6 \times 10^{-2}$ , and  
 1814 a batch size of 128. The final model uses the weights  
 1815 that achieved the best precision/purity for the test set.  
 1816 Training was done on the SLAC Shared Scientific Data  
 1817 Facility (S3DF) with an NVIDIA model L40S GPU.

1818 The model was initially trained using simulated data  
 1819 from the second DESC Data Challenge (DC2; (LSST  
 1820 Dark Energy Science Collaboration (LSST DESC) et al.

2021)) plus randomly located injections of PSFs to increase the number of real sources, for a total of 89,066 real sources. The same number of bogus sources were selected at random from non-injected DIASources. Once the LSSTComCam data were available, the model was fine-tuned on a subset of the data containing 183,046 sources with PSF injections. On the LSSTComCam test set, the model achieved an accuracy of 98.06%, purity of 97.87%, and completeness of 98.27%. As discussed in §5.8, the injections used to train this model version do not capture all types of astrophysical variability, so performance on the test set will not be representative for variable stars, comets, and other types of variable objects. The machine-learning reliability score, reported in the `reliability` column of the `DIASource` catalog, is a scalar value between 0 and 1 that quantifies the model’s confidence that a given detection is astrophysical.

#### 4.6.2. Light Curves

To produce light curves, we perform multi-epoch forced photometry on both the direct visit images and the difference images. For light curves we recommend the forced photometry on the difference images (`psfDiffFlux` on the `ForcedSource` Table), as it isolates the variable component of the flux and avoids contamination from static sources. In contrast, forced photometry on direct images includes flux from nearby or blended static objects, and this contamination can vary with seeing. Centroids used in the multi-epoch forced photometry stage are taken either from object positions measured on the coadds or from the `DIAObjects` (the associated `DIASources` detected on difference images).

#### 4.6.3. Solar System Processing

Solar system processing in DP1 consists of two key components: the association of observations (sources) with known solar system objects, and the discovery of previously unknown objects by linking sets of tracklets<sup>103</sup>.

The association component begins by generating expected positions for all objects in the Minor Planet Center orbit catalog, using ephemerides computed with the `Sorcha` survey simulation toolkit (Merritt et al., in press)<sup>104</sup>. To enable fast lookup of objects potentially present in an observed visit, we use the `mpsky` package (M. Juric 2025). In each image, the closest `DIASource` within 1 arcsecond of a known solar system object’s predicted position is associated to that object.

In DP1 we used a simple positional association to tag `DiaSources` that are likely observations of known asteroids. The 1 arcsecond radius is intentionally generous; we did not see evidence of mismatches at DP1 depth and volume. This radius will be tuned for future processing campaigns.

The discovery component of Solar System processing uses the `heliolinx` package<sup>105</sup>, which provides tools for asteroid identification and linking (A. Heinze et al. 2023). The repository contains code for the following tasks:

- Tracklet creation with `make_tracklets`
- Multi-night tracklet linking with an algorithm
- Linkage post processing (orbit fitting, outlier rejection, and de-duplication) with `link_purify`

The inputs to the discovery processing comprised all sources detected in difference images, regardless of whether they were tagged in the association step. These inputs were produced by an early processing of LSST-ComCam commissioning data, some of which were later rejected during DP1 processing and therefore do not appear in the final DP1 data products.

About 10% of all commissioning visits targeted the near-ecliptic field `Rubin_SV_38_7`, chosen to facilitate asteroid discovery. `Rubin_SV_38_7` produced the vast majority of asteroid discoveries in DP1, as expected, but a few were found in off-ecliptic fields as well.

Tracklet creation with `make_tracklets` used an upper limit angular velocity of 1.5 deg/day, faster than any main belt asteroid and in the range of many Near-Earth Object (NEO) discoveries. While no formal minimum angular velocity was imposed, in practice it would be unlikely to detect objects moving slower than about 0.01 deg day<sup>-1</sup>. To minimize false tracklets from fields observed multiple times per night, the minimum tracklet length was set to three detections, and a minimum on-sky motion of five arcseconds was required for a valid tracklet. To claim a discovery candidate, we required tracklets to be linked across at least three nights.

Multi-night tracklet linking is the heart of Solar system discovery, which connects (“links”) tracklets belonging to the same object over a series of nights. It employs the `HelioLinC3D` algorithm (S. Eggl et al. 2020; A. Heinze et al. 2022), a refinement of the original `HelioLinC` algorithm of M. J. Holman et al. (2018). Each processing run tested each tracklet with 324 different hypotheses spanning heliocentric distances from 1.5 to

<sup>103</sup> A tracklet is defined as two or more detections of a moving object candidate taken in close succession in a single night.

<sup>104</sup> Available at <https://github.com/dirac-institute/sorcha>

<sup>105</sup> <https://github.com/heliolinx/heliolinx>

1914 9.8 astronomical unit (au) and radial velocities span-  
 1915 ning the full range of possible bound orbits (eccentricity  
 1916 0.0 to nearly 1.0). The upper limit of 10 au was cho-  
 1917 sen because searches targeting more distant populations  
 1918 require different parameter choices. This range of dis-  
 1919 tance encompasses all main belt asteroids and Jupiter  
 1920 Trojans, as well as many comets and Mars-crossers and  
 1921 some NEOs. A dedicated search for objects at heliocen-  
 1922 tric distances out to 50 au was also conducted; no distant  
 1923 objects were detected, consistent with expectations for  
 1924 the size of the DP1 data set. Smaller heliocentric dis-  
 1925 tances were not attempted here because nearby objects  
 1926 move rapidly across the sky and hence were not likely  
 1927 to remain long enough in an LSSTComCam field to be  
 1928 discovered.

1929 Candidate linkages, defined as groups of tracklets  
 1930 whose propagated orbits cluster within a radius of  $1.33$   
 1931  $\times 10^3$  au at 1 au, are identified, then post-processed via  
 1932 `link_purify` to yield a final, non-overlapping set of  
 1933 high-confidence asteroid candidates, ranked by orbit-  
 1934 fit residuals and related metrics. While `heliolinx` can  
 1935 produce false-positive or redundant raw linkages by de-  
 1936 sign, these are filtered during post-processing by `link_`  
 1937 `purify`, which applies a Rubin-specific, more stringent  
 1938 version of the MPC validation rules<sup>106</sup>. This step both  
 1939 rejects spurious linkages and deduplicates multiple hy-  
 1940 potheses for the same object, ensuring that only the  
 1941 highest-quality, non-redundant linkages are carried for-  
 1942 ward for orbit determination and for distinguishing new  
 1943 discoveries from rediscoveries of known objects.

## 1944 5. PERFORMANCE CHARACTERIZATION AND 1945 KNOWN ISSUES

1946 In this section, we provide an assessment of the DP1  
 1947 data quality and describe known issues.

### 1948 5.1. Sensor Anomalies and ISR

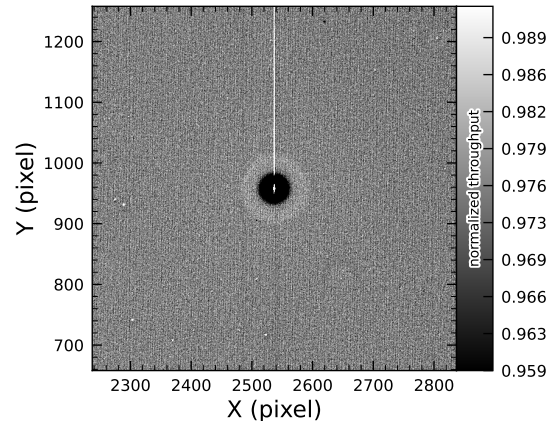
1949 In addition to the known detector features identified  
 1950 before LSSTComCam commissioning, most of which are  
 1951 handled by the ISR processing (see §4.2.1), we discov-  
 1952 ered a number of new types of anomalies in the DP1  
 1953 data. Since no corrections are currently available for  
 1954 these anomalies, they are masked and excluded from  
 1955 downstream data products.

#### 1956 5.1.1. Vampire Pixels

1957 “Vampire” pixels are visible on the images as a bright  
 1958 defect surrounded by a region of depressed flux, as  
 1959 though the defect is stealing charge from its neighboring

1960 pixels. Figure 12 shows an example of a vampire pixel  
 1961 near the center of R22\_S11 on an *r*-band flat.

1962 From studies on evenly illuminated images, vampires  
 1963 appear to conserve charge. Unfortunately, no unique  
 1964 optimum way exists to redistribute this stolen flux so,  
 1965 following visual inspection, a defect mask was created  
 1966 to exclude them from processing. We have found some  
 1967 similar features on the ITL detectors on LSSTCam, and  
 1968 will use the same approach to exclude them.



1969 **Figure 12.** A large vampire pixel near the center of R22\_-  
 1970 S11, as seen on the *r*-band flat. This clearly shows the central hot “vampire” pixels, surrounded by a region of depressed signal, with a brighter ring surrounding that caused by the local electric field effects. The charge contained in the central pixels is incompletely shifted as the image is read, and that charge leaks out into subsequent rows as they are shifted through the remnant charge. The columns that contain the hot pixels are masked as defects in all processing, as this feature cannot be otherwise corrected.

#### 1971 5.1.2. Phosphorescence

1972 Some regions of the LSSTComCam CCD raft were  
 1973 seen to contain large numbers of bright defects. An ex-  
 1974 ample is shown in Figure 13 in a *g*-band flat. On further  
 1975 investigation, it appears that on some detectors a layer  
 1976 of photoresist wax was incompletely removed from the  
 1977 detector surface during production. As this wax is now  
 1978 trapped below the surface coatings, there is no way to  
 1979 physically clean these surfaces. If this wax responded  
 1980 to all wavelengths equally, then it would likely result in  
 1981 quantum efficiency dips, which might be removable dur-  
 1982 ing flat correction. However, it appears that this wax is  
 1983 slightly phosphorescent, with a decay time on the order  
 1984 of minutes, resulting in the brightness of these defects  
 1985 being dependent on the illumination of prior exposures.  
 1986 The worst of these regions were excluded with manual  
 1988 masks.

<sup>106</sup> <https://minorplanetcenter.net/mpcops/documentation/identifications/additional/>

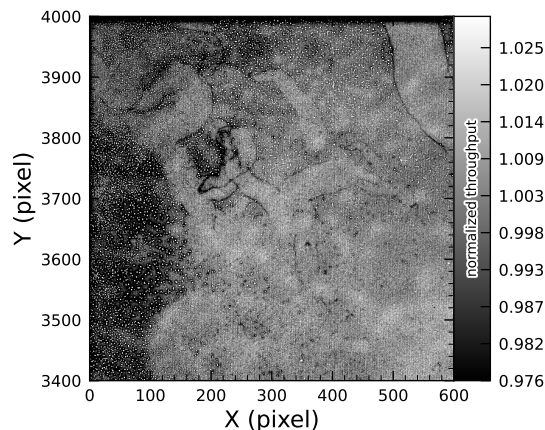


**Figure 13.** The top left corner of R22\_S01 in the g-band flat, showing the many small defect features that are caused by the remnant photoresist wax. A single large defect box masks this region from further analysis to prevent these features from contaminating measurements.

### 5.1.3. Crosstalk

Crosstalk refers to unwanted signal interference between adjacent pixels or amplifiers. We use an average inter-amp crosstalk correction based on laboratory measurements with LSSTCam. These average corrections proved satisfactory, and so have been used as-is for DP1 processing. There are, however, some residual crosstalk features present post-correction, with a tendency towards over-subtraction. Figure 14 shows an example of a bright star with over-subtracted crosstalk residuals visible on neighboring amplifiers to both sides on exposure 2024120600239, detector R22\_S02.

### 5.1.4. Bleed Trails

Bleed trails are produced when charge from saturated pixels spills into adjacent pixels. Bleed trails were anticipated on LSSTComCam sensors, but they appear in more dramatic forms than had been expected. As a bleed trail nears the serial register, it fans out into a “trumpet” shaped feature. Although bright, these features do not have consistently saturated pixels. In DP1 these “edge bleeds” were identified and masked.

Saturated sources can create a second type of bleed, where the central bleed drops below the background level. The depressed columns along these trails extend across the entire readout column of the detector, crossing the detector mid-line. We developed a model for these to identify which sources are sufficiently saturated to result in such a trail, which is then masked. As this kind of trail appears only on the ITL detectors, we’ve named these features “ITL dips”. Figure 15 shows an example of a bright star exhibiting the “ITL dip” phe-

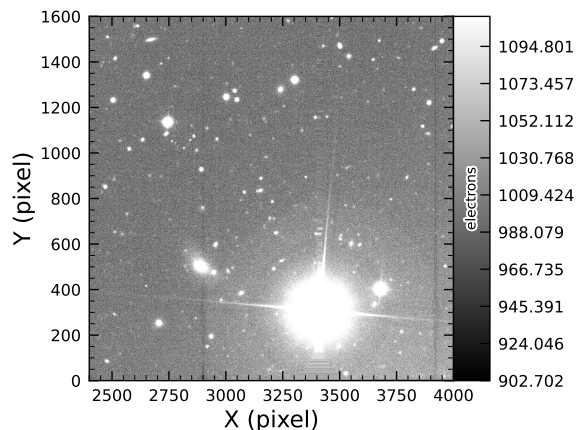


**Figure 14.** An example of a bright star with over-subtracted crosstalk residuals visible on neighboring amplifiers to both sides (exposure 2024120600239, detector R22\_S02). The horizontal banding stretching from the center of the star shows the interpolation pattern covering the saturated core and the ITL edge bleed near the serial register.

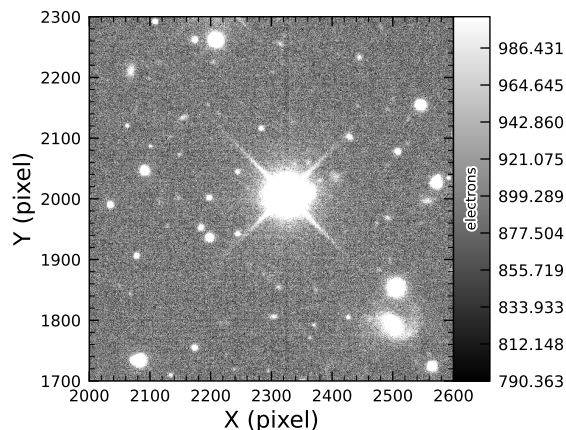


**Figure 15.** A bright star showing the “ITL dip” phenomenon, in which a dark trail extends out from the star to the top and bottom edges of the detector (exposure: 2024121000503, detector: R22\_S21).

## 5.2. PSF Models

To characterize PSF performance, we use adaptive second moments (G. M. Bernstein & M. Jarvis 2002) measured on PSF stars and on the PSF model using the HSM implementation (C. Hirata & U. Seljak 2003; R. Mandelbaum et al. 2005). All measurements are expressed in the pixel coordinate frame of each detector. We characterize the performance of the PSF using the

classical trace of the second moment matrix  $T$ , along with the ellipticity parameters  $e^1$  and  $e^2$ . Measurements on the observed PSF stars are denoted as  $T_{\text{PSF}}$ ,  $e_{\text{PSF}}^1$ ,  $e_{\text{PSF}}^2$ , while those from PSF models are denoted as  $T_{\text{model}}$ ,  $e_{\text{model}}^1$ ,  $e_{\text{model}}^2$ . We compare two PSF modeling approaches:

- Piff with second-order polynomial interpolation (Piff O2), the pipeline’s default, and
- Piff with fourth-order polynomial interpolation (Piff O4), which serves as the final DP1 PSF model.

Table 5 summarizes each model’s ability to reconstruct the mean  $T$ ,  $e^1$ , and  $e^2$  on LSSTComCam. Both models exhibit a negative residual bias in the reconstructed PSF size, with Piff O4 providing improved performance over Piff O2.

An alternative approach to evaluating the performance of the PSF model is to examine the average  $\delta T/T$ , where  $\delta T$  is  $T_{\text{PSF}} - T_{\text{model}}$ , across visits, projected onto focal-plane coordinates, as shown in Figure 16. Piff reveals strong spatial correlations in the residuals, including a systematic offset consistent with the results presented in Table 5. The presence of these spatial structures motivated the adoption of fourth-order polynomial interpolation in all bands except  $u$ -band. Although not shown in Figure 16, residual patterns persist even with third-order interpolation, indicating that it is insufficient to capture the complexity of the PSF variation. Increasing the interpolation order to five would nominally reduce the residuals further, but the limited number of stars available on some CCDs would not provide adequate constraints for such a model, while the resulting improvement would likely be minimal. Preliminary analysis of LSSTCam data in the laboratory at SLAC National Accelerator Laboratory (SLAC) shows that the ITL sensors exhibit the same pattern as ITL sensors on LSSTComCam.

Another way to look at the PSF modeling quality is via whisker plots of the PSF second and fourth moments and their modeling residuals projected on a part of the sky. In addition to the second moment, the spin-2 fourth moments,  $e^{(4)}$ , are defined as:

$$e_1^{(4)} = M_{40} - M_{04}$$

$$e_2^{(4)} = 2(M_{31} - M_{13}),$$

where  $M_{pq}$  are the standardized higher moments as defined in T. Zhang et al. (2023) measured on stars and PSF models. Figure 17 shows the whisker plots of  $e$ ,  $e^{(4)}$  (top rows), and  $\delta e$ ,  $\delta e^{(4)}$  in the ECDFS field. The direction of a whisker represents the orientation of the

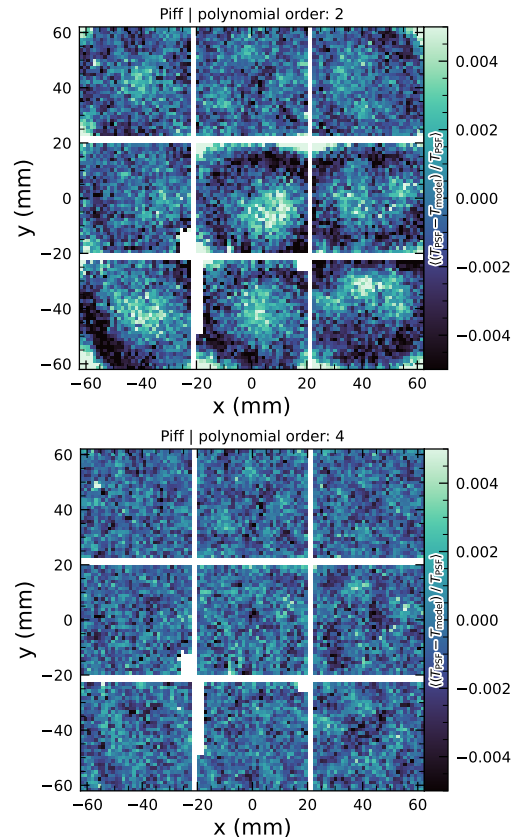


Figure 16. Average across all visits of  $\delta T/T$  for Piff O2 and Piff O4 modeling on LSSTComCam. Averages are computed using a  $120 \times 120$  binning.

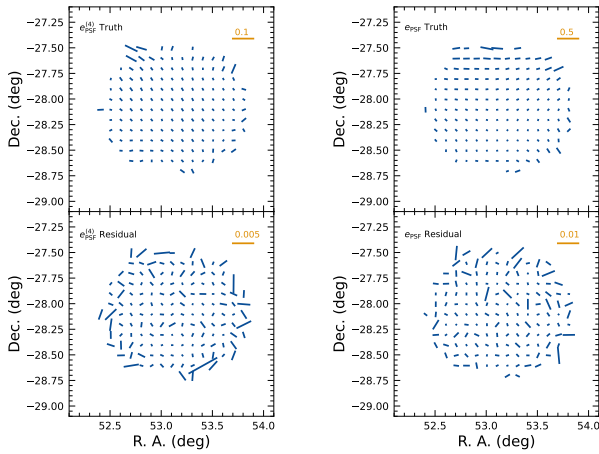
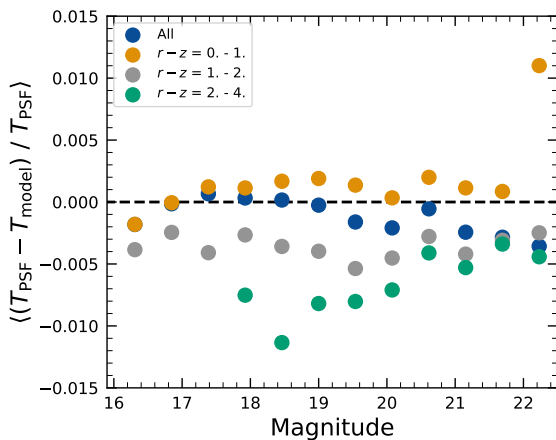
shape, while the length represents the amplitude  $|e|$  or  $|e^{(4)}|$ . We observe coherent patterns in both the PSF moments and the residuals, the latter of which warrants further investigation if it persists in future data releases.

Figure 18 shows a plot of  $\delta T/T$  versus stellar magnitude, which can reveal any dependencies between PSF size and flux. We also repeat this analysis in color bins to probe chromatic effects. Binning by color uncovers a clear color dependence, as was also seen in DES (?). The residual is consistent with Table 5 and its cause is unknown. DP1 does not include the color correction implemented in the DES Year 6 analysis, T. Schutt et al. (2025). This will be included in processing of future data releases.

As noted in Rubin Observatory Science Pipelines Developers (2025), two key Piff features were not used in the DP1 processing. PSF color dependence was not implemented, and, while Rubin software allows Piff to work with sky coordinates (including WCS transformations), it does not yet correct for sensor-induced astrometric

**Table 5.** Observed mean values and comparison of model residuals, across all visits and filters

| Quantity                                  | Observed                           | Piff O2          | Piff O4          |
|---|------------------------------------|------------------|------------------|
|   |                                    | $\times 10^{-4}$ | $\times 10^{-4}$ |
| $\langle T \rangle$ (pixel <sup>2</sup> ) | $11.366 \pm 0.003$                 |                  |                  |
| $\langle e^1 \rangle$                     | $(-6.07 \pm 0.05) \times 10^{-3}$  |                  |                  |
| $\langle e^2 \rangle$                     | $(-4.57 \pm 0.05) \times 10^{-3}$  |                  |                  |
| $\langle e \rangle$                       | $(8.794 \pm 0.004) \times 10^{-2}$ |                  |                  |
| $\langle \delta T/T \rangle$              |                                    | $-4.0 \pm 0.2$   | $-5.0 \pm 0.2$   |
| $\langle \delta e^1 \rangle$              |                                    | $0.6 \pm 0.1$    | $0.5 \pm 0.1$    |
| $\langle \delta e^2 \rangle$              |                                    | $0.0 \pm 0.1$    | $0.0 \pm 0.1$    |

**Figure 17.** Whisker plots for the ECDFS field for  $e$ ,  $e^{(4)}$  and  $\delta e$ ,  $\delta e^{(4)}$ .**Figure 18.** Binned  $\delta T/T$  as a function of magnitude across all visits and filters and in bins of stellar colors.

2106 distortions such as tree rings (H. Y. Park et al. 2017).  
 2107 Both features are planned for upcoming releases.

### 5.3. Astrometry

2108

2109 To characterize astrometric performance, we evaluate  
 2110 both internal consistency and agreement with an external  
 2111 reference. The primary measure of internal consistency  
 2112 is the repeatability of position measurements for  
 2113 the same object, defined as the RMS of the astrometric  
 2114 distance distribution for stellar pairs having a specified  
 2115 separation in arcminutes. We associate isolated point  
 2116 sources across visits and compute the rms of their fitted  
 2117 positions, rejecting any stars with another star within  
 2118  $2''$ . Figure 19 shows the mean per-tract rms astrometric  
 2119 error in RA for all isolated point sources, both after the  
 2120 initial calibration and after the final calibration, which  
 2121 includes proper motion corrections. The results indicate  
 2122 that the astrometric solution is already very good after  
 2123 the initial calibration. Global calibration yields only  
 2124 modest improvement, likely due to the short time span  
 2125 of DP1 and the minimal distortions in the LSSTCom-  
 2126 Cam. In the main survey, the longer time baseline and  
 2127 greater distortions near the LSSTCam field edges will  
 2128 make global calibration more impactful. An additional  
 2129 measure of internal consistency is the repeatability of  
 2130 separations between objects at a given distance. To com-  
 2131 pute this, we identify pairs of objects that are separated  
 2132 by a specified distance and measure their precise separa-  
 2133 tion during each visit in which both objects are ob-  
 2134 served. The scatter in these separation measurements  
 2135 provides an indication of the internal consistency of the  
 2136 astrometric model. Figure 20 shows the median separa-  
 2137 tion for pairs of objects separated by approximately 5  
 2138 arcminutes (referred to as “AM1”), computed per tract  
 2139 after the final calibration. These values are already ap-  
 2140 proaching the design requirement of 10 mas.  
 2142

2143 To assess external consistency, we consider the median  
 2144 separation between sources not included in the astro-  
 2145 metric fit and associated objects from a reference catalog  
 2146 (§3.3.3). For this, we use the Gaia DR3 catalog, with the

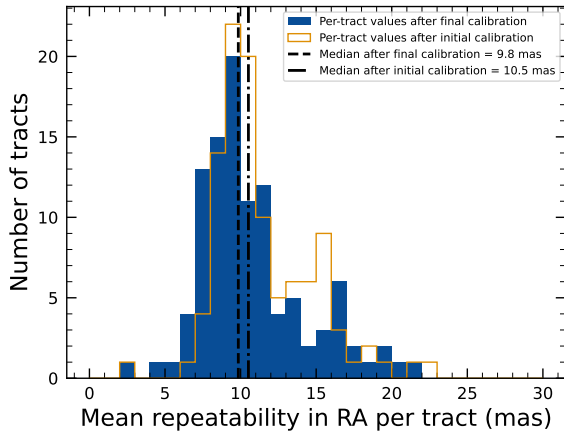


**Figure 19.** Mean per-tract astrometric repeatability of measurements of isolated point sources in RA in visits across all bands.

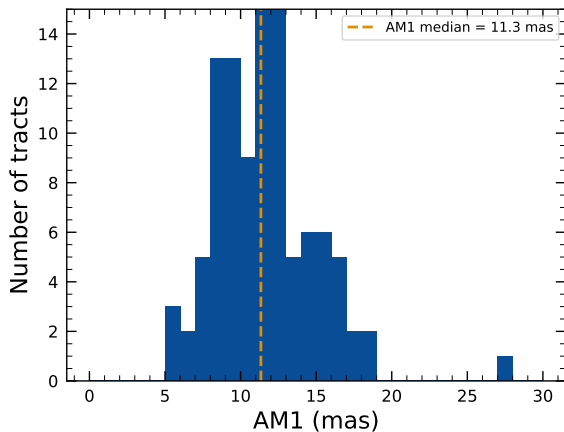


**Figure 20.** Median per-tract repeatability in separations between isolated point sources 5 arcmin apart (AM1) in visits across all bands.

2147 object positions shifted to the observation epoch using  
 2148 the Gaia proper motion parameters. Figure 21 shows the  
 2149 median separation for each visit in the  $r$ -band in `tract`  
 2150 4849 in the ECDFS fields. The calculated values are  
 2152 almost all within 5 mas, well below the design require-  
 2153 ment of 50 mas for the main survey. By examining the  
 2154 astrometric residuals, we can assess whether there are  
 2155 distortions not accounted for by the astrometric model.  
 2156 In some cases, residuals from a single visit exhibit behav-  
 2157 ior consistent with atmospheric turbulence, as shown in  
 2158 Figure 22, which is characterized by a curl-free gradient  
 2159 field in the two-point correlation function of the residu-  
 2160 als (E-mode), P. F. Léget et al. (2021) and W. F. Fortino  
 2162 et al. (2021). However, as seen in Figure 23, the residu-  
 2163 als in many visits also have correlation functions with

2164 a non-negligible divergence-free B-mode, indicating that  
 2165 some of the remaining residuals are due to unmodeled  
 2166 instrumental effects, such as rotations between visits.

2168 We can see unmodeled camera distortions by stacking  
 2169 the astrometric residuals over many visits as a function  
 2170 of the focal plane position. Figure 24 shows the median  
 2172 residuals in  $x$  and  $y$  directions for 1792 visits. Spatial  
 2173 structures are evident at the CCD level, as well as at  
 2174 the mid-line break, the discontinuity between the two  
 2175 rows of amplifiers, in the  $y$ -direction residuals. Further  
 2176 stacking all the detectors makes certain effects particu-  
 2177 larly clear. Figure 25 shows distortions very similar to  
 2178 those measured for an LSSTCam ITL sensor in a labo-  
 2180 ratory setting in J. H. Esteves et al. (2023).

#### 2181 5.4. Differential Chromatic Refraction

2182 DCR occurs when light passes through Earth’s atmo-  
 2183 sphere, refracting more for shorter wavelengths, which  
 2184 causes blue light to appear shifted closer to the zenith.  
 2185 This wavelength-dependent effect results in the smear-  
 2186 ing of point sources along the zenith direction, specifi-  
 2187 cally parallel to the parallactic angle. The DCR effect  
 2188 is observable in LSSTComCam data, particularly in the  
 2189 angular offset versus  $g - i$  band magnitude difference  
 2190 plots, as shown in Figure 26. These plots include 228  
 2191 visits selected to maximize the range of observed air-  
 2192 mass, which spans 1.01–1.30 with a mean value of 1.13.  
 2193 When looking at data perpendicular to the parallactic  
 2194 angle, sources exhibit no discernible DCR effect, which  
 2195 is expected, and form a clear vertical distribution on the  
 2196 two-dimensional density plots in Figure 26.

2197 In contrast, sources aligned with the parallactic angle  
 2198 exhibit a tilted, linear distribution, clearly demonstrat-  
 2199 ing that the relationship between angular offset and the  
 2200  $g - i$  band magnitude difference, thereby providing a vi-  
 2201 sual indication of the DCR effect. The DCR effect will  
 2202 be addressed in future releases.

#### 2203 5.5. Stellar Photometry

2204 The photometric repeatability for isolated bright un-  
 2205 resolved sources following the FGCM fits was excellent.  
 2206 For the 10% of unresolved sources withheld from the fit  
 2207 and having signal-to-noise ratios greater than 100, the  
 2208 photometric repeatability after applying chromatic cor-  
 2209 rection was 7.1, 5.4, 5.4, 5.1, 5.9, and 6.5 mmag in the  
 2210  $ugrizy$  bands respectively, across all fields. After ac-  
 2211 counting for photometric noise, the intrinsic photomet-  
 2212 ric repeatability was approximately 4.8, 2.7, 1.7, 1.0, 2.0,  
 2213 and 1.1 mmag in  $ugrizy$ . The DP1 processing does not  
 2214 yet include chromatic corrections in the final photome-  
 2215 try. In this case the delivered photometric repeatability  
 2216 was 3–8 mmag for  $grizy$ .

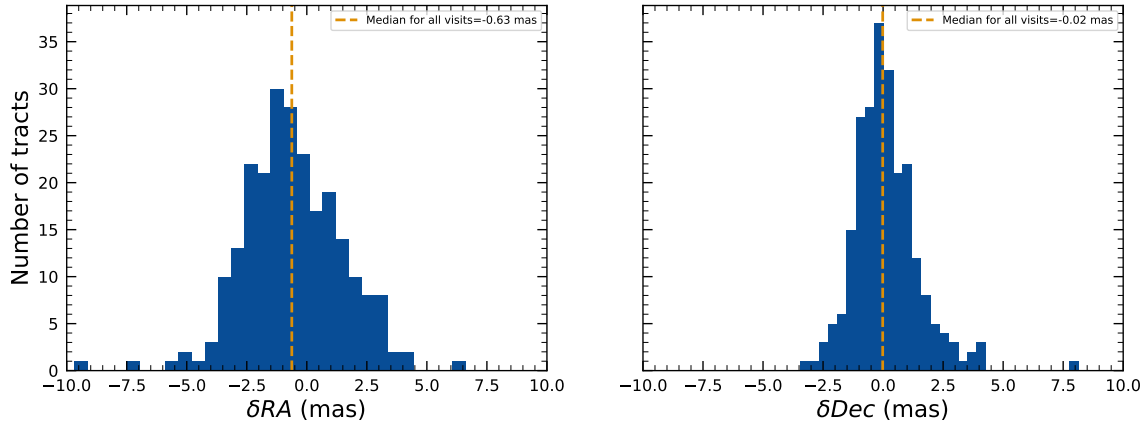


**Figure 21.** Median absolute offset for all visits in  $r$ -band in [tract 4849](#) in the ECDFS field. The offset is the difference between the positions of isolated point sources that were reserved from the astrometric fit and matched objects from the Gaia DR3 catalog.

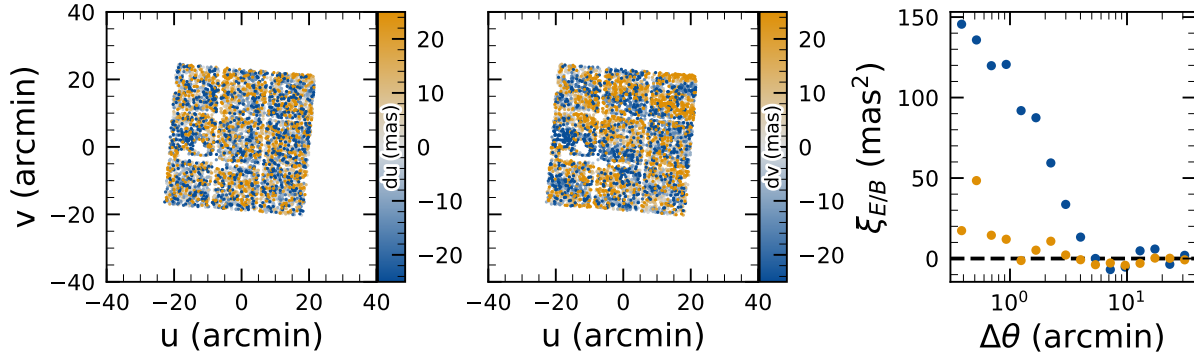


**Figure 22.** Astrometric residuals in  $u$  (left panel) and  $v$  (center panel) directions with the E (blue) and B (orange) modes of the two-point correlation function (right panel) seen in visit 2024120200359 in  $u$  band. The residuals show a wave-like pattern characteristic of atmospheric turbulence, and there is significant E-mode and negligible B-mode in the correlation function.

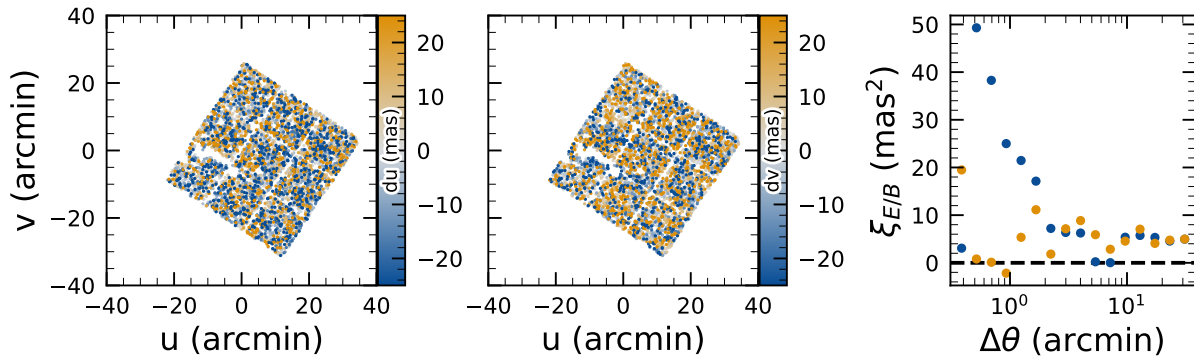


**Figure 23.** Astrometric residuals in  $u$  (left panel) and  $v$  (center panel) directions, with the E (blue) and B (orange) modes of the two-point correlation function (right panel) seen in visit 2024120700527 in  $u$  band. There are coherent residuals, but without the wave-like pattern seen in [Figure 22](#), and the correlation function has significant values for both E and B-modes.

2217 In [Figure 27](#), we show the stellar loci for  $ugriz$  for un- 2219 unresolved sources were selected using the extendedness  
2218 resolved sources in the `DP1 Object` table (§3.2). These

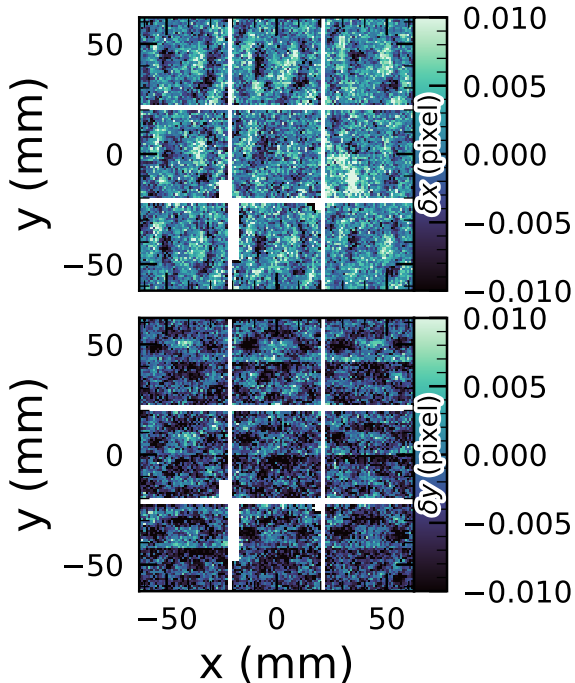


**Figure 24.** Median astrometric residuals as a function of focal plane position, shown in the left panel for the  $x$  direction and in the right panel for the  $y$  direction, for all nine LSSTComCam CCDs independently. The range of the color scale is  $\pm 0.01$  pixels, corresponding to 2 mas, showing that the effect is small.

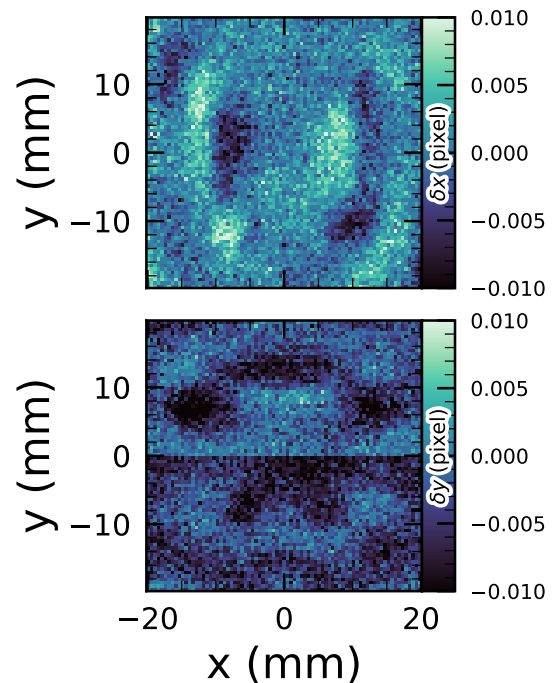


**Figure 25.** Median residuals as a function of pixel position, shown in the left panel for the  $x$  direction and in the right panel for the  $y$  direction. These residuals are aggregated across all nine CCDs that comprise the central LSSTComCam raft. The range of the color scale is  $\pm 0.01$  pixels, corresponding to 2 mas, showing that the effect is small.

parameter (§3.2) in the Object catalog. This parameter is assigned a value of 0 (unresolved) or 1 (resolved) in each band based on the difference between the PSF and CModel magnitudes. The extendedness is set to 1 when this magnitude difference exceeds 0.016 mag, as the PSF flux for extended sources is biased low relative to the CModel flux. This method has been previously employed by the SDSS pipelines, and its statistical properties, including the optimal combination of information from different bands and repeated measurements, are discussed in C. T. Slater et al. (2020).

Figure 28 illustrates the behavior of the extendedness parameter. Its behavior in the  $g$  and  $r$  bands is similar, with unresolved sources scattered around the vertical line centered on zero. The width of the distribution increases towards fainter magnitudes. Resolved sources are found to the right and the dashed lines in the top panels show the adopted “star-galaxy” separation boundary. The morphology of the two color-magnitude diagrams in the bottom panels suggest that the unresolved sample suffers from increasing contamination by galaxies for  $r > 24$ . This behavior is consistent with

simulation-based predictions from C. T. Slater et al. (2020).

### 5.6. Detection Completeness on Coadds

We characterize completeness by injecting synthetic sources into coadded images, and by comparing source detections to external catalogs. In both cases, we use a greedy, probabilistic matching algorithm that matches reference objects, in order of descending brightness, to the most likely target within a  $0''.5$  radius.

We inject sources in 12 of the patches of the ECDFS region with the deepest coverage. The input catalog contains stars and galaxies from part of the Data Challenge 2 (DC2) simulations (LSST Dark Energy Science Collaboration (LSST DESC) et al. 2021), where the galaxies consist of an exponential disk and de Vaucouleurs (G. de Vaucouleurs 1948, 1953) bulge. To avoid deblender failures from excessive increases in object density, stars with a total flux (i.e., summed across all six bands) brighter than 17.5 mag are excluded, as are galaxies whose total flux is brighter than 15 mag or fainter than 26.5 mag. Half of the remaining objects are selected for injection. Afterwards, individual bulge and disk com-

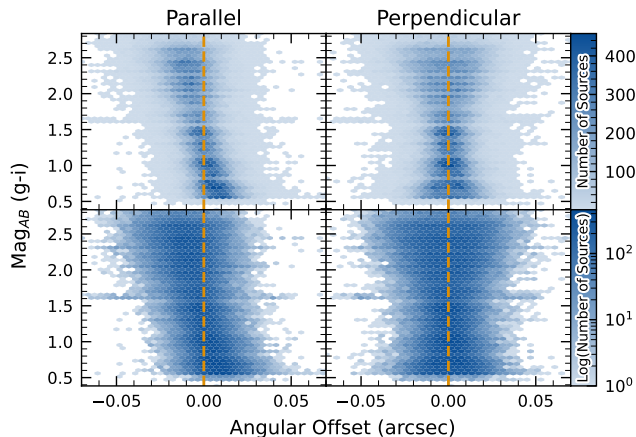


**Figure 26.** Visualization of [Differential Chromatic Refraction \(DCR\)](#) observed in the [LSSTComCam](#) commissioning campaign. The  $g - i$  color is computed for every source in the reference catalog (§3.3.3) that is matched to a direct source in the science image, and the binned density for the full survey is plotted against the angular offset between the reference and detected positions. The angular offset is projected along coordinates parallel and perpendicular to the parallactic angle of the observation, and shows a characteristic correlation along the parallel axis with no correlation along the perpendicular axis. The orange vertical dashed line indicates the expected  $g - i$  magnitude distribution at zero angular offset.

2265 ponents fainter than 29 mag are also excluded, both  
 2266 for computational expediency and because their struc-  
 2267 tural properties are less likely to be representative of  
 2268 real galaxies.

2270 [Figure 29](#) shows completeness as a function of mag-  
 2271 nitude for these injected objects in the [ECDFS](#) field.  
 2272 These completeness estimates are comparable to results  
 2273 from matching external catalogs. Matching to the Hub-  
 2274 ble Legacy Field catalog ([G. Illingworth et al. 2016](#);  
 2275 [K. E. Whitaker et al. 2019](#)) reaches 50% completeness  
 2276 at  $F775W = 26.13$ , or about  $i = 25.83$  from differences  
 2277 in matched object magnitudes. Similarly, completeness  
 2278 drops below 90% at  $VIS = 23.80$  from matching to  
 2279 [Euclid Q1](#) ([Euclid Collaboration et al. 2025](#)) objects,  
 2280 equivalent to roughly  $i = 23.5$ . The [Euclid](#) imaging is of  
 2281 comparable or shallower depth, so magnitude limits at  
 2282 lower completeness percentages than 90% are unreliable,  
 2283 whereas the [HST](#) images cover too small and irregular of  
 2284 an area to accurately characterize 80-90% completeness  
 2285 limits.

2286 At the 80% completeness limit, nearly 20% of objects,  
 2287 primarily injected galaxies, are incorrectly classified as  
 2288 stars based on their reference band extendedness. Sim-  
 2289 ilarly, the fraction of correctly classified injected stars

2290 drops to about 50% at  $i = 23.8$  (corresponding to 90%  
 2291 completeness).

2292 This analysis has several caveats. The selection of  
 2293 objects for matching in any catalog is not trivial. Some  
 2294 fraction of the detections are spurious, particularly close  
 2295 to bright stars and their diffraction spikes. Additionally,  
 2296 some objects lie in masked regions of one survey but not  
 2297 another, which has not been accounted for. For injected  
 2298 source matching, the reference catalog (§3.3.3) does not  
 2299 include real on-sky objects. Based on prior analyses of  
 2300 the [DC2](#) simulations, purity is generally greater than  
 2301 completeness at any given magnitude. Similarly, for  
 2302 bright ( $i < 23$ ) objects classified as stars by reference  
 2303 band extendedness,  $< 5\%$  are either unmatched to a [Euclid](#)  
 2304 or [HST](#) object, or misclassified - that is, selecting on  
 2305 extendedness alone yields a fairly pure but incomplete  
 2306 sample of stars. We expect to remedy some of these  
 2307 shortcomings in future releases.

### 2308 5.7. Model Flux and Shape Measurement

2309 [Figure 30](#) shows  $i$ -band magnitude residuals for  
 2310 [CModel](#) and [Sérsic](#) measurements using the matched in-  
 2311 jected galaxies described in §5.6. Similar behavior is  
 2312 seen in other bands. [Sérsic](#) fluxes show reduced scatter  
 2313 for galaxies with  $i < 22.5$ , though [CModel](#) fluxes are  
 2314 less biased, with median residuals closer to zero and less  
 2315 magnitude-dependent. For fainter objects, [Sérsic](#) fluxes  
 2316 are more biased and less accurate. The magnitude of  
 2317 this bias is considerably larger than previously seen in  
 2318 simulated data. Subsequent testing indicates that this  
 2319 bias can be (roughly) halved by fitting an exponential  
 2320 model first, and then using those parameters to initialize  
 2321 a free [Sérsic](#) fit. This approach will be adopted in future  
 2322 releases. Aperture fluxes - including [Kron](#) and [GAaP](#) -  
 2323 are not shown as they are not corrected to yield total  
 2324 fluxes. The correction for [Kron](#) fluxes can be derived  
 2325 from the [Sérsic](#) index ([A. W. Graham & S. P. Driver](#)  
 2326 [2005](#)), but this correction is not provided in object ta-  
 2327 bles.

2328 [Figure 31](#) shows  $g - i$  color residuals versus  $r$ -band  
 2329 magnitude for the same sample of galaxies as [Figure 30](#).  
 2330 For this and most other colors, [GAaP](#) (with a  $1''$  aper-  
 2331 ture) and [Sérsic](#) colors both yield lower scatter; however,  
 2332 the [CModel](#) colors have the smallest bias. Curiously,  
 2333 the [GAaP](#) bias appears to be magnitude-dependent,  
 2334 whereas the [Sérsic](#) bias remains stable from  $19 < r < 26$ .  
 2335 Any of these color measurements are suitable for use  
 2336 for deriving quantities like photometric redshifts, stellar  
 2337 population parameters, etc.

2338 In addition to photometry, some algorithms include  
 2339 measurements of structural parameters like size, ellip-  
 2340 ticity, and [Sérsic](#) index. One particular known issue is

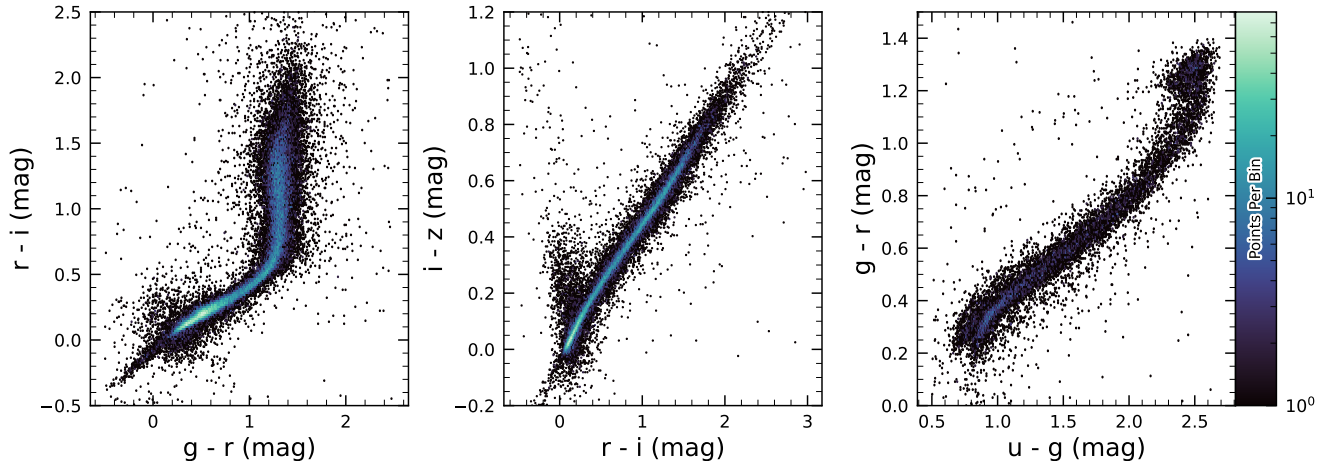


**Figure 27.** Examples of stellar loci for unresolved sources from the DP1 dataset. From left to right: *gri* stellar locus containing 63,236 stars with signal-to-noise ratio  $> 200$  in the *i* band; *riz* stellar locus containing 46,760 stars with signal-to-noise ratio  $> 200$  in the *i* band; *ugr* stellar locus containing 12,779 stars with signal-to-noise ratio  $> 50$  in the *u* band.

2341 that many (truly) faint objects have significantly over-  
 2342 estimated sizes and fluxes. This was also seen in the Dark  
 2343 Energy Survey (K. Bechtol et al. 2025), who dubbed  
 2344 such objects “super-spreaders”. These super-spreaders  
 2345 contribute significantly to overestimated fluxes at the  
 2346 faint end (see e.g. Figure 30), and are particularly prob-  
 2347 lematic for the Kron algorithm (R. G. Kron 1980), which  
 2348 should only be used with caution.

2349 As mentioned in §4.5, the Sérsic fits include a free  
 2350 centroid, which is initialized from the fiducial centroid  
 2351 of the object. Preliminary analyses of matched injected  
 2352 objects suggest that the Sérsic model galaxy *astrom-*  
 2353 *etry* residuals are somewhat smaller than for the stan-  
 2354 dard centroids used in other measurements, and so users  
 2355 of the Sérsic photometry should also use these centroid  
 2356 values. One caveat is that for faint objects and/or in  
 2357 crowded regions with unreliable deblending, free cen-  
 2358 troids can drift significantly and potentially towards  
 2359 other objects, so objects with large differences between  
 2360 the fiducial and Sérsic *astrometry* should be discarded  
 2361 or used with caution.

2362 Sérsic model parameter uncertainties are estimated  
 2363 by computing and inverting the Hessian matrix with  
 2364 the best-fit parameter values, after replacing the pixel  
 2365 data (but not uncertainties) by the best-fit model values.  
 2366 Currently, only the on-diagonal dispersion term (square  
 2367 root of the variance) is provided as an error estimate for  
 2368 each parameter. Future releases may provide more off-  
 2369 diagonal terms of the covariance matrix - particularly  
 2370 for the structural parameters, which are known to be  
 2371 correlated.

2372 A major outstanding issue is that many parameter  
 2373 uncertainties - including but not limited to those for

2374 fluxes - are underestimated. This is at least partly (but  
 2375 not wholly) due to the fact that coaddition introduces  
 2376 covariance between pixels, which is not captured in per-  
 2377 pixel variances.

2378 The degree to which uncertainties are underestimated  
 2379 can depend on the parameter in question and on the  
 2380 brightness of the object. In plots of uncertainty-scaled  
 2381 residuals, the ideal behavior is for the median (i.e. the  
 2382 bias) to lie close to zero, and for the  $\pm 1\sigma$  lines to lie at  
 2383  $\pm 1$ , without any dependence on magnitude. Figure 32  
 2384 shows that flux and color uncertainties for PSF model  
 2385 magnitudes of injected stars are both underestimated,  
 2386 but by a factor of approximately 1.7–2 that is not very  
 2387 sensitive to SNR. This holds for astrometric/centroid  
 2388 parameters as well.

2389 In turn, Figure 33 shows that CModel color uncertain-  
 2390 ties of galaxies are underestimated by a similar factor at  
 2391 the faint end, but with appreciable scaling with mag-  
 2392 nitude (and thereby SNR). Flux error underestimation  
 2393 is both larger than for colors and scales more strongly  
 2394 with SNR. This indicates that systematic effects domi-  
 2395 nate the errors in fluxes, particularly for bright galaxies.  
 2396 This is also at least partly but not wholly due to so-  
 2397 called model inadequacy - that is, the fact that galaxy  
 2398 models, parameteric or otherwise, are insufficiently com-  
 2399 plex to capture the structure of real galaxies.

2400 Figure 34 shows that Sérsic model fluxes and colors  
 2401 have similar behavior as CModel, but with a greater  
 2402 degree of overestimation. This may be partly due to the  
 2403 fact that Sérsic parameter uncertainties are estimated  
 2404 along with the free centroid and structural (shape and  
 2405 Sérsic index) parameters, whereas the forced CModel

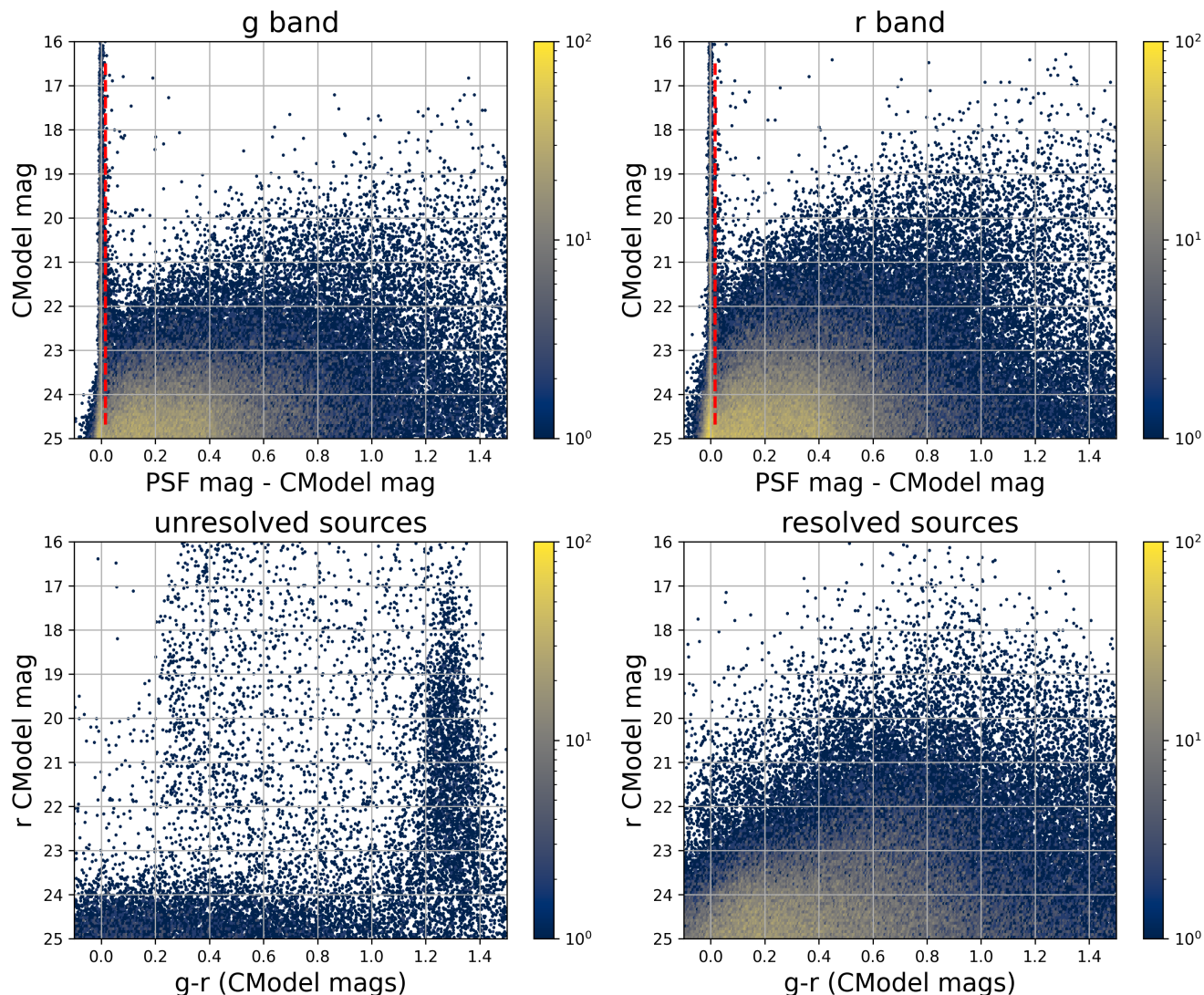


**Figure 28.** The top two panels shows the difference between the PSF and CModel magnitudes as a function of CModel magnitude in the  $g$  and  $r$  bands for 178,547 sources with  $CModel_r < 25$  from the ECDFS field. The vertical dashed line in each panel marks the minimum value (0.016 mag) for setting the extendedness parameter to 1. The bottom two panels show the  $r$  vs.  $g - r$  color-magnitude diagrams for 14,701 unresolved (left) and 163,666 resolved (right) sources. Note the unresolved sample suffers from increasing contamination by galaxies for  $r > 24$ .

2406 fluxes and errors are derived from linear flux fits with a 2416  
 2407 fixed shape and centroid.

2408 Efforts are underway to investigate and quantify the 2417  
 2409 origin of uncertainty underestimates and future releases 2418  
 2410 will, at the least, provide recommendations for mitiga- 2419  
 2411 tions. 2420

## 2412 5.8. Difference Imaging

2413 We assessed the performance of image differencing using 2426  
 2414 both human vetting (§5.8.1) and source injection 2427  
 2415 (§5.8.2). 2428

### 5.8.1. Difference Imaging Purity

2417 Members of the DP1 team labeled more than 11,000  
 2418 DIASource image triplets, each consisting of cutouts  
 2419 from the science, template, and difference images. An  
 2420 internal labeling service (`tasso`) was deployed within  
 2421 the USDF environment. A random subset of approx-  
 2422 imately 16,000 DIASources was selected and uploaded  
 2423 to the service, which remained active for roughly three  
 2424 months and labeled by members of the DP1 team. Users  
 2425 labeled DIASource PNG images triplets, each consist-  
 2426 ing of cutouts from the science, template, and differ-  
 2427 ence images. Each stamp had dimensions of  $51 \times 51$  pix-  
 2428 els, matching the input size required by the machine-

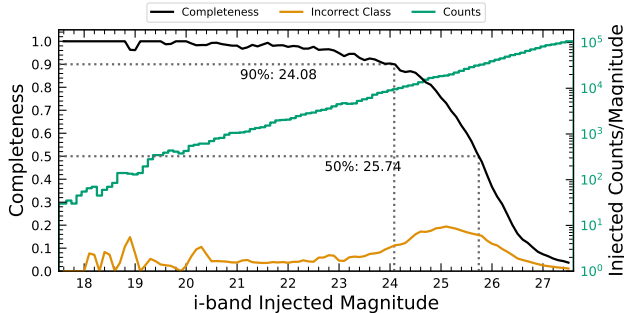


**Figure 29.** Completeness and incorrect classification fraction as a function of  $i$ -band CModel magnitude (Reference Magnitude) for DC2-based injected objects into a portion of the ECDFS field. The “Incorrect Class” line shows the proportion of objects that are matched but classified incorrectly by their reference-band extendedness, i.e. stars with extendedness of 1 or galaxies with extendedness of 0 in the reference band.

2429 learning model. Access to the labeling service was  
 2430 granted to all individuals with commissioning data ac-  
 2431 cess. Each DIASource was classified exactly once, with  
 2432 a total of 35 volunteers contributing labels. Figure 35  
 2433 show an example of one of the image triplets consist-  
 2434 ing of cutouts from the science, template, and difference  
 2435 images that volunteers were asked to label.

2437 The labeled sources were classified into multiple cat-  
 2438 egories representing real astrophysical events and arti-  
 2439 facts. Prior to any filtering, the raw artifact-to-real ratio  
 2440 was approximately 9:1. Bright stars were identified as  
 2441 the dominant source of artifacts, while correlated noise,  
 2442 particularly in the  $u$  and  $g$  bands, also produced spur-  
 2443 ious detections near the flux threshold. We expect to be  
 2444 able to mitigate these effects in future LSSTCam data.

2445 Applying a reliability threshold based on the Machine  
 2446 Learning reliability model described in §4.6.1 improved  
 2447 the purity of transient detections but had limited im-  
 2448 pact on variable stars. This limitation arises from tech-  
 2449 nical constraints at the time of model training, which  
 2450 prevented the injection of variable stars into the syn-  
 2451 thetic training set. Future reliability models for LSST-  
 2452 Cam data, described in §4.6.1, will be trained using a  
 2453 broader and more representative range of input data.

2454 The performance of the reliability model on the test  
 2455 data (§4.6.1) is shown in Figure 36. The rate of true  
 2456 positives and false negatives obtained by thresholding  
 2457 the reliability score at 0.5 is reported for transients (99  
 2458 stamps), and variable stars (316 stamps) vetted in `tasso`  
 2459 in Table 6.

2460 Additionally we crossmatched stamps  
 2461 with Solar System Objects with known orbits retrieving  
 2462 5,988 Solar System Objects stamps.

**Table 6.** The rate of true positives (TP) and false negatives (FN) obtained by thresholding the reliability score at 0.5 for Solar system objects, transients and variable stars.

| Object Type  | Number | TP Rate | FN Rate |
|--------------|--------|---------|---------|
| Solar System | 5,988  | 93.5%   | 6.5%    |
| Transients   | 99     | 73.7%   | 26.3%   |
| Variables    | 316    | 3.5%    | 96.5%   |

### 2464 5.8.2. Difference Imaging Detection Completeness

2465 We assess the performance of our difference imaging  
 2466 pipeline using synthetic source injection on the science  
 2467 images prior to differencing. We construct a catalog of  
 2468 injected sources by joining two different samples of point  
 2469 sources, a set of hosted sources to emulate transients in  
 2470 galaxies and second set of hostless sources. The hosts  
 2471 are selected from the pipeline source catalog that is pro-  
 2472 duced upstream by imposing a cut on their extendedness  
 2473 measurement and selecting  $N_{\text{src}} = \min(100, N \times 0.05)$  of  
 2474 the  $N$  available sources per detector. For each host we  
 2475 pick a random position angle and radius using its light  
 2476 profile shape to decide where to place the source, and  
 2477 also a random value of brightness for the injected source,  
 2478 with magnitudes higher than the host source.

2479 The hostless sources instead have random positions  
 2480 in the CCD focal plane, and magnitudes chosen from a  
 2481 random uniform distribution with  $20 \geq m \geq m_{\text{lim}} + 1$ ,  
 2482 where  $m_{\text{lim}}$  is the limiting magnitude of the image. We  
 2483 used the LSST `source_injection` package<sup>107</sup> to include  
 2484 these sources in our test images. We performed a coordi-  
 2485 nate cross-match task, with a threshold of 0.5 to find  
 2486 which of these sources were detected and which were  
 2487 lost, enabling the calculation of a set of performance  
 2488 metrics.

2489 In Figure 37 we show the detection completeness as  
 2490 a function of the SNR, for sources in the ECDFS field,  
 2491 for filters  $griz$ . We observe a completeness  $> 95\%$   
 2492 for sources with  $\text{SNR} > 6$ , with mean completeness  $\simeq 99\%$   
 2493 and standard deviation of  $\simeq 0.7\%$ . In Figure 38 we  
 2494 show the distribution of the residuals of the recovered  
 2495 sky coordinates for the detected synthetic sources. The  
 2496 marginal distributions are both centered at zero, and  
 2497 for sources of  $\text{SNR} > 20$  the residuals are compatible  
 2498 with normal distributions  $\mathcal{N}(\mu = 0, \sigma^2 = (0''.02)^2)$ . In  
 2499 Figure 39 we show photometry results for our detected  
 2500 synthetic sources in the  $i$  filter, using PSF photometry

<sup>107</sup> <https://pipelines.lsst.io/modules/lsst.source.injection/index.html>

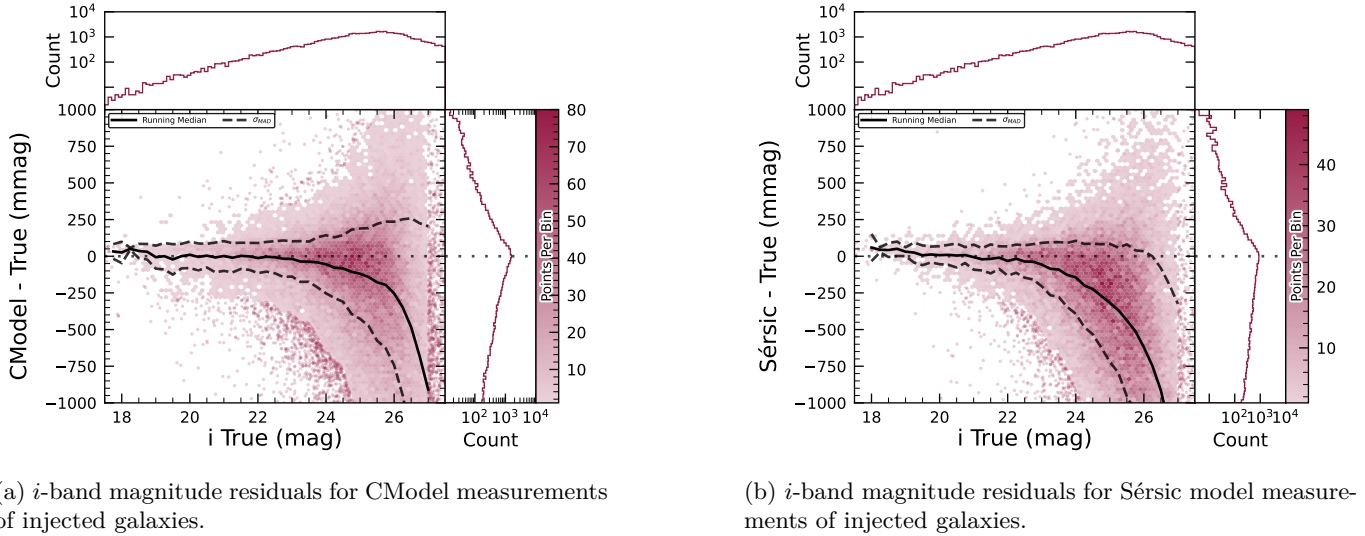


**Figure 30.**  $i$ -band magnitude residuals for matched injected DC2 galaxies with the CModel and Sérsic algorithms in a portion of the ECDFS region, including the median and scatter thereof. The black line is the median.

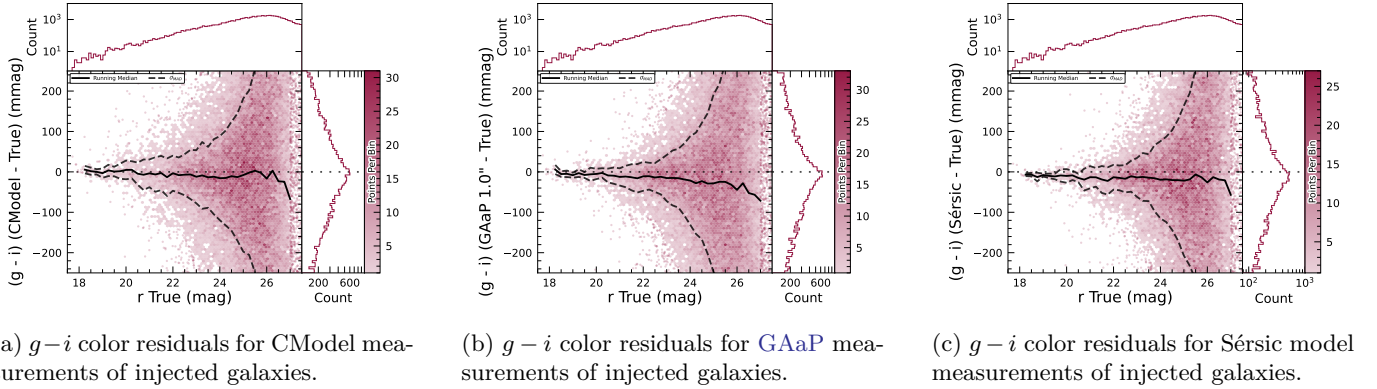


**Figure 31.**  $g-i$  color residuals versus true  $r$ -band magnitude for matched injected DC2 galaxies with the CModel, GAaP and Sérsic algorithms in a portion of the ECDFS region.

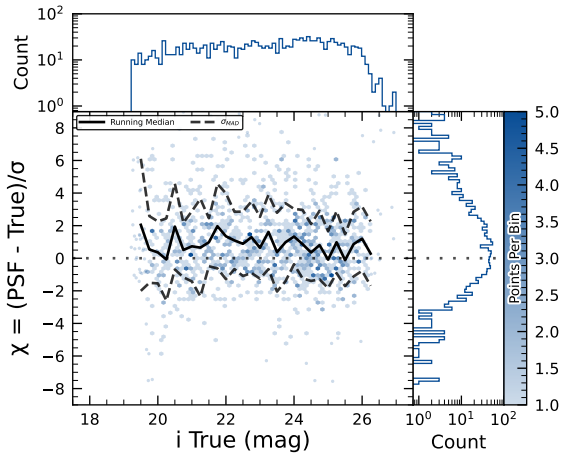
2503 on the difference images. We include both the mag- 2521  
 2504 nitude residuals as well as the flux pulls, defined as 2522  
 2505  $(f_{PSF} - f_{True})/\sigma_{f_{PSF}}$ , where  $f_{True}$  is the true flux,  $f_{PSF}$  2523  
 2506 is the PSF flux and  $\sigma_{f_{PSF}}$  is its uncertainty, as a function 2524  
 2507 of the true magnitude of the synthetic sources, includ- 2525  
 2508 ing the running median and median absolute deviation 2526  
 2509 (MAD) for the whole brightness range. We also include 2527  
 2510 the true magnitude distribution as well as the detection 2528  
 2511 completeness on the top panel, and for reference the 2529  
 2512 90% and 50% completeness magnitude values in vertical 2530  
 2513 lines. On the right panels we include the marginal dis- 2531  
 2514 tribution for sources brighter than 22.5 mag, splitting 2532  
 2515 the data into hosted and hostless, as well as the robust 2533  
 2516 mean and standard deviation. From this figure we can 2534  
 2517 see that our flux measurements are accurate within a 2535  
 2518 wide range of magnitudes, for both hosted and hostless 2536  
 2519 synthetic sources. We find that the median offset is be- 2537  
 2520 low 0.002 mag for true magnitudes below 21, and with a 2538

2521 maximum  $\sigma_{MAD}$  scatter of about 0.02 mag in this range. 2522  
 2523 For true  $m_i < 22.5$ , the robust running median PSF 2524  
 2525 magnitudes residuals are  $< 0.02$  mag, and when split- 2526  
 2527 ting into hosted and hostless both robust median are 2527  
 2528 well below 0.01, and robust  $\sigma$ , i.e.  $\sigma_{MAD}$  are also well 2528  
 2529 below 0.05. For all sources with  $m_i < 21.5$  the running 2529  
 2530 median is always  $|\langle \delta \rangle| < 0.1$ , and MAD  $\sigma_\delta < 1$ . Extend- 2530  
 2531 ing to sources with  $m_i < 22.5$  then hostless sources have 2531  
 2532 a robust mean pull below 0.02, with a robust standard 2532  
 2533 deviation  $< 1.15$ , while these parameters increase to 0.2 2533  
 2534 and 1.2 for hosted sources, suggesting that we might 2534  
 2535 have contamination from host background sources po- 2535  
 2536 tentially biasing our fluxes. 2536

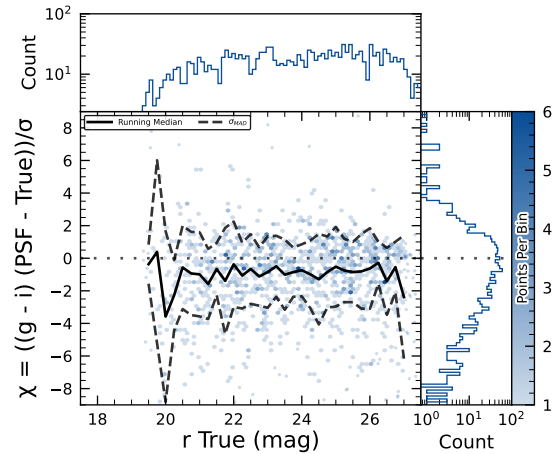
## 5.9. Solar System

### 5.9.1. Asteroid Linking Performance

2537 The evaluation of asteroid linking performance in DP1 2537  
 2538 focused on demonstrating discovery capability. The so- 2538

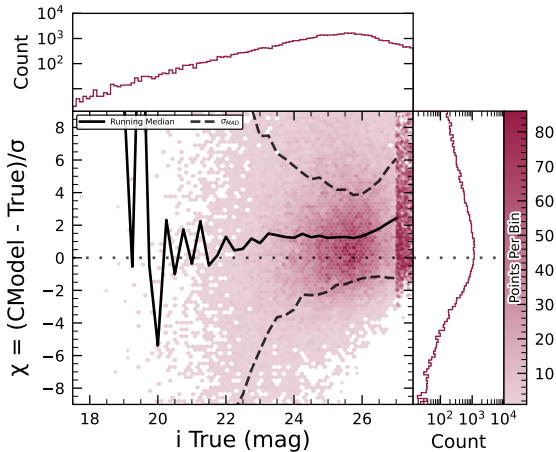


(a)  $i$ -band flux uncertainty-scaled residuals for PSF model measurements of injected stars.

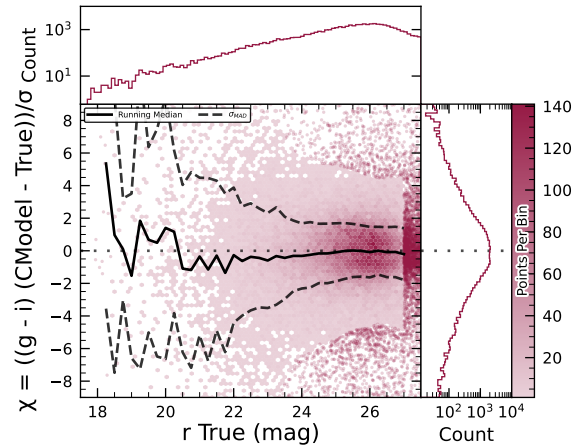


(b)  $g-i$  color uncertainty-scaled residuals for PSF model measurements of injected stars.

**Figure 32.** Color and flux uncertainty-scaled residuals for matched injected DC2 stars' PSF model measurements in a portion of the ECDFS region.



(a)  $i$ -band flux uncertainty-scaled residuals for CModel measurements of injected galaxies.



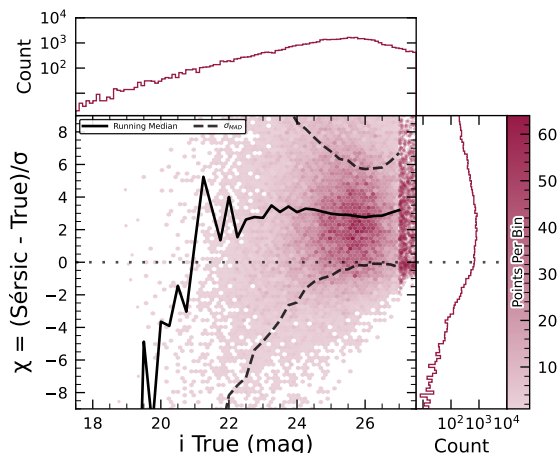
(b)  $g-i$  color uncertainty-scaled residuals for CModel measurements of injected galaxies.

**Figure 33.** Color and flux uncertainty-scaled residuals for matched injected DC2 galaxies' CModel measurements in a portion of the ECDFS region.

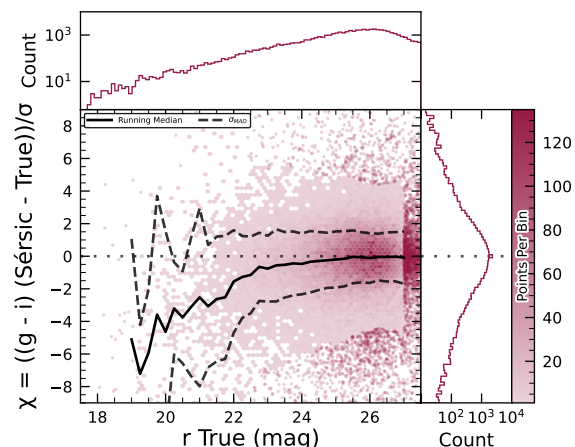
2539 lar system discovery pipeline produced 269,581 track- 2553  
 2540 lets, 5,691 linkages, and 281 post-processed candidates. 2554

2541 As described in §4.6.3, post-processing of the heli- 2555  
 2542 olinc output with link\_purify produced a final set of 2556  
 2543 281 candidate linkages, ranked with the most promising 2557  
 2544 first. We then used find\_orb (B. Gray 2025) to derive 2558  
 2545 orbit fits for each candidate, sorting the resulting list by 2559  
 2546  $\chi_{\text{dof}}^2$ , a measure of fit quality. A conservative manual 2560  
 2547 investigation of these candidates yielded a curated 2561  
 2548 list of 93 probable new asteroid discoveries. Manual 2562  
 2549 inspection of the linkages indicated that those ranked 2563  
 2550 0–137 corresponded to unique real asteroids; ranks 138– 2564  
 2551 200 contained additional real objects intermixed with 2565  
 2552 some spurious linkages; and ranks higher than 200 were 2566

essentially all spurious. This analysis indicates that it  
 will be possible to identify cuts on quality metrics such  
 as  $\chi^2$  to define discovery candidate samples with high  
 purity; determining the exact quantitative cut values re-  
 quires more data with LSSTCam. We next removed all  
 observations matched to known asteroids (using Minor  
 Planet Center (MPC)'s MPCChecker service), reducing  
 the number of candidates to 97. Of these, four had  
 strong astrometric and/or photometric outliers, likely  
 due to self-subtraction in difference images due to the  
 unavoidable limitations of template generation from the  
 limited quantity of data available from LSSTComCam.  
 We suspect these four linkages do correspond to real ob-  
 jects, but have chosen to discard them out of an abun-



(a)  $i$ -band flux uncertainty-scaled residuals for Sérsic model measurements of injected galaxies.



(b)  $g-i$  color uncertainty-scaled residuals for Sérsic model measurements of injected galaxies.

**Figure 34.** Color and flux uncertainty-scaled residuals for matched injected DC2 galaxies' Sérsic measurements in a portion of the ECDFS region.

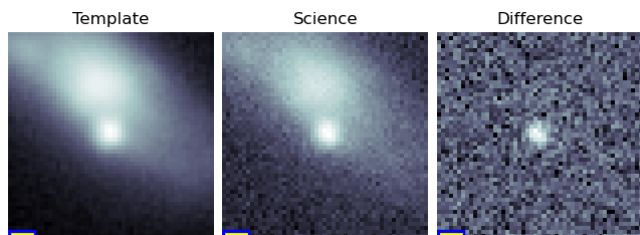


**Figure 35.** An example an image triplet consisting of cutouts showing, from left to right, the template, science, and difference images that volunteers were asked to label.

2567 dance of caution. The remaining 93 were submitted to  
 2568 the Minor Planet Center and accepted as discoveries,  
 2569 demonstrating the LSST pipelines are able to success-  
 2570 fully discover new solar system objects.

### 5.9.2. Asteroid Association Performance

2572 During the Solar System association step, 5988 Di-  
 2573 aSources were linked to 431 unique Solar System ob-  
 2574 jects. These include 3,934 DiaSources with 338 previ-  
 2575 ously known objects cataloged by the MPC, and 2,054  
 2576 DiaSources with the 93 newly-discovered objects, all of  
 2577 which are main belt asteroids. An additional 143 de-  
 2578 tectations of these newly discovered objects were also re-  
 2579 covered. These detections were not initially identified  
 2580 by the discovery pipelines, as they did not meet the  
 2581 required criteria for tracklet formation, specifically the  
 2582 minimum number of detections and/or the maximum  
 2583 allowed time span between observations.

2584 The astrometric residuals of known asteroid associa-  
 2585 tions are shown in Figure 40. The astrometric precision  
 2586 for solar system sources is excellent, with the majority of  
 2587 objects detected within  $0''.1$  of their expected positions.

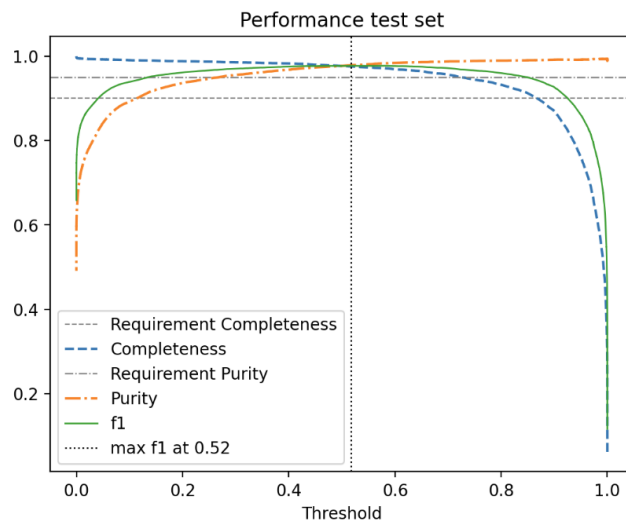


**Figure 36.** The purity and completeness of the reliability score is shown as a function of reliability threshold based on the testing data. A vertical line marks the threshold where the highest F1-score is obtained. The F1 score is the harmonic mean of completeness and purity. See §4.6.1 for details on the model and model training.

2588 By analyzing the signed median residuals to search for  
 2589 biases, we find that previously-known objects have mean  
 2590 residuals of  $0''.001$  and  $-0''.016$  in the RA and Dec di-  
 2591 rections respectively, whereas newly-discovered objects  
 2592 have mean residuals of  $-0''.035$  and  $-0''.010$  in the RA  
 2593 and Dec directions, respectively. These mean residuals  
 2594 are small enough to eliminate the possibility of a tim-  
 2595 ing offset greater than the second-scale shutter motion,  
 2596 which is consistent with the timing studies presented in  
 2597 §2.2.2.

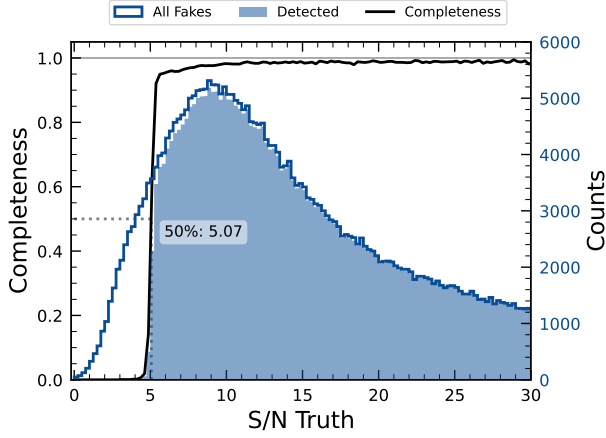


**Figure 37.** The difference image detection completeness for injected sources in the ECDFS field, for filters *griz*, as a function of the estimated signal to noise ratio SNR. This completeness is the ratio between the found fake sources (shaded histogram) and all the sources (solid line). The horizontal dashed line represents where the 50% completeness level is reached, at approximately  $\text{SNR} \simeq 5.07$ .

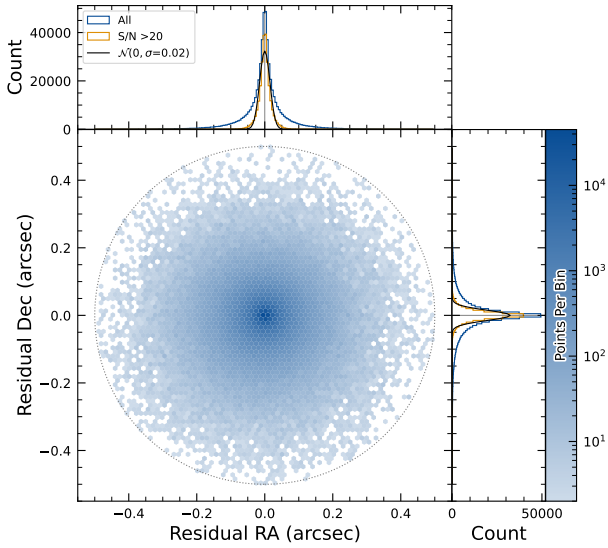


**Figure 38.** Coordinate residuals for detected synthetic sources in difference images, between recovered and true position of the sources in the ECDFS field. In the top and right panels we include the distribution of these offsets, for all sources as well as for sources with  $\text{SNR} > 20$ . These high SNR sources show gaussian coordinate residual distributions with  $\sigma = 0''.02$  (black solid lines). The circle reflects the matching radius of  $0''.5$ .

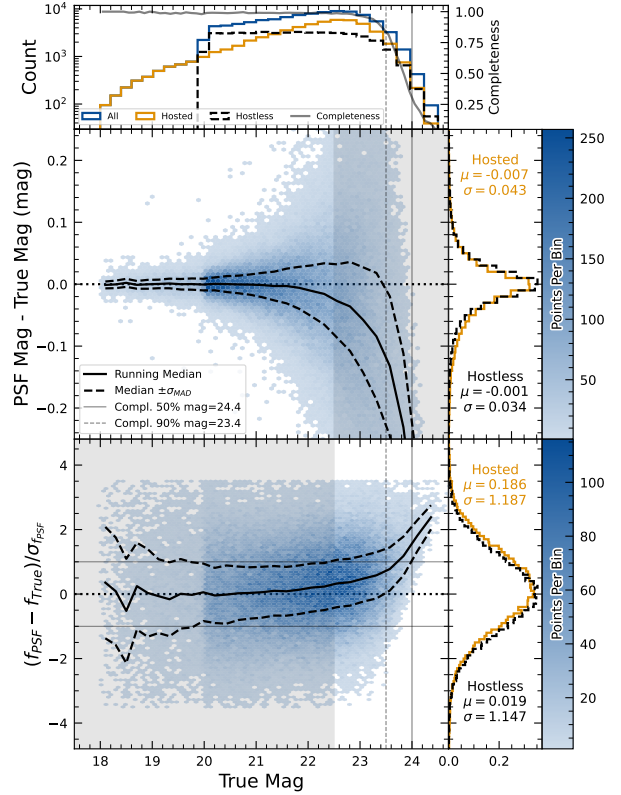


**Figure 39.** Magnitude residuals and flux pulls for *i*-band PSF photometry on difference images for ECDFS field in *i* for detected injected sources. Top panel: Distribution of true magnitudes for injected sources (blue), and split into hostless (black dash) and hosted (orange) sources, with detection completeness as a function of true magnitude (gray line). Vertical dashed lines indicate the 90% and 50% completeness magnitude limits. Center left panel: 2D hexbin plot of PSF magnitude residuals (measured minus true) versus true magnitude for detected sources, with running median (solid black) and  $\sigma_{MAD}$  (dashed black) overlaid. Center right panel: Marginalized distributions of PSF magnitude residuals for hostless (blue) and hosted (orange) sources with true magnitude  $m_i < 22.5$ , annotated with robust mean and standard deviation. Bottom left panel: 2D hexbin plot of PSF flux pulls versus true magnitude for detected sources, with running median (solid black) and  $\sigma_{MAD}$  (dashed black) overlaid. Bottom right panel: Marginalized distributions of PSF flux pulls for hostless (blue) and hosted (orange) sources with true magnitude  $m_i < 22.5$ , annotated with robust mean and standard deviation.

2598 The wider scatter in the RA residuals is due to ob-  
 2599 jects whose measured orbital elements are less well con-

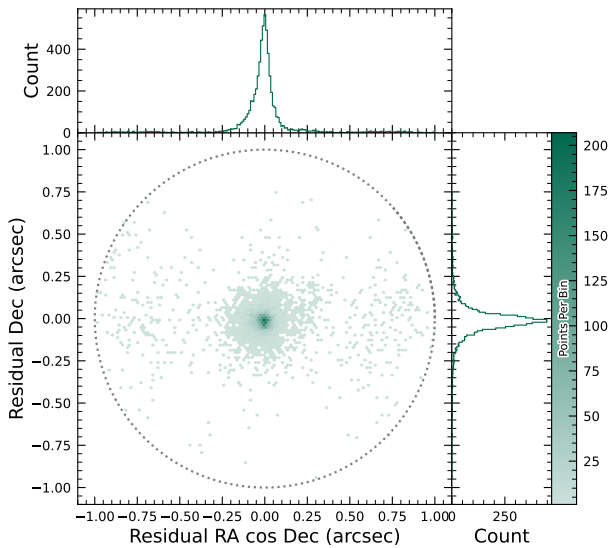


**Figure 40.** Astrometric residuals between expected and observed positions of Solar System Objects in DP1. The median residuals are  $0''.001$  and  $-0''.016$  in R.A./Dec direction, with standard deviations of  $0''.19$  and  $0''.10$ , respectively. No detectable systematic offset from zero indicates there are no major errors in either timing or astrometry delivered by the Rubin system. The wider scatter in the RA direction is due to objects whose measured orbital elements are less well constrained, translating to larger along-track positional errors in the predicted positions.

strained, translating to larger along-track positional errors in the predicted positions. Observations of objects with large residuals are the most valuable ones from the point of view of improving the orbit, which is why we kept a generous matching radius. However, in future releases we are likely to couple this with either orbit fitting to verify the “singleton” match, or require two near-in-time observations (a tracklet) that match the expected motion vector as well.

Optimal moving source attribution is an area of active work that we expect to fully converge in time of Data Release 1 (DR1). In the meantime, for DP1 we’ve opted to start with simple, more easily understandable, criteria.

### 5.10. Crowded Fields

Among the seven Rubin DP1 target fields, two stand out for their severe stellar crowding: the globular cluster 47 Tucanae (47\_Tuc) and the Fornax dwarf spheroidal galaxy (Fornax dSph). These fields were selected in part to stress-test the LSST Science Pipelines under high-density conditions. While both exhibit high stellar den-

sities, the nature and spatial extent of the crowding differ significantly.

47 Tuc presents extreme crowding across much of the field, encompassing its dense core and the eastern regions influenced by the Small Magellanic Cloud (SMC). This pervasive crowding leads to persistent challenges for deblending and reliable source detection, exposing field-wide limitations in the current pipeline performance (Y. Choi et al. 2025). In contrast, Fornax dSph shows significant crowding only in its central region, with outer areas remaining well resolved and easier to process.

In both 47 Tuc and Fornax, extreme crowding led to the deblending step being skipped frequently when memory or runtime limits were exceeded, typically due to an excessive number of peaks, or large parent footprints. However, the impact of these limitations differed: in 47 Tuc, deblending was often skipped across the entire field, resulting in large gaps and substantially reduced completeness. In Fornax, these issues were largely confined to the central region, with much better recovery in the outskirts. This contrast highlights how the pipeline’s limitations depend on the spatial extent of high-density regions: 47 Tuc exposed systematic, field-wide challenges, whereas Fornax revealed more localized, density-driven limits.

T. M. Wainer et al. (2025) explored the Rubin DP1 DiaObject catalog (§3.2) in the 47 Tuc field, which contains sources detected in difference images. Because forced photometry is performed at these positions across all single-epoch images, this dataset bypasses the coadd-based detection and deblending stages that often fail in crowded regions. By computing the median of the forced photometry for each DiaObject across available visits, they recovered approximately three times more candidate cluster members than found in the standard Object table (Y. Choi et al. 2025). This result underscores the value of difference-imaging-based catalogs for probing dense stellar regions inaccessible to standard coadd processing in DP1.

Although the DP1 pipeline was not optimized for crowded-field photometry, these early studies of 47 Tuc and Fornax provide critical benchmarks. They highlight both the limitations and opportunities for science with Rubin data in crowded environments, and they inform future pipeline development aimed at robust source recovery in complex stellar fields.

## 6. RUBIN SCIENCE PLATFORM

The RSP (M. Jurić et al. 2019) is a powerful, cloud-based environment for scientific research and analysis of petascale-scale astronomical survey data. It serves

as the primary interface for scientists to access, visualize, and conduct next-to-the-data analysis of Rubín and LSST data. The RSP is designed around a “bring the compute to the data” principle, eliminating the need for users to download massive datasets. Although DP1 is much smaller in size (3.5 TB) than many current survey datasets, future LSST datasets will be far larger and more complex, making it crucial to co-locate data and analysis for effective scientific discovery.

The RSP provides users with access to data and services through three distinct user-facing Aspects: a *Portal*, which facilitates interactive exploration of the data; a JupyterLab-based *Notebook* environment for data analysis using Python; and an extensive set of *Application Programming Interfaces (APIs)* that enable programmatic access to both data and services. The three Aspects are designed to be fully integrated, enabling seamless workflows across the RSP. The data products described in §3 are accessible via all three Aspects, and the system facilitates operations such as starting a query in one Aspect and retrieving its results in another. Figure 41 shows the Rubín Science Platform landing page in the Google cloud.

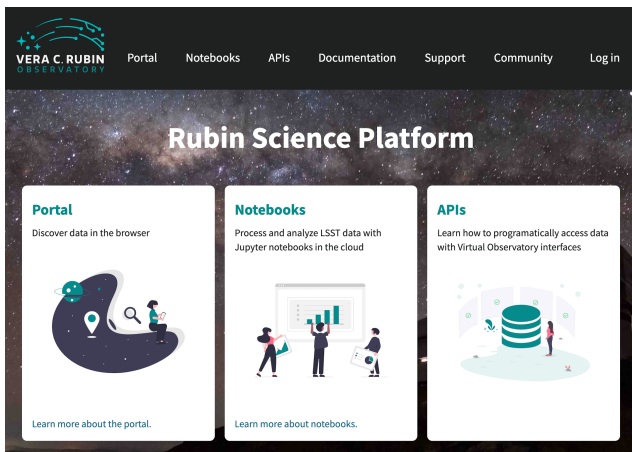


**Figure 41.** The Rubín Science Platform landing page at <https://data.lsst.cloud/> showing the three user-facing Aspects as well as links to documentation and support information.

The RSP is supported by a number of back-end services, including databases, files, and batch computing. Support for collaborative work through shared workspaces is also included in the RSP.

A preview of the RSP was launched on Google Cloud in 2022, operating under a shared-risk model to support Data Preview 0 (W. O’Mullane et al. 2024a). This allowed the community to test the platform, begin preparations for science, and provide valuable feedback to inform ongoing development. It was the first time an as-

tronomical research environment was hosted in a cloud environment. The DP1 release brings major updates to RSP services, enhancing scientific analysis capabilities. The RSP remains under active development, with incremental improvements being rolled out as they mature. During the Rubín Early Science Phase, the RSP will continue to operate under a shared-risk model. This section outlines the RSP functionality available at the time of the DP1 release and provides an overview of planned future capabilities.

### 6.1. Rubín Data Access Center

The Rubín US Data Access Center (US DAC) utilizes a novel hybrid on-premises-cloud architecture, which combines on-premises infrastructure at the USDF at SLAC with flexible and scalable resources in the Google cloud. This architecture has been deployed and tested using the larger simulated data set of DP0.2 (W. O’Mullane et al. 2024b).

In this hybrid model, user-facing services are deployed in the cloud to support dynamic scaling in response to user demand and to simplify the provisioning and management of large numbers of science user accounts. The majority of the static data products described in §3 are stored on-premises at the USDF to benefit from cost-effective mass storage and close integration with Rubín data processing infrastructure, also located at the USDF. For imaging data, the Data Butler (§6.2.2) provides the interface between the cloud-based users and data services, and the on-premises data. For catalog data, a cloud-based TAP client (§6.2.1) submits queries to the on-premises Qserv database cluster (§6.5) and retrieves the results. In the initial DP1 deployment, catalog data is hosted at the USDF while image data is stored in the cloud. The full hybrid model will be rolled out and further tested following the release of DP1. The RSP features a single-sign-on authentication and authorization system to provide secure access for Rubín data rights holders (R. Blum & the Rubín Operations Team 2020).

### 6.2. API Aspect

The API Aspect provides a comprehensive set of user-facing interfaces for programmatic access to the DP1 data products, through both IVOA-compliant services and the Rubín Data Butler. IVOA services enable standard queries and integration with existing tools, while the Butler facilitates advanced data processing within the LSST Science Pipelines.

At the time of the DP1 release, some IVOA services are unavailable, and certain data products are only accessible via the Butler. This section provides

2757 an overview of the available [IVOA](#) services and Butler  
2758 access.

### 2759 6.2.1. *IVOA Services*

2760 Rubin has adopted a [Virtual Observatory \(VO\)](#)-first  
2761 design philosophy, prioritizing compliance with [IVOA](#)  
2762 standard interfaces to foster interoperability, standard-  
2763 ization, and collaboration. In cases where standardized  
2764 protocols have yet to be established, additional services  
2765 have been introduced to complement these efforts. This  
2766 approach ensures that the RSP can be seamlessly inte-  
2767 grated with community-standard tools such as [Tool for](#)  
2768 [OPerations on Catalogues And Tables \(TOPCAT\)](#) (M.  
2769 Taylor 2011) and [Aladin](#) (F. Bonnarel et al. 2000; T.  
2770 Boch & P. Fernique 2014; M. Baumann et al. 2022), as  
2771 well as libraries such as [PyVO](#) (M. Graham et al. 2014).

2772 The user-facing [APIs](#) are also used internally within  
2773 the RSP, creating a unified design that ensures consis-  
2774 tent and reproducible workflows across all three Aspects.  
2775 This reduces code duplication, simplifies maintenance,  
2776 and ensures all users, both internal and external, access  
2777 data in the same way. For example, an [Astronomical](#)  
2778 [Data Query Language \(IVOA standard\) \(ADQL\)](#) query  
2779 on the [Object](#) catalog via [TAP](#) yields identical results  
2780 whether run from the Portal, Notebook, or an external  
2781 client.

2782 The following [IVOA](#) services are available at the time  
2783 of the [DP1](#) release:

- 2784 • **Table Access Protocol (TAP) Service:** A  
2785 TAP service (P. Dowler et al. 2019) enables queries  
2786 of catalog data via the [IVOA](#)-standard [ADQL](#), a  
2787 dialect of [SQL92](#) with spherical geometry exten-  
2788 sions. The main TAP service for [DP1](#) runs on the  
2789 Rubin-developed [Qserv](#) database (§ 6.5), which  
2790 hosts the core science tables described in §3.2, as  
2791 well as the [Visit](#) database. It also provides image  
2792 metadata in the [IVOA ObsCore](#) format via the  
2793 standard `ivoa.ObsCore` table, making it an “Ob-  
2794 sTAP” service (ObsTAP; M. Louys et al. 2017).  
2795 The TAP service is based on the [Canadian As-](#)  
2796 [tronomy Data Centre \(CADC\)](#)’s open-source Java  
2797 TAP implementation<sup>108</sup>, modified for the exact  
2798 query language accepted by [Qserv](#). It currently  
2799 supports a large subset of [ADQL](#), with limitations  
2800 documented in the data release materials (see §7.1)  
2801 and exposed via the TAP **capabilities** endpoint  
2802 where possible.

2803 The TAP service provides metadata annotations  
2804 consistent with the standard, including table and

2805 column descriptions, indications of foreign-key rela-  
2806 tionships between tables, and column metadata  
2807 such as units and [IVOA Unified Content Descrip-](#)  
2808 [tors \(UCDs\)](#).

- **Image Access Services:** Rubin image access services are compliant with [IVOA SIAv2](#) (Simple Image Access Protocol, version 2; T. Jenness et al. 2024; P. Dowler et al. 2015) for discovering and accessing astronomical images based on metadata. SIAv2 is a [REpresentational State Transfer \(REST\)](#)-based protocol designed for the discovery and retrieval of image data. It allows, for instance, querying all images in a given band over a defined sky region and time period.

Users identify an image or observation of interest and query the service. The result set includes metadata about the image, such as the sky position, time, or band, and a data access URL, which includes an [IVOA Identifier](#) uniquely identifying the dataset (T. Jenness & G. P. Dubois-Felsmann 2025), allowing the dataset to be retrieved or a cutout requested via [Server-side Operations for Data Access \(IVOA standard\) \(SODA\)](#).

- **Image Cutout Service:** The Rubin Cutout Service (R. Allbery 2023, 2024) is based on the [IVOA SODA](#) standard (F. Bonnarel et al. 2017). Users submit requests specifying sky coordinates and the cutout size as the radius from the coordinates, and the service performs the operation on the full image and returns a result set. For [DP1](#), the cutout service is a single cutout service only where  $N$  cutout requests will require  $N$  independent synchronous calls. We expect some form of bulk cutout service by mid 2026.

- **HiPS Data Service:** An authenticated [HiPS](#) (P. Fernique et al. 2017) data service for seamless pan-and-zoom access to large-scale co-adds. It supports fast interactive progressive image exploration at a range of resolutions.

- **WebDAV:** A [Web Distributed Authoring and Versioning \(WebDav\)](#) service is provided to enable users to remotely manage, edit, and organize files and directories on the RSP as if they were local files on their own computer. This is especially useful for local development.

### 2850 6.2.2. *Data Butler*

2851 The Rubin Data Butler (T. Jenness et al. 2022; N. B.  
2852 Lust et al. 2023), is a high-level interface designed to

<sup>108</sup> <https://github.com/opencadc/tap>

2853 facilitate seamless access to data for both users and  
 2854 software systems. This includes managing storage for-  
 2855 mats, physical locations, data staging, and database  
 2856 mappings. A [Butler](#) repository contains two compo-  
 2857 nents:

- 2858 • the *Data Store*: A physical storage system for  
 2859 datasets, e.g., a [Portable Operating System Inter-](#)  
 2860 [face \(POSIX\)](#) file system or S3 object store; and
- 2861 • the *Registry*: An [Structured Query Language](#)  
 2862 [\(SQL\)](#)-compatible database that stores metadata  
 2863 about the datasets in the data store.

2864 For DP1, the Butler repository is hosted in the Google  
 2865 Cloud, using an [\(Amazon\) Simple Storage Service](#)  
 2866 [\(S3\)](#)-compatible store for datasets and AlloyDB, a  
 2867 PostgreSQL-compatible database, for the registry.

2868 In the context of the [Butler](#), a *dataset* refers to a  
 2869 unique data product, such as an image, catalog or map,  
 2870 generated by the observatory or processing pipelines  
 2871 Datasets belong to one of the various types of data  
 2872 products, described in §3. The [Butler](#) ensures that  
 2873 each dataset is uniquely identifiable by a combination  
 2874 of three pieces of information: a data coordinate,  
 2875 a dataset type, and a run collection. For example,  
 2876 a dataset that represents a single raw image in the  
 2877 *i* band taken on the night starting 2024-11-11 with  
 2878 exposure ID 2024111100074 would be represented as  
 2879 `dataId='exposure':2024111100074, 'band':'i',`  
 2880 `'instrument':'LSSTComCam'` and is associated with  
 2881 the `raw` DatasetType. For a deep coadd on a `patch`  
 2882 of sky in the Seagull field, there would be no exposure di-  
 2883 mensions and instead the tract, `patch` and band would  
 2884 be specified as `dataId='tract':7850, 'patch':`  
 2885 `6, 'band':'g', 'instrument':'LSSTComCam',`  
 2886 `skymap='lsst_cells_v1'` and is associated with the  
 2887 `deep_coadd` DatasetType. The tract identification  
 2888 numbers and corresponding target names for these  
 2889 tracts are listed in [Table 7](#).

2890 The data coordinate is used to locate a dataset in  
 2891 multi-dimensional space, where dimensions are defined  
 2892 in terms of scientifically meaningful concepts, such as  
 2893 instrument, visit, detector or band. For example, a cali-  
 2894 brated single-visit image (§3.1) has dimensions includ-  
 2895 ing band, instrument, and detector. In contrast, the  
 2896 visit table (§3.2), a catalog of all calibrated single-epoch  
 2897 visits in DP1, has only the instrument dimension. The  
 2898 main dimensions used in DP1 are listed, together with a  
 2899 brief description, in [Table 8](#). To determine which dimen-  
 2900 sions are relevant for a specific dataset, the [Butler](#) de-  
 2901 fines dataset types, which associate each dataset with its  
 2902 specific set of relevant dimensions, as well as the associ-  
 2903 ated Python type representing the dataset. The dataset

**Table 7.** Tract coverage of each DP1 field. The size of a tract is larger than the LSSTComCam field of view; however, since each observed field extends across more than one tract, each field covers multiple tracts.

| Field Code       | Tract ID                                 |
|------------------|--|
| 47_Tuc           | 453, 454                                 |
| ECDFS            | 4848, 4849, 5062, 5063, 5064             |
| EDFS_comcam      | 2234, 2235, 2393, 2394                   |
| Fornax_dSph      | 4016, 4017, 4217, 4218                   |
| Rubin_SV_095_-25 | 5305, 5306, 5525, 5526                   |
| Rubin_SV_38_7    | 10221, 10222, 10463, 10464, 10704, 10705 |
| Seagull          | 7610, 7611, 7849, 7850                   |

2904 type defines the kind of data a dataset represents, such  
 2905 as a raw image (`raw`), a processed catalog (`object_`  
 2906 `forced_source`), or a sky map (`skyMap`). [Table 9](#) lists  
 2907 all the dataset types available via the Butler in DP1, to-  
 2908 gether with the dimensions needed to uniquely identify  
 2909 a specific dataset and the number of unique datasets of  
 2910 each type.

2911 It is important to highlight a key difference between  
 2912 accessing catalog data via the [TAP](#) service versus the  
 2913 Butler. While the [TAP](#) service contains entire catalogs,  
 2914 many of the same catalogs in the Butler are split into  
 2915 multiple separate catalogs. This is partly due to how  
 2916 these catalogs are generated, but also because of the  
 2917 way data is stored within and retrieved from the Butler  
 2918 repository – it is inefficient to retrieve the entire `Source`  
 2919 catalog, for example, from the file system. Instead, be-  
 2920 cause the `Source` catalog contains data for sources de-  
 2921 tected in the `visit_images`, there is one `Source` catalog  
 2922 in the Butler for each `visit_image`. Similarly, there is  
 2923 one `Object` catalog for each `deep_coadd`. All the cata-  
 2924 logs described in §3.2, aside from the `CcdVisit`, `SSOb-`  
 2925 `ject`, `SSSource`, and `Calibration` catalogs, are split  
 2926 within the Butler.

2928 A dataset is associated with one or more *Collections*;  
 2929 logical groupings of datasets within the [Butler](#) system  
 2930 that were created or processed together by the same  
 2931 batch operation. Collections allow multiple datasets  
 2932 with the same data coordinate to coexist without con-  
 2933 flict. Collections support flexible, parallel processing by  
 2934 enabling repeated analyses of the same input data using  
 2935 different configurations. The DP1 Butler is read-only; a  
 2936 writeable Butler is expected by mid-2026.

### 6.2.3. Remote Programmatic Access

2938 The Rubin [RSP API](#) can be accessed from a local sys-  
 2939 tem by data rights holders outside of the [RSP](#), by creat-

**Table 8.** Descriptions of and valid values for the key data dimensions in DP1. YYYYMMDD signifies date and # signifies a single 0–9 digit.

| Dimension       | Format/Valid values                | Description   |
|-----------------|------------------------------------|---|
| day_obs         | YYYYMMDD                           | A day and night of observations that rolls over during daylight hours.  |
| visit           | YYYYMMDD#####                      | A sequence of observations processed together; synonymous with “exposure” in DP1.   |
| exposure        | YYYYMMDD#####                      | A single exposure of all nine ComCam detectors.   |
| instrument      | LSSTComCam                         | The instrument name.  |
| detector        | 0–8                                | A ComCam detector.  |
| skymap          | lsst_cells_v1                      | A set of tracts and patches that subdivide the sky into rectangular regions with simple projections and intentional overlaps. |
| tract           | See <a href="#">Table 7</a>        | A large rectangular region of the sky.  |
| patch           | 0–99                               | A rectangular region within a tract.  |
| physical_filter | u_02, g_01, i_06, r_03, z_03, y_04 | A physical filter.  |
| band            | u, g, r, i, z, y                   | An conceptual astronomical passband.  |

**Table 9.** The name and number of each type of data product in the Butler and the dimensions required to identify a specific dataset.

| Data Product                 | Name in Butler           | Required Dimensions            | Number in DP1 |
|------------------------------|--------------------------|--------------------------------|---------------|
| <b>Image Data Products</b>   |                          |                                |               |
| raw                          | raw                      | instrument, detector, exposure | 16125         |
| visit_image                  | visit_image              | instrument, detector, visit    | 15972         |
| deep_coadd                   | deep_coadd               | band, skymap, tract, patch     | 2644          |
| template_coadd               | template_coadd           | band, skymap, tract, patch     | 2730          |
| difference_image             | difference_image         | instrument, detector, visit    | 15972         |
| <b>Catalog Data Products</b> |                          |                                |               |
| Source                       | source                   | instrument, visit              | 1786          |
| Object                       | object                   | skymap, tract                  | 29            |
| ForcedSource                 | object_forced_source     | skymap, tract, patch           | 636           |
| DiaSource                    | dia_source               | skymap, tract                  | 25            |
| DiaObject                    | dia_object               | skymap, tract                  | 25            |
| ForcedSourceOnDiaObject      | dia_object_forced_source | skymap, tract, patch           | 597           |
| SSSource                     | ss_source                | –                              | 1             |
| SSObject                     | ss_object                | –                              | 1             |
| Visit                        | visit_table              | instrument                     | 1             |
| CcdVisit                     | visit_detector_table     | instrument                     | 1             |

2940 ing a user security token. This token can then be used  
 2941 as a bearer token for [API](#) calls to the [RSP TAP](#) service.  
 2942 This capability is especially useful for remote data anal-  
 2943 ysis using tools such as [TOPCAT](#), as well as enabling  
 2944 third-party systems, e.g., Community Alert Brokers, to  
 2945 access Rubin data. Additionally, it supports remote de-  
 2946 velopment, allowing for more flexible workflows and in-  
 2947 tegration with external systems.

### 2948 6.3. Portal Aspect

2949 The Portal Aspect provides an interactive web-based  
 2950 environment for exploratory data discovery, filtering,  
 2951 querying ,and visualization of both image and catalog  
 2952 data, without requiring programming expertise. It en-  
 2953 ables users to access and analyze large datasets via tools  
 2954 for catalog queries, image browsing, time-series inspec-  
 2955 tion, and cross-matching.

The Portal is built on [Firefly](#) ([X. Wu et al. 2019](#)), a web application framework developed by the Infrared Processing and Analysis Center (IPAC). [Firefly](#) provides interactive capabilities such as customizable table views, image overlays, multi-panel visualizations, and synchronized displays linking catalog and image data.

Designed to support both exploratory data access and detailed scientific investigation, the Portal delivers an intuitive user experience, allowing users to visually analyze data while retaining access to underlying metadata and query controls.

#### 6.4. Notebook Aspect

The Notebook Aspect provides an interactive, web-based environment built on Jupyter Notebooks, enabling users to write and execute Python code directly on Rubin and [LSST](#) data without downloading it locally. It offers programmatic access to Rubin and [LSST](#) data products, allowing users to query and retrieve datasets, manipulate and display images, compute derived properties, plot results, and reprocess data using the [LSST Science Pipelines](#) (§4.1). The environment comes pre-installed with the pipelines and a broad set of widely used astronomical [software](#) tools, supporting immediate and flexible data analysis.

#### 6.5. Databases

The user-facing Aspects of the [RSP](#) are supported by several backend databases that store catalog data products, image metadata, and other derived datasets. The [schema](#) for [DP1](#) and other Rubin databases are available online at <https://sdm-schemas.lsst.io>.

##### 6.5.1. Qserv

The final 10-year [LSST](#) catalog is expected to reach 15 PB and contain measurements for billions of stars and galaxies across trillions of detections. To support efficient storage, querying, and analysis of this dataset, Rubin Observatory developed [Qserv](#) ([D. L. Wang et al. 2011](#); ?) – a scalable, parallel, distributed SQL database system. [Qserv](#) partitions data over approximately equal-area regions of the celestial sphere, replicates data to ensure resilience and high availability, and uses shared scanning to reduce overall I/O load. It also supports a package of scientific user-defined functions (SciSQL: <https://smonkewitz.github.io/scisql/>) simplifying complex queries involving spherical geometry, statistics, and photometry. [Qserv](#) is built on robust production-quality components, including [MariaDB](#) (<https://www.mariadb.org/>) and [XRootD](#) (<https://xrootd.org/>). [Qserv](#) runs at the [USDF](#) and user access to catalog data is via the [TAP](#) service (§6.2.1).

This enables catalog-based analysis through both the [RSP](#) Portal and [Notebook](#) Aspects.

Although the small [DP1](#) dataset does not require [Qserv](#)’s full capabilities, we nevertheless chose to use it for [DP1](#) to accurately reflect the future data access environment and to gain experience with scientifically-motivated queries ahead of full-scale deployment. [Qserv](#) is open-source and available on [GitHub](#): <https://github.com/lsst/qserv>.

## 7. SUPPORT FOR COMMUNITY SCIENCE

Rubin Observatory has a science community that encompasses thousands of individuals worldwide, with a broad range of experience and expertise in astronomy in general, and in the analysis of optical imaging data specifically.

Rubin’s model to support this diverse community to access and analyze [DP1](#) emphasizes self-help via documentation and tutorials, and employs an open platform for asynchronous issue reporting that enables crowd-sourced solutions. These two aspects of community support are augmented by virtual engagement activities. In addition, Rubin supports its Users Committee to advocate on behalf of the science community, and supports the eight [LSST](#) Science Collaborations (§7.6).

All of the resources for scientists that are discussed in this section are discoverable by browsing the *For Scientists* pages of the Rubin Observatory website<sup>109</sup>.

### 7.1. Documentation

The data release documentation for [DP1](#)<sup>110</sup> provides an overview of the [LSSTComCam](#) observations, detailed descriptions of the data products, and a high-level summary of the processing pipelines. Although much of its content overlaps significantly with this paper, the documentation is presented as a searchable, web-based resource built using [Sphinx](#)<sup>111</sup>, with a focus on enabling scientific use of the data products.

### 7.2. Tutorials

A suite of tutorials ([NSF-DOE Vera C. Rubin Observatory 2021](#)) that demonstrate how to access and analyze [DP1](#) using the [RSP](#) accompanies the [DP1](#) release<sup>112</sup>. Jupyter Notebook tutorials are available via the “Tutorials” drop-down menu within the [Notebook](#) aspect of the [RSP](#). Tutorials for the [Portal](#) and [API](#) aspects of the [RSP](#) can be found in the data release documentation.

<sup>109</sup> <https://rubinobservatory.org/for-scientists>

<sup>110</sup> <https://dp1.lsst.io>

<sup>111</sup> <https://www.sphinx-doc.org/>

<sup>112</sup> <https://dp1.lsst.io/tutorials>

These tutorials are designed to be inclusive, accessible, clear, focused, and consistent. Their format and contents follow a set of guidelines (M. L. Graham et al. 2026) that are informed by modern standards in technical writing.

### 7.3. Community Forum

The venue for all user support is the Rubin Community Forum<sup>113</sup>. Questions about any and all aspects of the Rubin data products, pipelines, and services, including DP1, should be posted as new topics in the Support category. This includes beginner-level and “how-to” questions, advanced scientific analysis questions, technical bug reports, account and data access issues, and everything in between. The Support category of the Forum is monitored by Rubin staff, who follow an established internal workflow for following-up and resolving all reported issues.

The Rubin Community Forum is built on the open-source Discourse platform. It was chosen because, for a worldwide community of ten thousand Rubin users, a traditional (i.e., closed) help desk represents a risk to Rubin science (e.g., many users with the same question having to wait for responses). The open nature of the Forum enables self-help by letting users search for similar issues, and enables crowd-sourced problem solving (and avoids knowledge bottlenecks) by letting users help users.

The Rubin Community Forum, and the internal staff workflows for user support, were set up, tested, and refined with DP0 so that it was ready for use with DP1.

### 7.4. Engagement Activities

A variety of live virtual and in-person workshops and seminars offer learning opportunities to scientists and students working with the Rubin data products, services, and tools.

- Rubin Science Assemblies (weekly, virtual, 1 hour): alternates between hands-on tutorials based on the most recent data release and open drop-in “office hours” with Rubin staff.
- Rubin Data Academy (annual, virtual, 3-4 days): an intense set of hands-on tutorials based on the most recent data release, along with co-working and networking sessions.
- Rubin Community Workshop (annual, virtual, 5 days), a science-focused conference of contributed

posters, talks, and sessions led by members of the Rubin science community and Rubin staff.

Following the release of DP1, all of these engagement activities focused on use of DP1 by the science community. In particular, the 2025 Rubin Data Academy was run the week of the DP1 release, in order to immediately facilitate community access. The 2025 Rubin Community Workshop had several sessions to introduce people to the DP1 dataset and demonstrate how to access and analyze it with the RSP.

For schedules, connection information, zoom recordings, and associated materials, visit the *For Scientists* pages of the Rubin Observatory website<sup>114</sup>. Requests for custom tutorials and presentations for research groups are also accommodated.

### 7.5. Users Committee

This committee is charged with soliciting feedback from the science community, advocating on their behalf, and recommending science-driven improvements to the LSST data products and the Rubin Science Platform tools and services. Community members are encouraged to attend their virtual meetings and raise issues to their attention, so they can be included in the committee’s twice-yearly reports to the Rubin Observatory Director.

Like the Forum, the Users Committee was established and began its work with DP0, and that feedback was implemented for DP1. The community’s response to DP1 will be especially valuable input to DP2 and DR1, and the Users Committee encourages all users to interact with them. For a list of members and contact information, visit the *For Scientists* pages of the Rubin Observatory website.

### 7.6. Science Collaborations

The eight LSST Science Collaborations are independent, worldwide communities of scientists, self-organized into collaborations based on their research interests and expertise. Members work together to apply for funding, build software infrastructure and analysis algorithms, and incorporate external data sets into their LSST-based research.

The Science Collaborations also provide valuable advice to Rubin Observatory on the operational strategies and data products to accomplish specific science goals, and Rubin Observatory supports the collaborations via staff liaisons and regular virtual meetings with Rubin operations leadership.

<sup>113</sup> <https://community.lsst.org/>

<sup>114</sup> <https://rubinobservatory.org/for-scientists/events-deadlines>

3142 The Science Collaborations have been functioning for  
 3143 many years, and their engagement and feedback on DP0  
 3144 was implemented into the community science model for  
 3145 DP1, as it will for future data releases.

## 3146 8. SUMMARY AND FUTURE RELEASES

3147 Rubin Data Preview 1 offers an initial look at the first  
 3148 on-sky data products and access services from the Vera  
 3149 C. Rubin Observatory. DP1 forms part of Rubin’s Early  
 3150 Science Program, and provides the scientific community  
 3151 with an early opportunity to familiarize themselves with  
 3152 the data formats and access infrastructure for the forth-  
 3153 coming Legacy Survey of Space and Time. This early  
 3154 release has a proprietary period of two years, during  
 3155 which time it is available to Rubin data rights holders  
 3156 only via the cloud-based RSP.

3157 In this paper we have described the completion status  
 3158 of the observatory at the time of data acquisition, the  
 3159 commissioning campaign that forms the basis of DP1,  
 3160 and the processing pipelines used to produce early ver-  
 3161 sions of data products. We provide details on the data  
 3162 products, their characteristics and known issues, and  
 3163 describe the Rubin Science Platform for access to and  
 3164 analysis of DP1.

3165 The data products described in this paper derive from  
 3166 observations obtained by LSSTComCam. LSSTCom-  
 3167 Cam contains only around 5% the number of CCDs as  
 3168 the full LSST Science Camera (LSSTCam), yet the DP1  
 3169 dataset that it has produced will already enable a very  
 3170 broad range of science. At 3.5 TB in size, DP1 covers  
 3171 a total area of  $\sim 15$  deg<sup>2</sup> and contains 1792 single-epoch  
 3172 images, 2644 deep coadded images and 2.3 million dis-  
 3173 tinct astrophysical objects, including 93 new asteroid  
 3174 discoveries.

3175 While some data products anticipated from the LSST  
 3176 are not yet available, e.g., cell-based coadds, DP1 in-  
 3177 cludes several products that will not be provided in fu-  
 3178 ture releases. Notably, difference images are included in  
 3179 DP1 as pre-generated products; in future releases, these  
 3180 will instead be generated on demand via dedicated ser-  
 3181 vices. The inclusion of pre-generated difference images  
 3182 in DP1 is feasible due to the relatively small size of the  
 3183 dataset, an approach that will not scale to the signifi-  
 3184 cantly larger data volumes expected in subsequent re-  
 3185 leases.

3186 The RSP is continually under development, and new  
 3187 functionality will continue to be deployed incrementally

3188 as it becomes available, and independent of the future  
 3189 data release schedule. User query history capabilities,  
 3190 context-aware documentation and a bulk cutout services  
 3191 are just a few of the services currently under develop-  
 3192 ment.

3193 Coincident with the release of DP1, Rubin Obser-  
 3194 vatory begins its Science Validation Surveys with the  
 3195 LSST Science Camera (i.e., LSSTCam). This final com-  
 3196 missioning phase will produce a dataset that will form  
 3197 the foundation for the second Rubin Data Preview, DP2.  
 3198 Full operations, marking the start of the LSST, are ex-  
 3199 pected to commence in 2026.

## 3200 ACKNOWLEDGMENTS

3201 . This material is based upon work supported in part by  
 3202 the National Science Foundation through Cooperative  
 3203 Agreements AST-1258333 and AST-2241526 and Co-  
 3204 operative Support Agreements AST-1202910 and AST-  
 3205 2211468 managed by the Association of Universities for  
 3206 Research in Astronomy (AURA), and the Department of  
 3207 Energy under Contract No. DE-AC02-76SF00515 with  
 3208 the SLAC National Accelerator Laboratory managed  
 3209 by Stanford University. Additional Rubin Observatory  
 3210 funding comes from private donations, grants to univer-  
 3211 sities, and in-kind support from LSST-DA Institutional  
 3212 Members.

3213 This work has been supported by the French Na-  
 3214 tional Institute of Nuclear and Particle Physics (IN2P3)  
 3215 through dedicated funding provided by the National  
 3216 Center for Scientific Research (CNRS).

3217 This work has been supported by STFC fund-  
 3218 ing for UK participation in LSST, through grant  
 3219 ST/Y00292X/1.

3220 *Facilities:* Rubin:Simonyi (LSSTComCam), Ru-  
 3221 bin:USDAC

3222 *Software:* Rubin Data Butler (T. Jenness et al.  
 3223 2022), LSST Science Pipelines (Rubin Observatory Sci-  
 3224 ence Pipelines Developers 2025), LSST Feature Based  
 3225 Scheduler v3.0 (P. Yoachim et al. 2024; E. Naghib et al.  
 3226 2019) Astropy (Astropy Collaboration et al. 2013, 2018,  
 3227 2022) PIFF (?), GBDES (G. M. Bernstein 2022), Qserv  
 3228 (D. L. Wang et al. 2011; F. Mueller et al. 2025), Slurm,  
 3229 HTCondor, CVMFS, FTS3, ESNet

## 3230 APPENDIX

## REFERENCES

- 3231 Abazajian, K., Adelman-McCarthy, J. K., Agüeros, M. A.,  
3232 et al. 2004, *AJ*, 128, 502, doi: [10.1086/421365](https://doi.org/10.1086/421365)
- 3233 Ahumada, R., Allende Prieto, C., Almeida, A., et al. 2020,  
3234 *ApJS*, 249, 3, doi: [10.3847/1538-4365/ab929e](https://doi.org/10.3847/1538-4365/ab929e)
- 3235 Aihara, H., AlSayyad, Y., Ando, M., et al. 2022, *PASJ*, 74,  
3236 247, doi: [10.1093/pasj/psab122](https://doi.org/10.1093/pasj/psab122)
- 3237 Allbery, R. 2023, IVOA SODA implementation experience,  
3238 SQuaRE Technical Note SQR-063, NSF-DOE Vera C.  
3239 Rubin Observatory. <https://sqr-063.lsst.io/>
- 3240 Allbery, R. 2024, Draft IVOA SODA web service  
3241 specification, SQuaRE Technical Note SQR-093,  
3242 NSF-DOE Vera C. Rubin Observatory.  
3243 <https://sqr-093.lsst.io/>
- 3244 AlSayyad, Y. 2018, Coaddition Artifact Rejection and  
3245 CompareWarp, Data Management Technical Note  
3246 DMTN-080, NSF-DOE Vera C. Rubin Observatory,  
3247 doi: [10.71929/rubin/2583441](https://doi.org/10.71929/rubin/2583441)
- 3248 Ansel, J., Yang, E., He, H., et al. 2024, in 29th ACM  
3249 International Conference on Architectural Support for  
3250 Programming Languages and Operating Systems, Volume  
3251 2 (ASPLOS '24) (ACM), doi: [10.1145/3620665.3640366](https://doi.org/10.1145/3620665.3640366)
- 3252 Antilogus, P., Astier, P., Doherty, P., Guyonnet, A., &  
3253 Regnault, N. 2014, *Journal of Instrumentation*, 9,  
3254 C03048, doi: [10.1088/1748-0221/9/03/C03048](https://doi.org/10.1088/1748-0221/9/03/C03048)
- 3255 Astropy Collaboration, Robitaille, T. P., Tollerud, E. J.,  
3256 et al. 2013, *A&A*, 558, A33,  
3257 doi: [10.1051/0004-6361/201322068](https://doi.org/10.1051/0004-6361/201322068)
- 3258 Astropy Collaboration, Price-Whelan, A. M., Sipőcz, B. M.,  
3259 et al. 2018, *AJ*, 156, 123, doi: [10.3847/1538-3881/aabc4f](https://doi.org/10.3847/1538-3881/aabc4f)
- 3260 Astropy Collaboration, Price-Whelan, A. M., Lim, P. L.,  
3261 et al. 2022, *ApJ*, 935, 167, doi: [10.3847/1538-4357/ac7c74](https://doi.org/10.3847/1538-4357/ac7c74)
- 3262 Baumann, M., Boch, T., Pineau, F.-X., et al. 2022, in  
3263 *Astronomical Society of the Pacific Conference Series*,  
3264 Vol. 532, *Astronomical Data Analysis Software and*  
3265 *Systems XXX*, ed. J. E. Ruiz, F. Pierfederici, &  
3266 P. Teuben, 7
- 3267 Bechtol, K., Sevilla-Noarbe, I., Drlica-Wagner, A., et al.  
3268 2025, arXiv e-prints, arXiv:2501.05739,  
3269 doi: [10.48550/arXiv.2501.05739](https://doi.org/10.48550/arXiv.2501.05739)
- 3270 Berk, A., Anderson, G. P., Bernstein, L. S., et al. 1999, in  
3271 *Society of Photo-Optical Instrumentation Engineers*  
3272 *(SPIE) Conference Series*, Vol. 3756, *Optical*  
3273 *Spectroscopic Techniques and Instrumentation for*  
3274 *Atmospheric and Space Research III*, ed. A. M. Larar,  
3275 348–353, doi: [10.1117/12.366388](https://doi.org/10.1117/12.366388)
- 3276 Bernstein, G. M. 2022, gbdes: DECam instrumental  
3277 signature fitting and processing programs,, *Astrophysics*  
3278 *Source Code Library*, record ascl:2210.011  
3279 <http://ascl.net/2210.011>
- 3280 Bernstein, G. M., & Jarvis, M. 2002, *AJ*, 123, 583,  
3281 doi: [10.1086/338085](https://doi.org/10.1086/338085)
- 3282 Bernstein, G. M., Armstrong, R., Plazas, A. A., et al. 2017,  
3283 *PASP*, 129, 074503, doi: [10.1088/1538-3873/aa6c55](https://doi.org/10.1088/1538-3873/aa6c55)
- 3284 Bertin, E. 2011, in *Astronomical Society of the Pacific*  
3285 *Conference Series*, Vol. 442, *Astronomical Data Analysis*  
3286 *Software and Systems XX*, ed. I. N. Evans,  
3287 A. Accomazzi, D. J. Mink, & A. H. Rots, 435
- 3288 Bianco, F. B., Ivezić, Ž., Jones, R. L., et al. 2022, *ApJS*,  
3289 258, 1, doi: [10.3847/1538-4365/ac3e72](https://doi.org/10.3847/1538-4365/ac3e72)
- 3290 Blum, R., & the Rubin Operations Team. 2020, Vera C.  
3291 Rubin Observatory Data Policy, Data Management  
3292 Operations Controlled Document RDO-013, NSF-DOE  
3293 Vera C. Rubin Observatory. <https://ls.st/RDO-013>
- 3294 Boch, T., & Fernique, P. 2014, in *Astronomical Society of*  
3295 *the Pacific Conference Series*, Vol. 485, *Astronomical*  
3296 *Data Analysis Software and Systems XXIII*, ed.  
3297 N. Manset & P. Forshay, 277
- 3298 Bonnarel, F., Dowler, P., Demleitner, M., Tody, D., &  
3299 Dempsey, J. 2017, IVOA Server-side Operations for Data  
3300 Access Version 1.0., IVOA Recommendation 17 May 2017  
3301 doi: [10.5479/ADS/bib/2017ivoa.spec.0517B](https://doi.org/10.5479/ADS/bib/2017ivoa.spec.0517B)
- 3302 Bonnarel, F., Fernique, P., Bienaymé, O., et al. 2000,  
3303 *A&AS*, 143, 33, doi: [10.1051/aas:2000331](https://doi.org/10.1051/aas:2000331)
- 3304 Bosch, J., Armstrong, R., Bickerton, S., et al. 2018, *PASJ*,  
3305 70, S5, doi: [10.1093/pasj/psx080](https://doi.org/10.1093/pasj/psx080)
- 3306 Broughton, A., Utsumi, Y., Plazas Malagón, A. A., et al.  
3307 2024, *PASP*, 136, 045003, doi: [10.1088/1538-3873/ad3aa2](https://doi.org/10.1088/1538-3873/ad3aa2)
- 3308 Burke, D. L., Rykoff, E. S., Allam, S., et al. 2018, *AJ*, 155,  
3309 41, doi: [10.3847/1538-3881/aa9f22](https://doi.org/10.3847/1538-3881/aa9f22)
- 3310 Chambers, K. C., Magnier, E. A., Metcalfe, N., et al. 2016,  
3311 arXiv e-prints, arXiv:1612.05560,  
3312 doi: [10.48550/arXiv.1612.05560](https://doi.org/10.48550/arXiv.1612.05560)
- 3313 Choi, Y., Olsen, K. A. G., Carlin, J. L., et al. 2025, arXiv  
3314 e-prints, arXiv:2507.01343,  
3315 doi: [10.48550/arXiv.2507.01343](https://doi.org/10.48550/arXiv.2507.01343)
- 3316 de Vaucouleurs, G. 1948, *Annales d’Astrophysique*, 11, 247
- 3317 de Vaucouleurs, G. 1953, *MNRAS*, 113, 134,  
3318 doi: [10.1093/mnras/113.2.134](https://doi.org/10.1093/mnras/113.2.134)
- 3319 Dowler, P., Bonnarel, F., & Tody, D. 2015, IVOA Simple  
3320 Image Access Version 2.0., IVOA Recommendation 23  
3321 December 2015  
3322 doi: [10.5479/ADS/bib/2015ivoa.spec.1223D](https://doi.org/10.5479/ADS/bib/2015ivoa.spec.1223D)
- 3323 Dowler, P., Rixon, G., Tody, D., & Demleitner, M. 2019,  
3324 Table Access Protocol Version 1.1., IVOA  
3325 Recommendation 27 September 2019  
3326 doi: [10.5479/ADS/bib/2019ivoa.spec.0927D](https://doi.org/10.5479/ADS/bib/2019ivoa.spec.0927D)

- 3327 Eggl, S., Juric, M., Moeyens, J., & Jones, L. 2020, in  
 3328 AAS/Division for Planetary Sciences Meeting Abstracts,  
 3329 Vol. 52, AAS/Division for Planetary Sciences Meeting  
 3330 Abstracts, 211.01
- 3331 Esteves, J. H., Utsumi, Y., Snyder, A., et al. 2023, PASP,  
 3332 135, 115003, doi: [10.1088/1538-3873/ad0a73](https://doi.org/10.1088/1538-3873/ad0a73)
- 3333 Euclid Collaboration, Romelli, E., Kümmel, M., et al. 2025,  
 3334 arXiv e-prints, arXiv:2503.15305,  
 3335 doi: [10.48550/arXiv.2503.15305](https://doi.org/10.48550/arXiv.2503.15305)
- 3336 Fagreluis, P., & Rykoff, E. S. 2025, Rubin Observatory  
 3337 Baseline Calibration Plan, Commissioning Technical  
 3338 Note SITCOMTN-086, NSF-DOE Vera C. Rubin  
 3339 Observatory, doi: [10.71929/rubin/2583850](https://doi.org/10.71929/rubin/2583850)
- 3340 Ferguson, P. S., Rykoff, E. S., Carlin, J. L., Saunders, C., &  
 3341 Parejko, J. K. 2025, The Monster: A reference catalog  
 3342 with synthetic ugrizy-band fluxes for the Vera C. Rubin  
 3343 observatory, Data Management Technical Note  
 3344 DMTN-277, NSF-DOE Vera C. Rubin Observatory,  
 3345 doi: [10.71929/rubin/2583688](https://doi.org/10.71929/rubin/2583688)
- 3346 Fernique, P., Allen, M. G., Boch, T., et al. 2015, A&A, 578,  
 3347 A114, doi: [10.1051/0004-6361/201526075](https://doi.org/10.1051/0004-6361/201526075)
- 3348 Fernique, P., Allen, M., Boch, T., et al. 2017, HiPS -  
 3349 Hierarchical Progressive Survey Version 1.0., IVOA  
 3350 Recommendation 19 May 2017  
 3351 doi: [10.5479/ADS/bib/2017ivoa.spec.0519F](https://doi.org/10.5479/ADS/bib/2017ivoa.spec.0519F)
- 3352 Finkbeiner, D. P., Davis, M., & Schlegel, D. J. 1999, ApJ,  
 3353 524, 867, doi: [10.1086/307852](https://doi.org/10.1086/307852)
- 3354 Fortino, W. F., Bernstein, G. M., Bernardinelli, P. H., et al.  
 3355 2021, AJ, 162, 106, doi: [10.3847/1538-3881/ac0722](https://doi.org/10.3847/1538-3881/ac0722)
- 3356 Gaia Collaboration, Montegriffo, P., Bellazzini, M., et al.  
 3357 2023a, A&A, 674, A33,  
 3358 doi: [10.1051/0004-6361/202243709](https://doi.org/10.1051/0004-6361/202243709)
- 3359 Gaia Collaboration, Vallenari, A., Brown, A. G. A., et al.  
 3360 2023b, A&A, 674, A1, doi: [10.1051/0004-6361/202243940](https://doi.org/10.1051/0004-6361/202243940)
- 3361 Górski, K. M., Hivon, E., Banday, A. J., et al. 2005, ApJ,  
 3362 622, 759, doi: [10.1086/427976](https://doi.org/10.1086/427976)
- 3363 Graham, A. W., & Driver, S. P. 2005, PASA, 22, 118,  
 3364 doi: [10.1071/AS05001](https://doi.org/10.1071/AS05001)
- 3365 Graham, M., Plante, R., Tody, D., & Fitzpatrick, M. 2014,  
 3366 PyVO: Python access to the Virtual Observatory,,  
 3367 Astrophysics Source Code Library, record ascl:1402.004
- 3368 Graham, M. L., Carlin, J. L., Adair, C. L., et al. 2026,  
 3369 Guidelines for User Tutorials, Technical Note RTN-045,  
 3370 NSF-DOE Vera C. Rubin Observatory,  
 3371 doi: [10.71929/rubin/2584020](https://doi.org/10.71929/rubin/2584020)
- 3372 Gray, B. 2025, find\_orb: Orbit determination from  
 3373 observations, [https://github.com/Bill-Gray/find\\_orb](https://github.com/Bill-Gray/find_orb)
- 3374 Guy, L. P., Bechtol, K., Bellm, E., et al. 2026, Rubin  
 3375 Observatory Plans for an Early Science Program,  
 3376 Technical Note RTN-011, NSF-DOE Vera C. Rubin  
 3377 Observatory, doi: [10.71929/rubin/2584021](https://doi.org/10.71929/rubin/2584021)
- 3378 Heinze, A., Eggl, S., Juric, M., et al. 2022, in AAS/Division  
 3379 for Planetary Sciences Meeting Abstracts, Vol. 54,  
 3380 AAS/Division for Planetary Sciences Meeting Abstracts,  
 3381 504.04
- 3382 Heinze, A., Juric, M., & Kurlander, J. 2023, heliolineX: Open  
 3383 Source Solar System Discovery Software,  
 3384 <https://github.com/heliolineX/heliolineX>
- 3385 Hirata, C., & Seljak, U. 2003, MNRAS, 343, 459,  
 3386 doi: [10.1046/j.1365-8711.2003.06683.x](https://doi.org/10.1046/j.1365-8711.2003.06683.x)
- 3387 Holman, M. J., Payne, M. J., Blankley, P., Janssen, R., &  
 3388 Kuindersma, S. 2018, AJ, 156, 135,  
 3389 doi: [10.3847/1538-3881/aad69a](https://doi.org/10.3847/1538-3881/aad69a)
- 3390 Howard, J., Reil, K., Claver, C., et al. 2018, in Society of  
 3391 Photo-Optical Instrumentation Engineers (SPIE)  
 3392 Conference Series, Vol. 10700, Ground-based and  
 3393 Airborne Telescopes VII, ed. H. K. Marshall &  
 3394 J. Spyromilio, 107003D, doi: [10.1117/12.2312684](https://doi.org/10.1117/12.2312684)
- 3395 Illingworth, G., Magee, D., Bouwens, R., et al. 2016, arXiv  
 3396 e-prints, arXiv:1606.00841,  
 3397 doi: [10.48550/arXiv.1606.00841](https://doi.org/10.48550/arXiv.1606.00841)
- 3398 Ingraham, P., Fagreluis, P., Stubbs, C. W., et al. 2022, in  
 3399 Society of Photo-Optical Instrumentation Engineers  
 3400 (SPIE) Conference Series, Vol. 12182, Ground-based and  
 3401 Airborne Telescopes IX, ed. H. K. Marshall,  
 3402 J. Spyromilio, & T. Usuda, 121820R,  
 3403 doi: [10.1117/12.2630185](https://doi.org/10.1117/12.2630185)
- 3404 Ivezić, Ž., Kahn, S. M., Tyson, J. A., et al. 2019a, ApJ,  
 3405 873, 111, doi: [10.3847/1538-4357/ab042c](https://doi.org/10.3847/1538-4357/ab042c)
- 3406 Ivezić, Ž., Kahn, S. M., Tyson, J. A., et al. 2019b, ApJ,  
 3407 873, 111, doi: [10.3847/1538-4357/ab042c](https://doi.org/10.3847/1538-4357/ab042c)
- 3408 Jarvis, M., Bernstein, G. M., Amon, A., et al. 2021,  
 3409 MNRAS, 501, 1282, doi: [10.1093/mnras/staa3679](https://doi.org/10.1093/mnras/staa3679)
- 3410 Jenness, T., & Dubois-Felsmann, G. P. 2025, IVOA  
 3411 Identifier Usage at the Rubin Observatory, Data  
 3412 Management Technical Note DMTN-302, NSF-DOE Vera  
 3413 C. Rubin Observatory, doi: [10.71929/rubin/2583848](https://doi.org/10.71929/rubin/2583848)
- 3414 Jenness, T., Voutsinas, S., Dubois-Felsmann, G. P., &  
 3415 Salnikov, A. 2024, arXiv e-prints, arXiv:2501.00544,  
 3416 doi: [10.48550/arXiv.2501.00544](https://doi.org/10.48550/arXiv.2501.00544)
- 3417 Jenness, T., Bosch, J. F., Salnikov, A., et al. 2022, in  
 3418 Society of Photo-Optical Instrumentation Engineers  
 3419 (SPIE) Conference Series, Vol. 12189, Software and  
 3420 Cyberinfrastructure for Astronomy VII, 1218911,  
 3421 doi: [10.1117/12.2629569](https://doi.org/10.1117/12.2629569)

- 3422 Jones, R. L., Yoachim, P., Ivezić, Ž., Neilsen Jr., E. H., &  
3423 Ribeiro, T. 2021, Survey Strategy and Cadence Choices  
3424 for the Vera C. Rubin Observatory Legacy Survey of  
3425 Space and Time (LSST), Project Science Technical Note  
3426 PSTN-051, NSF-DOE Vera C. Rubin Observatory,  
3427 doi: [10.71929/rubin/2584084](https://doi.org/10.71929/rubin/2584084)
- 3428 Juric, M. 2025, mpsky: Multi-purpose sky catalog  
3429 cross-matching, <https://github.com/mjuric/mpsky>
- 3430 Jurić, M., Ciardi, D., Dubois-Felsmann, G., & Guy, L.  
3431 2019, LSST Science Platform Vision Document, Systems  
3432 Engineering Controlled Document LSE-319, NSF-DOE  
3433 Vera C. Rubin Observatory, doi: [10.71929/rubin/2587242](https://doi.org/10.71929/rubin/2587242)
- 3434 Jurić, M., Axelrod, T. S., Becker, A. C., et al. 2023, Data  
3435 Products Definition Document, Systems Engineering  
3436 Controlled Document LSE-163, NSF-DOE Vera C. Rubin  
3437 Observatory, doi: [10.71929/rubin/2587118](https://doi.org/10.71929/rubin/2587118)
- 3438 Kannawadi, A. 2025, Consistent galaxy colors with  
3439 Gaussian-Aperture and PSF photometry, Data  
3440 Management Technical Note DMTN-190, NSF-DOE Vera  
3441 C. Rubin Observatory, doi: [10.71929/rubin/2583849](https://doi.org/10.71929/rubin/2583849)
- 3442 Kron, R. G. 1980, ApJS, 43, 305, doi: [10.1086/190669](https://doi.org/10.1086/190669)
- 3443 Kuijken, K. 2008, A&A, 482, 1053,  
3444 doi: [10.1051/0004-6361:20066601](https://doi.org/10.1051/0004-6361:20066601)
- 3445 Lange, T., Nordby, M., Pollek, H., et al. 2024, in Society of  
3446 Photo-Optical Instrumentation Engineers (SPIE)  
3447 Conference Series, Vol. 13096, Ground-based and  
3448 Airborne Instrumentation for Astronomy X, ed. J. J.  
3449 Bryant, K. Motohara, & J. R. D. Vernet, 130961O,  
3450 doi: [10.1117/12.3019302](https://doi.org/10.1117/12.3019302)
- 3451 Léget, P. F., Astier, P., Regnault, N., et al. 2021, A&A,  
3452 650, A81, doi: [10.1051/0004-6361/202140463](https://doi.org/10.1051/0004-6361/202140463)
- 3453 Lim, K.-T. 2023, Proposal and Prototype for Prompt  
3454 Processing, Data Management Technical Note  
3455 DMTN-219, NSF-DOE Vera C. Rubin Observatory,  
3456 doi: [10.71929/rubin/2585429](https://doi.org/10.71929/rubin/2585429)
- 3457 Louys, M., Tody, D., Dowler, P., et al. 2017, Observation  
3458 Data Model Core Components, its Implementation in the  
3459 Table Access Protocol Version 1.1., IVOA  
3460 Recommendation 09 May 2017  
3461 doi: [10.5479/ADS/bib/2017ivoa.spec.0509L](https://doi.org/10.5479/ADS/bib/2017ivoa.spec.0509L)
- 3462 LSST Dark Energy Science Collaboration (LSST DESC),  
3463 Abolfathi, B., Alonso, D., et al. 2021, ApJS, 253, 31,  
3464 doi: [10.3847/1538-4365/abd62c](https://doi.org/10.3847/1538-4365/abd62c)
- 3465 Lupton, R., Blanton, M. R., Fekete, G., et al. 2004, PASP,  
3466 116, 133, doi: [10.1086/382245](https://doi.org/10.1086/382245)
- 3467 Lust, N. B., Jenness, T., Bosch, J. F., et al. 2023, arXiv  
3468 e-prints, arXiv:2303.03313,  
3469 doi: [10.48550/arXiv.2303.03313](https://doi.org/10.48550/arXiv.2303.03313)
- 3470 Mandelbaum, R., Hirata, C. M., Seljak, U., et al. 2005,  
3471 MNRAS, 361, 1287,  
3472 doi: [10.1111/j.1365-2966.2005.09282.x](https://doi.org/10.1111/j.1365-2966.2005.09282.x)
- 3473 Megias Homar, G., Kahn, S. M., Meyers, J. M., Crenshaw,  
3474 J. F., & Thomas, S. J. 2024a, ApJ, 974, 108,  
3475 doi: [10.3847/1538-4357/ad6cdc](https://doi.org/10.3847/1538-4357/ad6cdc)
- 3476 Megias Homar, G., Tighe, R., Thomas, S., et al. 2024b, in  
3477 Society of Photo-Optical Instrumentation Engineers  
3478 (SPIE) Conference Series, Vol. 13094, Ground-based and  
3479 Airborne Telescopes X, ed. H. K. Marshall, J. Spyromilio,  
3480 & T. Usuda, 130943C, doi: [10.1117/12.3019031](https://doi.org/10.1117/12.3019031)
- 3481 Melchior, P., Moolekamp, F., Jerdee, M., et al. 2018,  
3482 Astronomy and Computing, 24, 129,  
3483 doi: [10.1016/j.ascom.2018.07.001](https://doi.org/10.1016/j.ascom.2018.07.001)
- 3484 Mueller, F., Gaponenko, I., Gates, J., et al. 2025, in  
3485 Astronomical Society of the Pacific Conference Series,  
3486 Vol. 538, Astronomical Data Analysis Software and  
3487 Systems XXXII, ed. S. Gaudet, D. Bohlender, S. Gwyn,  
3488 A. Hincks, & P. Teuben, 114, doi: [10.26624/XCPI7375](https://doi.org/10.26624/XCPI7375)
- 3489 Naghib, E., Yoachim, P., Vanderbei, R. J., Connolly, A. J.,  
3490 & Jones, R. L. 2019, AJ, 157, 151,  
3491 doi: [10.3847/1538-3881/aafece](https://doi.org/10.3847/1538-3881/aafece)
- 3492 NSF-DOE Vera C. Rubin Observatory. 2021, Rubin  
3493 Observatory LSST Tutorials [Computer Software],  
3494 NSF-DOE Vera C. Rubin Observatory,  
3495 doi: [10.11578/rubin/dc.20250909.20](https://doi.org/10.11578/rubin/dc.20250909.20)
- 3496 NSF-DOE Vera C. Rubin Observatory. 2025a, Legacy  
3497 Survey of Space and Time Data Preview 1 [Data set],  
3498 NSF-DOE Vera C. Rubin Observatory,  
3499 doi: [10.71929/RUBIN/2570308](https://doi.org/10.71929/RUBIN/2570308)
- 3500 NSF-DOE Vera C. Rubin Observatory. 2025b, Legacy  
3501 Survey of Space and Time Data Preview 1: raw dataset  
3502 type [Data set], NSF-DOE Vera C. Rubin Observatory,  
3503 doi: [10.71929/RUBIN/2570310](https://doi.org/10.71929/RUBIN/2570310)
- 3504 NSF-DOE Vera C. Rubin Observatory. 2025c, Legacy  
3505 Survey of Space and Time Data Preview 1: visit\_image  
3506 dataset type [Data set], NSF-DOE Vera C. Rubin  
3507 Observatory, doi: [10.71929/RUBIN/2570311](https://doi.org/10.71929/RUBIN/2570311)
- 3508 NSF-DOE Vera C. Rubin Observatory. 2025d, Legacy  
3509 Survey of Space and Time Data Preview 1:  
3510 template\_coadd dataset type [Data set], NSF-DOE Vera  
3511 C. Rubin Observatory, doi: [10.71929/RUBIN/2570314](https://doi.org/10.71929/RUBIN/2570314)
- 3512 NSF-DOE Vera C. Rubin Observatory. 2025e, Legacy  
3513 Survey of Space and Time Data Preview 1:  
3514 difference\_image dataset type [Data set], NSF-DOE Vera  
3515 C. Rubin Observatory, doi: [10.71929/RUBIN/2570312](https://doi.org/10.71929/RUBIN/2570312)
- 3516 NSF-DOE Vera C. Rubin Observatory. 2025f, Legacy  
3517 Survey of Space and Time Data Preview 1: Source  
3518 searchable catalog [Data set], NSF-DOE Vera C. Rubin  
3519 Observatory, doi: [10.71929/RUBIN/2570323](https://doi.org/10.71929/RUBIN/2570323)

- 3520 NSF-DOE Vera C. Rubin Observatory. 2025g, Legacy  
3521 Survey of Space and Time Data Preview 1: Object  
3522 searchable catalog [Data set], NSF-DOE Vera C. Rubin  
3523 Observatory, doi: [10.71929/RUBIN/2570325](https://doi.org/10.71929/RUBIN/2570325)
- 3524 NSF-DOE Vera C. Rubin Observatory. 2025h, Legacy  
3525 Survey of Space and Time Data Preview 1: ForcedSource  
3526 searchable catalog [Data set], NSF-DOE Vera C. Rubin  
3527 Observatory, doi: [10.71929/RUBIN/2570327](https://doi.org/10.71929/RUBIN/2570327)
- 3528 NSF-DOE Vera C. Rubin Observatory. 2025i, Legacy  
3529 Survey of Space and Time Data Preview 1: DiaSource  
3530 searchable catalog [Data set], NSF-DOE Vera C. Rubin  
3531 Observatory, doi: [10.71929/RUBIN/2570317](https://doi.org/10.71929/RUBIN/2570317)
- 3532 NSF-DOE Vera C. Rubin Observatory. 2025j, Legacy  
3533 Survey of Space and Time Data Preview 1: DiaObject  
3534 searchable catalog [Data set], NSF-DOE Vera C. Rubin  
3535 Observatory, doi: [10.71929/RUBIN/2570319](https://doi.org/10.71929/RUBIN/2570319)
- 3536 NSF-DOE Vera C. Rubin Observatory. 2025k, Legacy  
3537 Survey of Space and Time Data Preview 1:  
3538 ForcedSourceOnDiaObject searchable catalog [Data set],  
3539 NSF-DOE Vera C. Rubin Observatory,  
3540 doi: [10.71929/RUBIN/2570321](https://doi.org/10.71929/RUBIN/2570321)
- 3541 NSF-DOE Vera C. Rubin Observatory. 2025l, Legacy  
3542 Survey of Space and Time Data Preview 1: SSOBJECT  
3543 searchable catalog [Data set], NSF-DOE Vera C. Rubin  
3544 Observatory, doi: [10.71929/RUBIN/2570335](https://doi.org/10.71929/RUBIN/2570335)
- 3545 NSF-DOE Vera C. Rubin Observatory. 2025m, Legacy  
3546 Survey of Space and Time Data Preview 1: SSSource  
3547 searchable catalog [Data set], NSF-DOE Vera C. Rubin  
3548 Observatory, doi: [10.71929/RUBIN/2570333](https://doi.org/10.71929/RUBIN/2570333)
- 3549 NSF-DOE Vera C. Rubin Observatory. 2025n, Legacy  
3550 Survey of Space and Time Data Preview 1: CcdVisit  
3551 searchable catalog [Data set], NSF-DOE Vera C. Rubin  
3552 Observatory, doi: [10.71929/RUBIN/2570331](https://doi.org/10.71929/RUBIN/2570331)
- 3553 NSF-DOE Vera C. Rubin Observatory. 2025o, Legacy  
3554 Survey of Space and Time Data Preview 1: survey  
3555 property dataset type [Data set], NSF-DOE Vera C.  
3556 Rubin Observatory, doi: [10.71929/RUBIN/2570315](https://doi.org/10.71929/RUBIN/2570315)
- 3557 Oke, J. B., & Gunn, J. E. 1983, ApJ, 266, 713,  
3558 doi: [10.1086/160817](https://doi.org/10.1086/160817)
- 3559 O'Mullane, W., Economou, F., Huang, F., et al. 2024a, in  
3560 Astronomical Society of the Pacific Conference Series,  
3561 Vol. 535, Astronomical Data Analysis Software and Systems  
3562 XXXI, ed. B. V. Hugo, R. Van Rooyen, & O. M.  
3563 Smirnov, 227, doi: [10.48550/arXiv.2111.15030](https://doi.org/10.48550/arXiv.2111.15030)
- 3564 O'Mullane, W., AlSayyad, Y., Chiang, J., et al. 2024b, in  
3565 Society of Photo-Optical Instrumentation Engineers  
3566 (SPIE) Conference Series, Vol. 13101, Software and  
3567 Cyberinfrastructure for Astronomy VIII, ed. J. Ibsen &  
3568 G. Chiozzi, 131012B, doi: [10.1117/12.3018005](https://doi.org/10.1117/12.3018005)
- 3569 Onken, C. A., Wolf, C., Bessell, M. S., et al. 2019, PASA,  
3570 36, e033, doi: [10.1017/pasa.2019.27](https://doi.org/10.1017/pasa.2019.27)
- 3571 Park, H. Y., Nomerotski, A., & Tsybychev, D. 2017,  
3572 Journal of Instrumentation, 12, C05015,  
3573 doi: [10.1088/1748-0221/12/05/C05015](https://doi.org/10.1088/1748-0221/12/05/C05015)
- 3574 Petrosian, V. 1976, ApJL, 210, L53,  
3575 doi: [10.1086/18230110.1086/182253](https://doi.org/10.1086/18230110.1086/182253)
- 3576 Plazas, A. A., Shapiro, C., Smith, R., Huff, E., & Rhodes, J.  
3577 2018, PASP, 130, 065004, doi: [10.1088/1538-3873/aab820](https://doi.org/10.1088/1538-3873/aab820)
- 3578 Plazas Malagón, A. A., Digel, S. W., Roodman, A., et al.  
3579 2026, LSSTCam and LSSTComCam Focal Plane  
3580 Layouts, Camera Technical Note CTN-001, NSF-DOE  
3581 Vera C. Rubin Observatory, doi: [10.71929/rubin/2584019](https://doi.org/10.71929/rubin/2584019)
- 3582 Plazas Malagón, A. A., Waters, C., Broughton, A., et al.  
3583 2025, Journal of Astronomical Telescopes, Instruments,  
3584 and Systems, 11, 011209,  
3585 doi: [10.1117/1.JATIS.11.1.011209](https://doi.org/10.1117/1.JATIS.11.1.011209)
- 3586 Porter, M. N., Tucker, D. L., Smith, J. A., & Adair, C. L.  
3587 2026, Photometric Transformation Relations for the  
3588 LSST Data Preview 1, Technical Note RTN-099,  
3589 NSF-DOE Vera C. Rubin Observatory,  
3590 doi: [10.71929/rubin/3006074](https://doi.org/10.71929/rubin/3006074)
- 3591 Refregier, A. 2003, ARA&A, 41, 645,  
3592 doi: [10.1146/annurev.astro.41.111302.102207](https://doi.org/10.1146/annurev.astro.41.111302.102207)
- 3593 Reiss, D. J., & Lupton, R. H. 2016, Implementation of  
3594 Image Difference Decorrelation, Data Management  
3595 Technical Note DMTN-021, NSF-DOE Vera C. Rubin  
3596 Observatory, doi: [10.71929/rubin/2586490](https://doi.org/10.71929/rubin/2586490)
- 3597 Roodman, A., Rasmussen, A., Bradshaw, A., et al. 2024, in  
3598 Society of Photo-Optical Instrumentation Engineers  
3599 (SPIE) Conference Series, Vol. 13096, Ground-based and  
3600 Airborne Instrumentation for Astronomy X, ed. J. J.  
3601 Bryant, K. Motohara, & J. R. D. Vernet, 130961S,  
3602 doi: [10.1117/12.3019698](https://doi.org/10.1117/12.3019698)
- 3603 Rubin, V. C., & Ford, Jr., W. K. 1970, ApJ, 159, 379,  
3604 doi: [10.1086/150317](https://doi.org/10.1086/150317)
- 3605 Rubin, V. C., Ford, Jr., W. K., & Thonnard, N. 1980, ApJ,  
3606 238, 471, doi: [10.1086/158003](https://doi.org/10.1086/158003)
- 3607 Rubin Observatory Science Pipelines Developers. 2025, The  
3608 LSST Science Pipelines Software: Optical Survey  
3609 Pipeline Reduction and Analysis Environment, Project  
3610 Science Technical Note PSTN-019, NSF-DOE Vera C.  
3611 Rubin Observatory, doi: [10.71929/rubin/2570545](https://doi.org/10.71929/rubin/2570545)
- 3612 Rubin's Survey Cadence Optimization Committee, Bauer,  
3613 F. E., Brough, S., et al. 2022, Survey Cadence  
3614 Optimization Committee's Phase 1 Recommendation,  
3615 Project Science Technical Note PSTN-053, NSF-DOE  
3616 Vera C. Rubin Observatory, doi: [10.71929/rubin/2584276](https://doi.org/10.71929/rubin/2584276)

- 3617 Rubin's Survey Cadence Optimization Committee, Bauer,  
3618 F. E., Bianco, F. B., et al. 2023, Survey Cadence  
3619 Optimization Committee's Phase 2 Recommendations,  
3620 Project Science Technical Note PSTN-055, NSF-DOE  
3621 Vera C. Rubin Observatory, doi: [10.71929/rubin/2585249](https://doi.org/10.71929/rubin/2585249)
- 3622 Rubin's Survey Cadence Optimization Committee, Bianco,  
3623 F. B., Jones, R. L., et al. 2025, Survey Cadence  
3624 Optimization Committee's Phase 3 Recommendations,  
3625 Project Science Technical Note PSTN-056, NSF-DOE  
3626 Vera C. Rubin Observatory, doi: [10.71929/rubin/2585402](https://doi.org/10.71929/rubin/2585402)
- 3627 Rykoff, E. S., Tucker, D. L., Burke, D. L., et al. 2023, arXiv  
3628 e-prints, arXiv:2305.01695,  
3629 doi: [10.48550/arXiv.2305.01695](https://doi.org/10.48550/arXiv.2305.01695)
- 3630 Saunders, C. 2024, Astrometric Calibration in the LSST  
3631 Pipeline, Data Management Technical Note DMTN-266,  
3632 NSF-DOE Vera C. Rubin Observatory,  
3633 doi: [10.71929/rubin/2583846](https://doi.org/10.71929/rubin/2583846)
- 3634 Schutt, T., Jarvis, M., Roodman, A., et al. 2025, The Open  
3635 Journal of Astrophysics, 8, 26, doi: [10.33232/001c.132299](https://doi.org/10.33232/001c.132299)
- 3636 Sérsic, J. L. 1963, Boletín de la Asociación Argentina de  
3637 Astronomía La Plata Argentina, 6, 41
- 3638 Sersic, J. L. 1968, Atlas de Galaxias Australes (Cordoba,  
3639 Argentina: Observatorio Astronomico)
- 3640 Shanks, T., Metcalfe, N., Chehade, B., et al. 2015,  
3641 MNRAS, 451, 4238, doi: [10.1093/mnras/stv1130](https://doi.org/10.1093/mnras/stv1130)
- 3642 SLAC National Accelerator Laboratory, & NSF-DOE Vera  
3643 C. Rubin Observatory. 2024, LSST Commissioning  
3644 Camera, SLAC National Accelerator Laboratory (SLAC),  
3645 Menlo Park, CA (United States),  
3646 doi: [10.71929/RUBIN/2561361](https://doi.org/10.71929/RUBIN/2561361)
- 3647 Slater, C. T., Ivezić, Ž., & Lupton, R. H. 2020, AJ, 159, 65,  
3648 doi: [10.3847/1538-3881/ab6166](https://doi.org/10.3847/1538-3881/ab6166)
- 3649 Smith, G. E. 2010, Reviews of Modern Physics, 82, 2307,  
3650 doi: [10.1103/RevModPhys.82.2307](https://doi.org/10.1103/RevModPhys.82.2307)
- 3651 Stalder, B., Reil, K., Claver, C., et al. 2020, in Society of  
3652 Photo-Optical Instrumentation Engineers (SPIE)  
3653 Conference Series, Vol. 11447, Ground-based and  
3654 Airborne Instrumentation for Astronomy VIII, ed. C. J.  
3655 Evans, J. J. Bryant, & K. Motohara, 114470L,  
3656 doi: [10.1117/12.2561132](https://doi.org/10.1117/12.2561132)
- 3657 Stalder, B., Reil, K., Aguilar, C., et al. 2022, in Society of  
3658 Photo-Optical Instrumentation Engineers (SPIE)  
3659 Conference Series, Vol. 12184, Ground-based and  
3660 Airborne Instrumentation for Astronomy IX, ed. C. J.  
3661 Evans, J. J. Bryant, & K. Motohara, 121840J,  
3662 doi: [10.1117/12.2630184](https://doi.org/10.1117/12.2630184)
- 3663 Stalder, B., Munoz, F., Aguilar, C., et al. 2024, in Society  
3664 of Photo-Optical Instrumentation Engineers (SPIE)  
3665 Conference Series, Vol. 13094, Ground-based and  
3666 Airborne Telescopes X, ed. H. K. Marshall, J. Spyromilio,  
3667 & T. Usuda, 1309409, doi: [10.1117/12.3019266](https://doi.org/10.1117/12.3019266)
- 3668 Swinbank, J. D., Axelrod, T. S., Becker, A. C., et al. 2020,  
3669 Data Management Science Pipelines Design, Data  
3670 Management Controlled Document LDM-151, NSF-DOE  
3671 Vera C. Rubin Observatory, doi: [10.71929/rubin/2587108](https://doi.org/10.71929/rubin/2587108)
- 3672 Taranu, D. S. 2025, The MultiProFit astronomical source  
3673 modelling code, Data Management Technical Note  
3674 DMTN-312, NSF-DOE Vera C. Rubin Observatory,  
3675 doi: [10.71929/rubin/2584108](https://doi.org/10.71929/rubin/2584108)
- 3676 Taylor, M. 2011, TOPCAT: Tool for OPERations on  
3677 Catalogues And Tables,, Astrophysics Source Code  
3678 Library, record ascl:1101.010
- 3679 Thomas, S., Connolly, A., Crenshaw, J. F., et al. 2023, in  
3680 Adaptive Optics for Extremely Large Telescopes  
3681 (AO4ELT7), 67, doi: [10.13009/AO4ELT7-2023-069](https://doi.org/10.13009/AO4ELT7-2023-069)
- 3682 Tonry, J. L., Denneau, L., Heinze, A. N., et al. 2018, PASP,  
3683 130, 064505, doi: [10.1088/1538-3873/aabadf](https://doi.org/10.1088/1538-3873/aabadf)
- 3684 Wainer, T. M., Davenport, J. R. A., Bellm, E. C., et al.  
3685 2025, Research Notes of the American Astronomical  
3686 Society, 9, 171, doi: [10.3847/2515-5172/adecef](https://doi.org/10.3847/2515-5172/adecef)
- 3687 Wang, D. L., Monkewitz, S. M., Lim, K.-T., & Becla, J.  
3688 2011, in State of the Practice Reports, SC '11 (New  
3689 York, NY, USA: ACM), 12:1–12:11,  
3690 doi: [10.1145/2063348.2063364](https://doi.org/10.1145/2063348.2063364)
- 3691 Waters, C. Z., Magnier, E. A., Price, P. A., et al. 2020,  
3692 ApJS, 251, 4, doi: [10.3847/1538-4365/abb82b](https://doi.org/10.3847/1538-4365/abb82b)
- 3693 Whitaker, K. E., Ashas, M., Illingworth, G., et al. 2019,  
3694 ApJS, 244, 16, doi: [10.3847/1538-4365/ab3853](https://doi.org/10.3847/1538-4365/ab3853)
- 3695 Wu, X., Roby, W., Goldian, T., et al. 2019, in Astronomical  
3696 Society of the Pacific Conference Series, Vol. 521,  
3697 Astronomical Data Analysis Software and Systems  
3698 XXVI, ed. M. Molinaro, K. Shortridge, & F. Pasian, 32
- 3699 Xin, B., Claver, C., Liang, M., et al. 2015, ApOpt, 54,  
3700 9045, doi: [10.1364/AO.54.009045](https://doi.org/10.1364/AO.54.009045)
- 3701 Yoachim, P. 2022, Survey Strategy: Rolling Cadence,  
3702 Project Science Technical Note PSTN-052, NSF-DOE  
3703 Vera C. Rubin Observatory, doi: [10.71929/rubin/2584109](https://doi.org/10.71929/rubin/2584109)
- 3704 Yoachim, P., Jones, L., Eric H. Neilsen, J., & Becker, M. R.  
3705 2024, lsst/rubin\_scheduler: v3.0.0, v3.0.0 Zenodo,  
3706 doi: [10.5281/zenodo.13985198](https://doi.org/10.5281/zenodo.13985198)
- 3707 Zhang, T., Almoubayyed, H., Mandelbaum, R., et al. 2023,  
3708 MNRAS, 520, 2328, doi: [10.1093/mnras/stac3350](https://doi.org/10.1093/mnras/stac3350)